STUDY OF STOCHASTICLLY VARYING THROUGH THE THICKNESS PERMEABILITY OF WOVEN FABRIC AND ITS EFFECT ON VOID FORMATION IN LIQUID COMPOSITE MOLDING PROCESSES

by

Minyoung Yun

A dissertation submitted to the Faculty of the University of Delaware in partial fulfillment of the requirements for the degree of Doctor of Philosophy in Mechanical Engineering

Fall 2018

STUDY OF STOCHASTICLLY VARYING THROUGH THE THICKNESS PERMEABILITY OF WOVEN FABRIC AND ITS EFFECT ON VOID FORMATION IN LIQUID COMPOSITE MOLDING PROCESSES

by

Minyoung Yun

Approved: _____
Ajay K. Prasad, Ph.D.
Chair of the Department of Mechanical Engineering

Approved: _____
Levi T. Thompson, Ph.D.
Dean of the College of Engineering

Approved: _____
Douglas J. Doren, Ph.D.
Interim Vice Provost for Graduate and Professional Education

I certify that I have read this dissertation and that in my opinion it meets the academic and professional standard required by the University as a dissertation for the degree of Doctor of Philosophy.

Signed: _____

Suresh G. Advani, Ph.D.
Professor in charge of dissertation

I certify that I have read this dissertation and that in my opinion it meets the academic and professional standard required by the University as a dissertation for the degree of Doctor of Philosophy.

Signed: _____

R. Valery Roy, Ph.D.
Member of dissertation committee

I certify that I have read this dissertation and that in my opinion it meets the academic and professional standard required by the University as a dissertation for the degree of Doctor of Philosophy.

Signed: _____

Christophe Binetruy, Ph.D.
Member of dissertation committee

I certify that I have read this dissertation and that in my opinion it meets the academic and professional standard required by the University as a dissertation for the degree of Doctor of Philosophy.

Signed: _____

Pavel Simacek, Ph.D.
Member of dissertation committee

ACKNOWLEDGMENTS

First of all, I give great thanks to my advisor, Professor Suresh Advani. He has trusted me all along even when I was doubting my own capability. He gave me an opportunity to work in his lab, knowing I do not have background in composites or mechanical engineering. Thanks to him, I was able to work on exciting projects and interact with amazingly fun and intelligent people in this Composite Center.

I thank the graduate students from mechanical engineering department and CCM for helping me through this long journey of PhD. I would not have been able to arrive at this finish line without their help and advice. I feel truly lucky to know these people in my life.

Of course, I also grateful to my family, especially my sister. She has always encouraged me and believed in me that I could do this. It was not always easy to be a PhD student in a foreign country. It was my sister who would give me kind and encouraging words. I truly thank her for that.

Last but not least, I thank my husband (Bamtoli) for always being there for me when I was going through difficult times or happy times during my PhD years. He has been inspiring for new ideas and motivating. Thank you so much my love.

TABLE OF CONTENTS

LIST OF TABLES

LIST OF FIGURES

ABSTRACT

Quantifying the effect of geometric, material and process variability on the manufacturing process is the subject of this thesis specifically applied to a class of composite manufacturing processed called as Liquid Composite Molding (LCM). In LCM, the material which is a stack of woven or stitched fabrics, is placed in a closed mold and resin is injected to cover all the empty spaces between the fibers to fabricate a composite part. The 3D permeability network created by the stack of fabrics influences the resin flow path and any variability in the local permeability from one part to the next could influence the filling dynamics resulting in voids within the composite. The local permeability variability of the fabric material is caused by the size and the distribution of the pinholes that exist in the fabric at the woven or stitched junctions.

In this work, first a method is introduced, to characterize the full 3D permeability tensor of a fabric from one experiment. Next, the local variability (pinholes) of a woven fabric is experimentally measured, and a methodology to statistically model it is formulated. The statistical properties of the pinholes are used to generate the pinhole sizes and distribution based on Monte Carlo method to conduct 3D flow simulations to investigate the dynamics of resin flow and void formation due to the presence and distribution of the pinholes. The effect of this material variability on the manufacturing process is quantified by predicting the final void content in the part numerically and validating experimentally.

Having characterized the pinholes of a woven fabric with its statistical properties,. unsupervised machine learning methods of dimensionality reduction

(Principal Components Analysis (PCA) and Stochastic Neighbor Embedding (t-SNE)) are employed to extract the statistical properties of the pinholes from an image of a woven fabric. The extracted statistical properties are then used to create the pinhole sizes and distribution to conduct 3D flow simulations to predict void formation for varying properties of the pinhole distribution within the fabric and other material and process parameters.. Five parameters (pinhole properties, permeability of fabric, permeability of distribution media, and vent pressure) were identified as important variables that would influence the void fraction and size of the voids. The results were then organized using a Decision Tree method for more efficient analysis and classification. This study should prove useful in providing the guidelines to design a robust process which accounts for the input material, process and geometric variabilities to fabricate composites without voids.

Chapter 1

INTRODUCTION

1.1 Liquid Composite Molding (LCM) processes

1.1.1 Composites

A composite is made by combining two distinct materials of different physical and chemical properties (a dry fibrous material and a liquid polymer). Dry fibrous material can be either short or continuous fiber form. For the continuous fiber form, different architecture types have been used. They include woven, random, and stitched fabrics as shown in Figure 1.1.

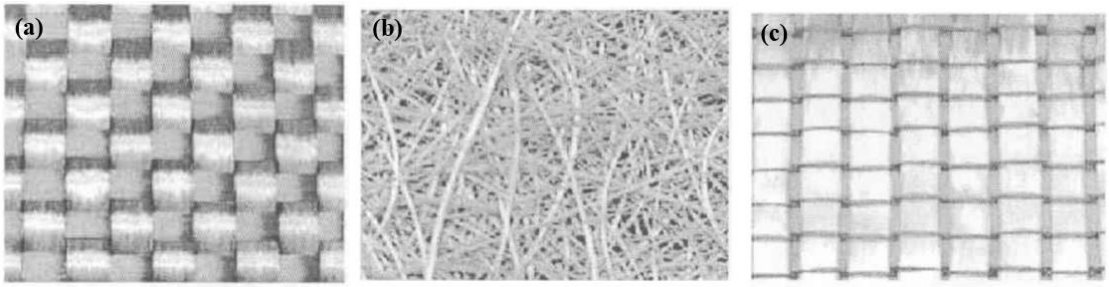

Figure 1.1 Continuous fiber forms (a) woven fabric (b) random fabric (c) stitched fabric[1]

Liquid polymer resin is introduced to cover all the gaps between the fibers to manufacture a composite. There are two types of liquid resins used: thermoset and thermoplastic. Thermoset is about 50 to 5000 times more viscous than water, whereas thermoplastic is over one million times more viscous than water. Thermoplastic although difficult to process can be recycled while thermoset undergo irreversible

chemical reaction and cannot be recycled. For this reason, the use of thermoplastic is deemed to be more environmentally friendly than thermoset. However, it's not plausible to use thermoplastic for all types of composite manufacturing processes especially in processes in which dense dry fabric needs to be injected with resin that will occupy all the empty spaces between the fibers. Hence, thermosets of low viscosity are used when impregnating dense continuous fiber systems. Liquid Composite Molding (LCM) encompasses a family of processes in which a low viscosity resin is introduced in a stationary fabric form by subjecting the resin to a pressure gradient. The resins mainly used are thermosets, and the process is widely used in industries including aerospace, automotive, civil, and marine[1]as it does allow one to make complex and net shape composite structures.

1.1.2 Family of LCM processes

Liquid Composite Molding (LCM) represents a family of composite manufacturing process in which the fabric preform is placed in a mold, the mold is closed and liquid polymer is injected into the mold and cured (hardened) to form the final composite part. LCM largely includes Resin Transfer Molding (RTM), Vacuum Assisted Resin Transfer Molding (VARTM), Seeman's Composites Resin Infusion Molding Process (SCRIMP), Injection Compression Molding, Reinforced Reaction Injection Molding (RRIM), and Structural Reaction Injection Molding (SRIM)[1]. In this work, the main focus is the SCRIMP process (VARTM with a flow enhancement media called distribution media)) but we will also introduce RTM and VARTM process to set the background.

1.1.2.1 Resin Transfer Molding (RTM) and Vacuum Assisted Resin Transfer Molding (VARTM)

The major difference between RTM and VARTM is the type of mold and pressure used to impregnate the dry fabrics with the polymer resin. The schematics of both processes are presented in Figure 1.2.

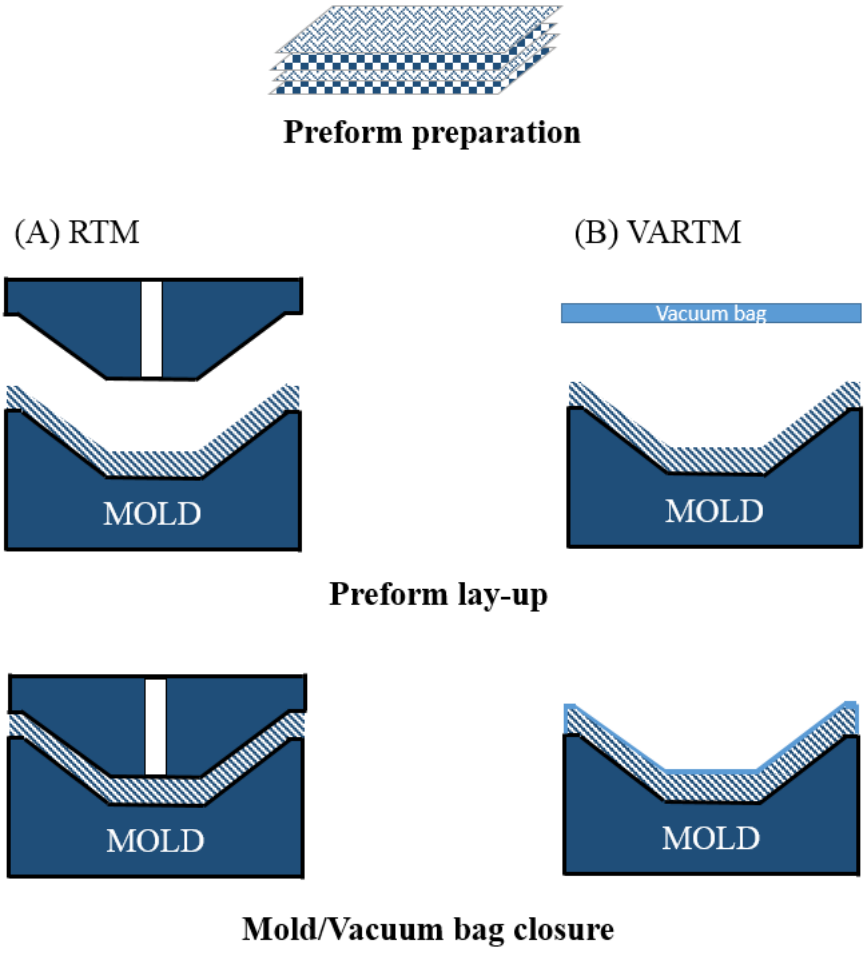

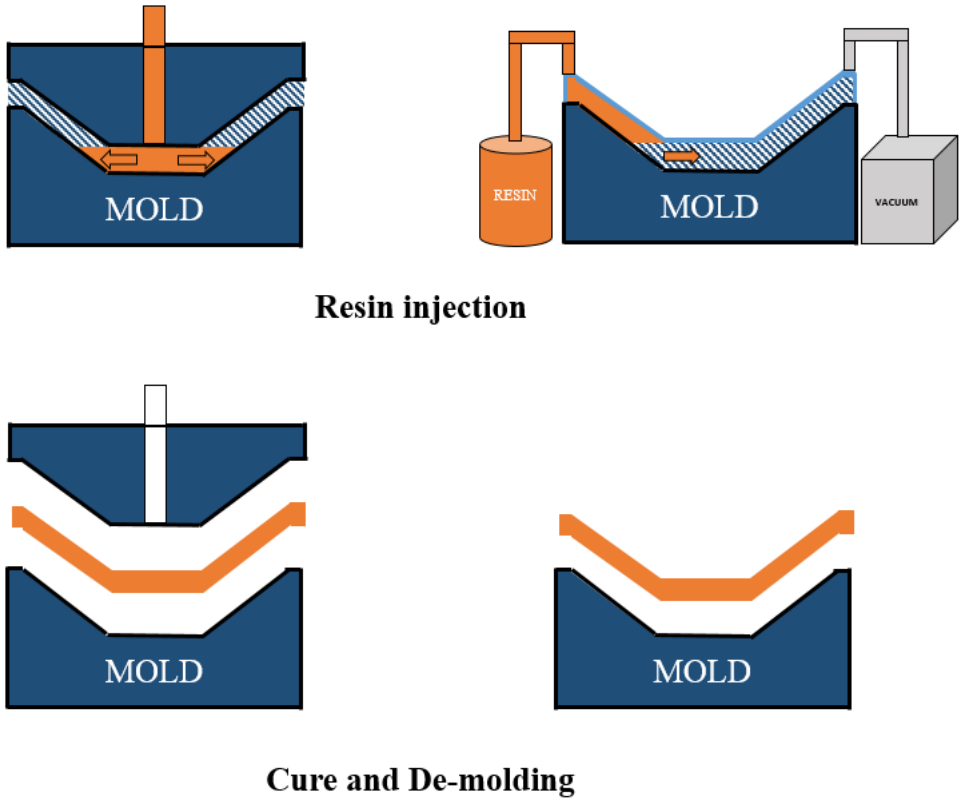

Figure 1.2 Schematic of (a) RTM (b) VARTM process

In the RTM process, a two sided rigid mold is used to enclose and compact the fabric preform to the desired fiber volume fraction. Resin is injected under positive pressure into the closed rigid mold through an opening called as the gate to impregnate the stationary preform within the mold. Once the resin arrives at the vent, the injection gate is closed and resin is allowed to cure within the mold before opening it to demold the composite part. The schematic of a RTM setting is presented in Figure 1.2 (a). Spacer plates can be used to control the final thickness of multi-layer of fabrics for permeability measurement test. The fiber volume fraction of fabrics can be manipulated by using different thicknesses of spacer plates. For an industrial manufacturing process,

hard molds are specifically made for the composite part which does not require the spacer plates for the thickness control.

The advantage of RTM process is good surface finish, short cycle time and high volume fraction of a part. The good surface finish is achieved because the solid molds are placed on both sides pressing the layers of fabric during the impregnation process. Positive pressure pushing resin through the reinforcement fabric enables the short cycle time of a process. The disadvantage of the process is high initial investment for the set-up (solid molds), especially compared to VARTM process.

The automotive, civil and marine industries have been using this technique to produce composite parts.

Figure 1.3 Example of RTM manufactured composite parts : varying composite parts (top), BMW i3 with internal structure and body of composite (bottom) [2,3]

Examples of carbon fiber reinforced composite parts which are made using the RTM process are shown in Figure 1.3(a). Figure 1.3 (b) shows BMW i3 car which is mass produced (70 vehicles a day) using the RTM process. The internal body and structure of the car are made of composite parts.

VARTM was introduced due to it low initial set up cost as one did not need a complex two sided rigid mold. The schematic of the process can be found in Figure 1.2 . The process of VARTM is as following. Dry fiber preforms are first placed on a tool surface and then enveloped within a vacuum bag. A line injection is placed at one end and a vacuum line or port is placed at the other end. A vacuum is drawn on the assembly to compact the fabric and draw the resin at atmospheric pressure into the mold due to the pressure gradient. As there is only one atmospheric pressure to drive the resin, it can take hours to impregnate a meter long part using this process which is not desirable as the resin could cure before the part is filled. Hence a slight modification was invented and labeled as (Seemann Composites Resin Infusion Molding Process)SCRIMP[4]. In this process, a Distribution media (DM) is placed on top to enhance the resin flow in the in plane direction. DM is a fabric with a very high permeability which allows resin to travel in the in-plane direction quickly. Fabrics and DM under a vacuum bag are placed under vacuum which secures the fabrics and DM in place for the infusion step. Finally vacuum is drawn to move the resin into the fibrous preform.

The advantage of this process is that it is relatively easy to scale-up the process for large composite parts such as a wind blades[5–7] and aircraft parts[8] and that the initial set-up cost is low thanks to the usage of vacuum bag and DM instead of a rigid mold on one side. The examples of composite parts manufactured using the

VARTM/SCRIMP process are shown in Figure 1.4.However, the part manufactured using the VARTM process has lower volume fraction and less complicated design than the one in the RTM process.

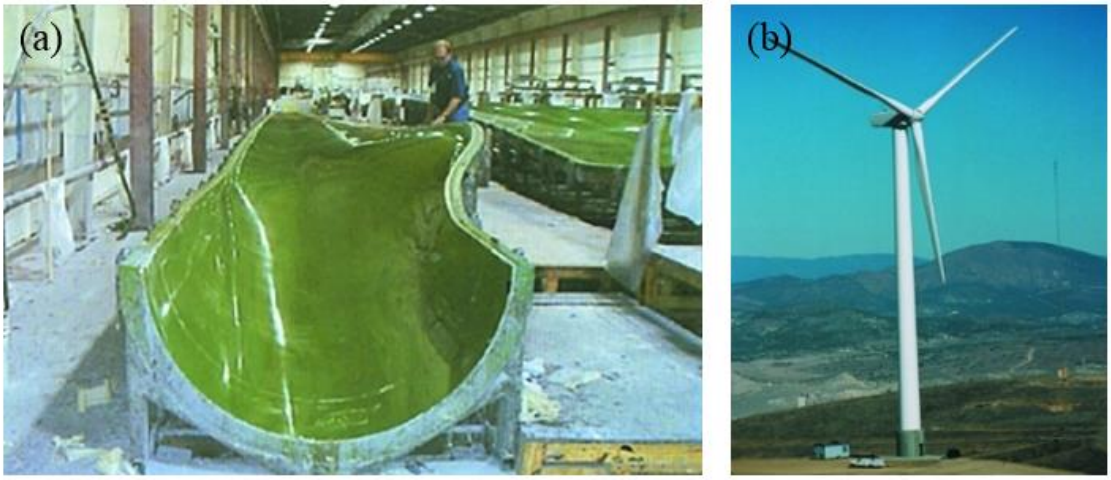

Figure 1.4 VARTM manufactured parts (a) wind blade motor (b) wind blade [9]

The quality of both processes is mainly governed by the flow dynamics of resin impregnating the dry fibrous materials. The goal is to fill all the empty spaces in the dry fabrics with resin. Therefore, it is key to understand the dynamics of resin flow to ensure high quality of the process and the final composite part.

1.1.3 Modeling of Flow in LCM Processes

In Liquid Composite Molding (LCM) processes, the flow of resin through the fiber preform can be modeled as flow of liquid through an anisotropic porous media, which Darcy's law describes as:

$$< \boldsymbol{u} >= \frac{\boldsymbol{K}}{\mu} \cdot \nabla p \tag{1.1}$$

Here **<u>** is volume averaged velocity vector, μ is the resin viscosity, ∇p is the pressure gradient experienced by the resin which drives the flow, and **K** is the permeability tensor that characterizes the resistance to resin flow in various directions due to the architecture of the porous medium. Permeability is a second order symmetric tensor with six independent components. It is a material property that describes fiber resistance to the flow of liquid. The permeability tensor is given in Equation 2.

$$\boldsymbol{K} = \begin{bmatrix} K_{xx} & K_{xy} & K_{xz} \\ K_{xy} & K_{yy} & K_{yz} \\ K_{xz} & K_{yz} & K_{zz} \end{bmatrix} \tag{1.2}$$

K_{xx}, K_{yy}, and K_{xy} are in-plane permeability components which describe the flow in the plane. K_{xz}, K_{yz}, and K_{zz} describe out of plane permeability components. K_{xy} K_{xz} and K_{yz} are skew terms which quantify the degree of misalignment between the principal directions of the fabrics and the chosen coordinate directions. **K** is a material parameter of the fabric and needs to be characterized before one can model the flow of resin in such fibrous porous media

1.1.4 Characterization of permeability tensor

There are a number of studies to characterize the permeability tensor, [10–36]. The permeability tensor has been characterized analytically and numerically by a

number of studies. Simacek et al presented a methodology to calculate K_{xx}, K_{yy}, and K_{zz} from a single experiment numerically[32]. Nedanov et al. introduced an inverse method to obtain all four components of permeability tensor (K_{xx}, K_{yy}, K_{zz}, and K_{xy}) from a single test[17]. One important thing to notice is that the through the thickness skew terms (K_{xz} and K_{yz}) are still relatively understudied and unidentified. Sas et al. are the first ones to point out the importance of the through the thickness skew terms[21]. The skew terms represent the tendency of the liquid resin to travel in skewed manner in through the thickness direction. The effect on the flow front is well described in Figure 1.5.

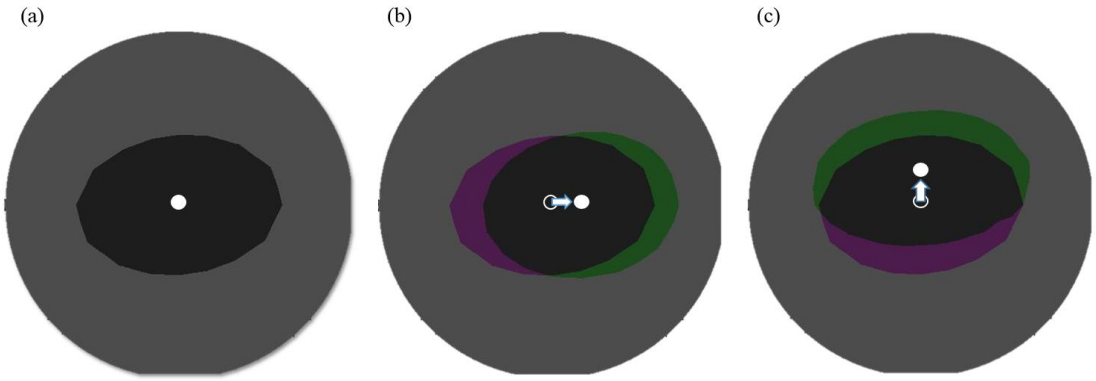

Figure 1.5 Flow front profiles on the top surface at 120s. (a) K_{xz} , K_{yz} = 0 (b) K_{xz} =5e-12 m^2, K_{yz}=0 (c) K_{xz} =0, K_{yz}=5e-12m^2 . For all simulations: K_{xx} =2e-10m^2, K_{yy} =1e-10m^2, K_{zz} =1e-12m^2, K_{xy} =1e-11m^2

The center of the flow front on the top surface shifts in the x direction in relation to the injection gate at the bottom surface with the presence of non-zero K_{xz} skew term and in the y direction with the non-zero K_{yz} skew term.

For this reason, it is important to characterize all six components of permeability tensor including through the thickness skew terms. One of the goals of this dissertation is to develop and verify a novel methodology to measure the permeability tensor with the

skew terms from a single experiment. However, such an experiment provides a homogenous global value for the permeability components for the entire fabric. In reality, the local permeability will exhibit variability and this could influence the local resin flow.

1.2 Variability in Fabric Permeability and Its Effect in LCM Process

Dry preform contains local variability due to its randomly varying geometrical properties. This could be due to manufacturing process, handling, and/or lay-up[37–39]. The example of local variability of a plain woven preform is presented in Figure 1.6. which shows the (a) original image of 6cm x 6cm plain woven fabric, (b) highlighted local variability, and (c) binary image obtained by filtering the original image. The local variability or randomly varying geometrical properties are not obvious or clear in (a). However, the variability induced by uneven width of a tow or fibers abnormally sticking out from a tow can be detected on close observation. These anomalies result in locally varying permeability field of dry fibrous preform. In addition to these factors, the meso-scale empty space between tows (pinhole) also vary in size which is well depicted in Figure 1.6(c).

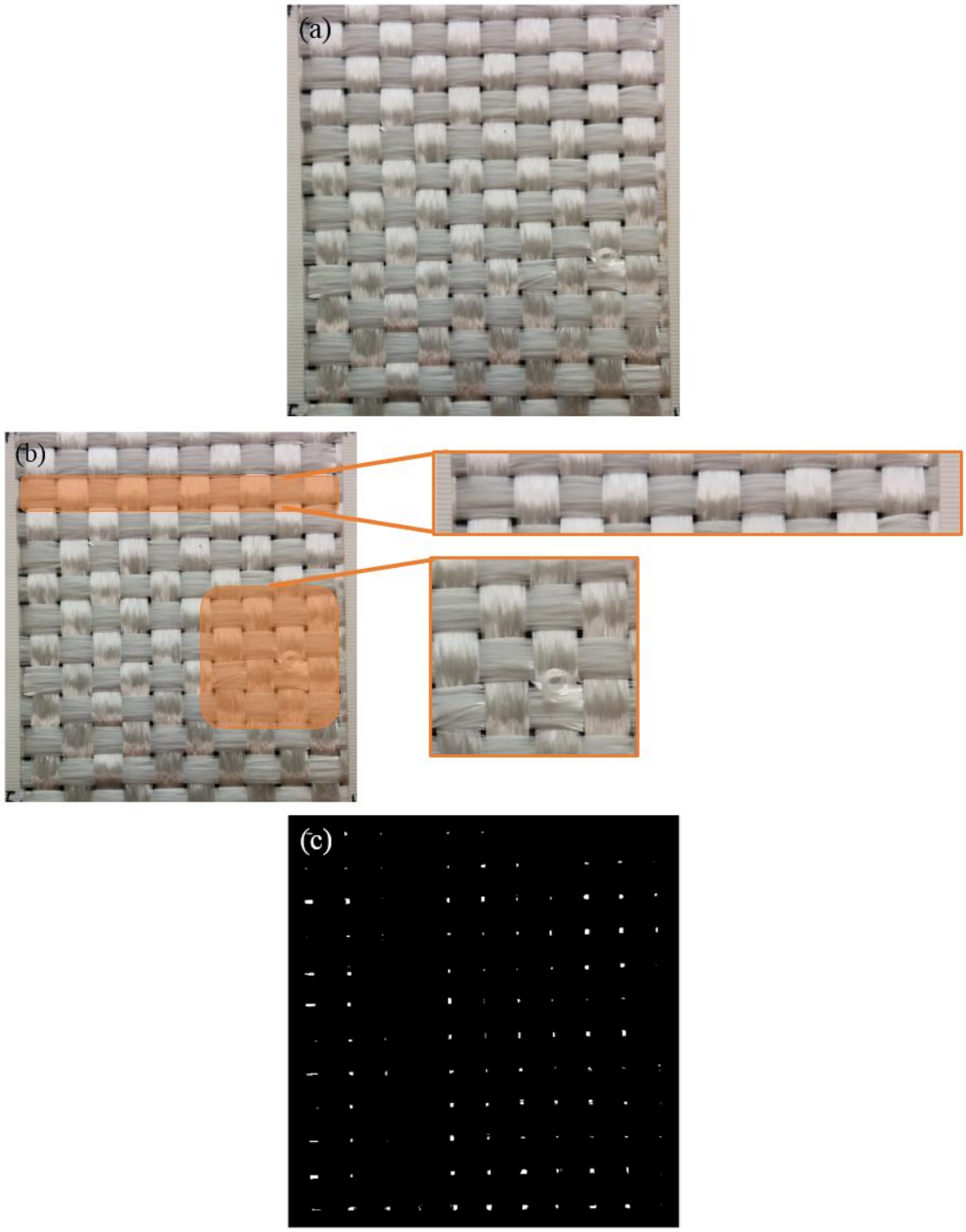

Figure 1.6 (a) Image of plain woven fabric (b) plain woven fabric with local variability (c) Binary image obtained by filtering image (a)

These random variabilities in a material can cause large changes on how the fluid impregnates the preform during the impregnation step of the manufacturing process. Especially, the pinholes of varying size directly affect the resin flow in through the thickness direction which results in air entrapment (dry spots, or voids). Void is a region of the preform that failed to fill with the resin during the impregnation process. Voids are undesirable as they act as stress concentrations and can initiate failure of the component. The progress of resin flow in the presence of pinholes is depicted in Figure 1.7. In this example of the VARTM (SCRIMP) process, a total of four layers of dry woven fabrics with pinholes were first placed on an acrylic plastic mold and then the DM was placed on top of the 4 layers. The acrylic mold allows visual access to the impregnation process. A camera was mounted at the bottom to record the filling. Figure 1.7 shows the images of the bottom layer at different times.

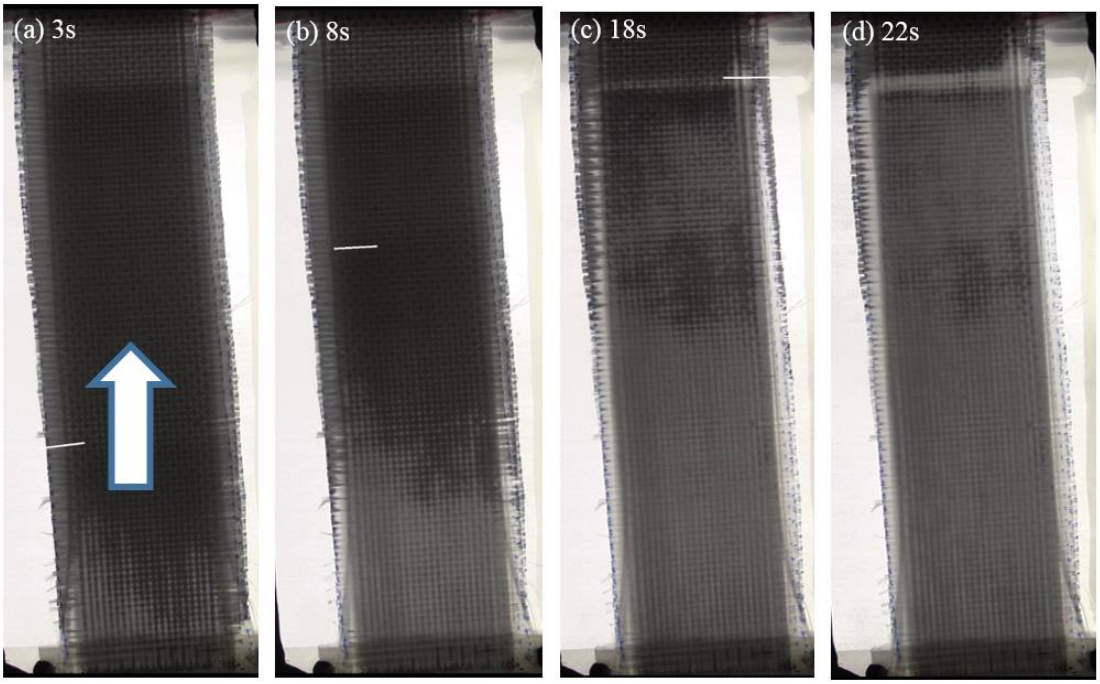

Figure 1.7 Progress of resin flow filmed from the bottom during the SCRIMP process at advancing times (a) 3s (b) 8s (c) 18s (d) 22s from the beginning of the injection. White indicates resin and black indicates voids. Resin flows from bottom to top

As there is a distribution media on top, the resin can fill the top face much faster than the bottom layers, The flow front is uneven as the resin from the distribution media can arrive at the bottom layer through the pinholes before the resin impregnating the bottom layer arrives there. As the flow fronts emerging from the pinholes merge with the flow front impregnating the bottom layer, it will entrap the air and create a void. Figure 1.8 shows (a) the last image at 22s and (b) its filtered image. One can clearly see the voids in Figure 1.8 (b) in the pink background in the filtered image.

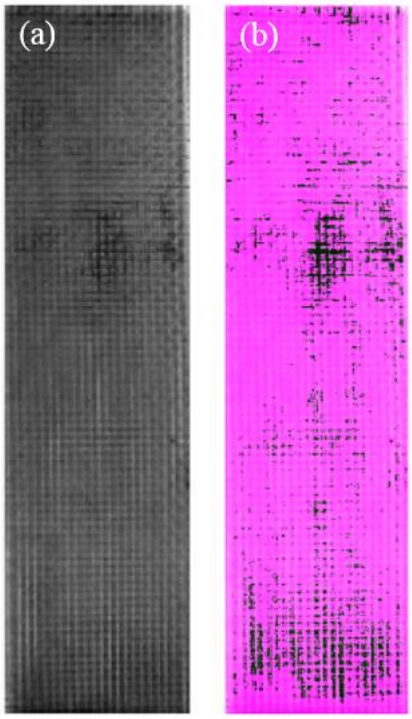

Figure 1.8 (a) Image of the bottom layer at 22s in the SCRIMP process. Black indicates voids and light region shows the resin. (b) Filtered image clearly shows the dark void regions and the pink resin regions

Hence, it is important to predict the effect of this variation on the manufacturing quality of the composite part.

Although many of possible cause for the variability have been identified in published works [18,37–68], most of the studies of the heterogeneous (stochastically varying) permeability field of a fibrous material are focused on characterization of randomly varying in-plane permeability. Markicevic et al. were the first ones to address [43] tthe influence of stochastically varying through the thickness permeability of a woven fabric.

Another goal of this dissertation is to better understand the stochastically varying through the thickness permeability field of a woven fabric and its relation to other manufacturing parameters such as DM permeability.

1.3 Dissertation Overview

The scope of the work presented here is to develop a method to characterize all 6 components of bulk permeability and to understand, model and finally predict the resin flow into a reinforcement with random heterogeneity in through the thickness permeability in LCM processes. The objective of this dissertation is to characterize and model the random fields induced by pinholes in through the thickness direction which can help to predict the resin flow and develop a robust LCM process that manufactures composites without voids despite the presence of the variations in the permeability of a fabric.

There are several steps required to achieve the proposed objective : (a) to formulate a methodology to measure and determine the permeability tensor including skew terms (K_{xz}, K_{yz}) to predict the resin flow in a homogeneous fabric (b) to identify and confirm the cause of heterogeneity in through the thickness permeability of a fabric experimentally and numerically, (c) to develop a novel way to generate the random field of the heterogeneous permeability field by investigating its statistical properties, and (d) to develop a methodology to enable users to quickly determine and characterize the degree of the heterogeneity of a desired fabric sample..

Chapter 2 introduces a methodology developed to obtain all six components of permeability tensor including K_{xz} and K_{yz} from a single experiment. The importance of

the influence of skew terms in influencing the through the thickness and in plane flow is presented and the methodology is explained in detail.

In Chapter 3, the cause of heterogeneity in through the thickness permeability of a woven fibrous material is identified and implemented into a numerical simulation. The effect of heterogeneity in through the thickness permeability on resin flow and void formation is investigated experimentally and numerically. The effect of randomly varying permeability field on void formation (air entrapment) in LCM processes is studied with varying DM permeability.

Chapter 4 characterizes the random field of through the thickness permeability of a woven fabric using statistical analysis. With the methodology to create the random field with key statistical properties. Monte Carlo (MC) simulations are carried out to characterize the void distribution and compare it with the experimental results

In Chapter 5, a machine learning method of dimensionality reduction is utilized to identify the key statistical properties of the permeability field of a fabric in the through thickness direction from its image. Using Principal Component Analysis (PCA), the dimensionality of the binary images is reduced to three. A decision tree approach is introduced in Chapter 5 to forecast the possible void fraction and void distribution to expect from a binary image of the fabric architecture before introducing resin in that preform architecture.

In Chapter 6, a parametric study is introduced to investigate the effect of pinholes along with other process parameters on the void formation in a VARTM process. Pinhole properties, fabric permeability, Distribution media permeability, and vent pressure are parameters chosen to study its effect on resin flow. Monte Carlo numerical simulations are carried out and of the resulting size of voids or void fraction

are obtained. The results are then classified using the Decision Tree approach for easy visualization and approach.

Final chapter summarizes the original contributions of this work and presents possible pathways for continuation of this approach to improve manufacturing processes of composite materials.

Chapter 2

CHARACTERIZATION OF 3D FABRIC PERMEABILITY WITH SKEW TERMS

2.1 Introduction

Permeability tensor is an important input parameter in the simulation to describe the flow behavior of the resin during mold filling. For this reason, many studies on characterizing the permeability of a reinforcement fabric have been carried out [14–18,21,24,25,32,33,69,70]. In-plane principal permeability values were measured experimentally by 16 different methods in the study by Arbter et al. [69]. Ken han et al.[25] developed a new method to measure in-plane principle permeability components of fiber preforms with high volume fraction using pressure transducers. Okonkwo et al.[17] developed a methodology to obtain four permeability values (all in-plane permeability components and through the thickness permeability) from a single experiment. In-plane and through the thickness permeability were studied in depth by the researchers, however, the skew terms (K_{xz} and K_{yz}) for thick parts have not been addressed. Sas et al.[21] are the first ones to consider the effect of through the thickness skew terms on the flow front. Through the thickness skew term, if present, can affect the resin flow dynamics in LCM process to a significant degree as shown by examples simulated in Figure 2.1.

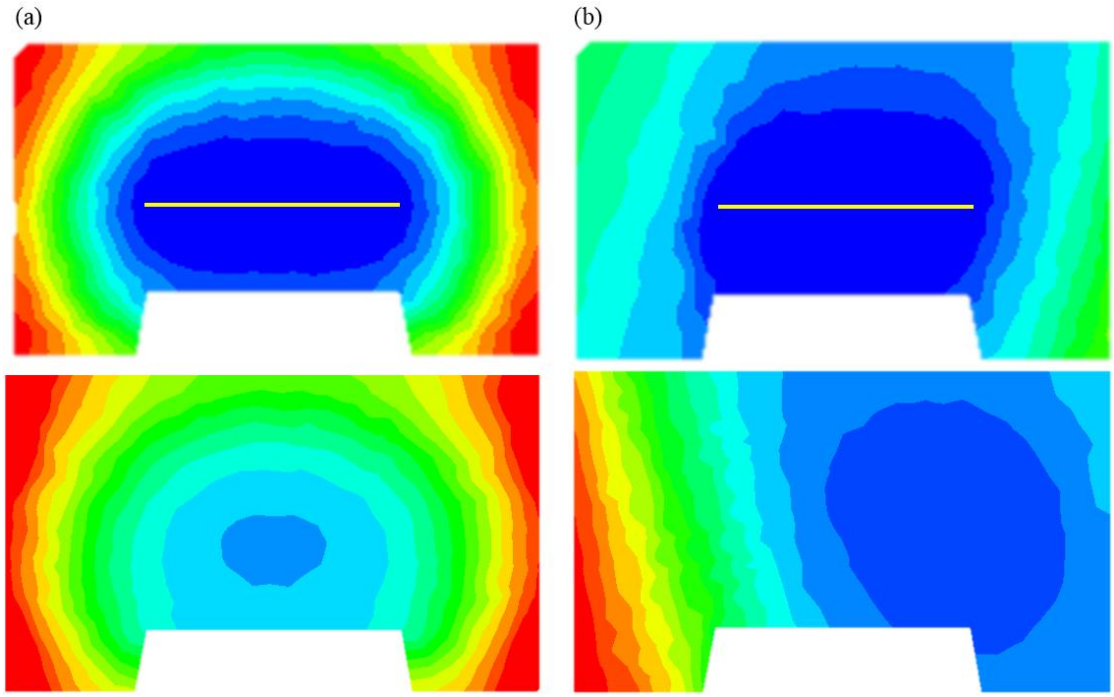

Figure 2.1 Flow front profiles along the top (upper picture) and bottom (lower picture) surfaces of a 3D geometry (a) K_{xz} , K_{yz} = 0 (b) K_{xz} = 7e-12 m^2 K_{yz} = 7e-12 m^2 For both simulations: K_{xx} =1e-10m^2, K_{yy} =1e-10m^2, K_{zz} =1e-12m^2, K_{xy} =0.

Figure 2.1shows the effects of transverse skew terms on resin flow patterns during impregnation into a complex 3D geometry. Resin is introduced from the center line gate which is located on the top side. Colors in the figure signify the arrival time of the resin at that location. Blue represents early times and red is later times. In Figure 2.1 (a), the flow fronts advance from the line gate reaching the edge of the trailer evenly at the same time along the top and the bottom. When through the thickness skew terms are introduced in the simulation in Figure 2.1(b), the flow fronts along the top and the bottom show substantial difference in the filling pattern which could lead to voids (air entrapment) if the resin arrives at the vent before the preform is completely saturated.

Thick 3D preforms due to a complex weaving pattern exhibitasymmetric flow in the thickness direction which can be predicted if the skew terms from a permeability

characterization experiment are provided as an input to the flow simulation. Hence, skew terms along with in-plane and transverse permeability of a preform should all be characterized to better understand resin flow behavior in LCM processes. In this section, we present an algorithm that optimizes the flow front positions recorded from a permeability measurement station to obtain all six independent permeability components of the second order permeability tensor from a single experiment.

2.2 Approach

2.2.1 Methodology

Figure 2.2 describes the methodology used to characterize the permeability tensor of the fabric from a single experiment.

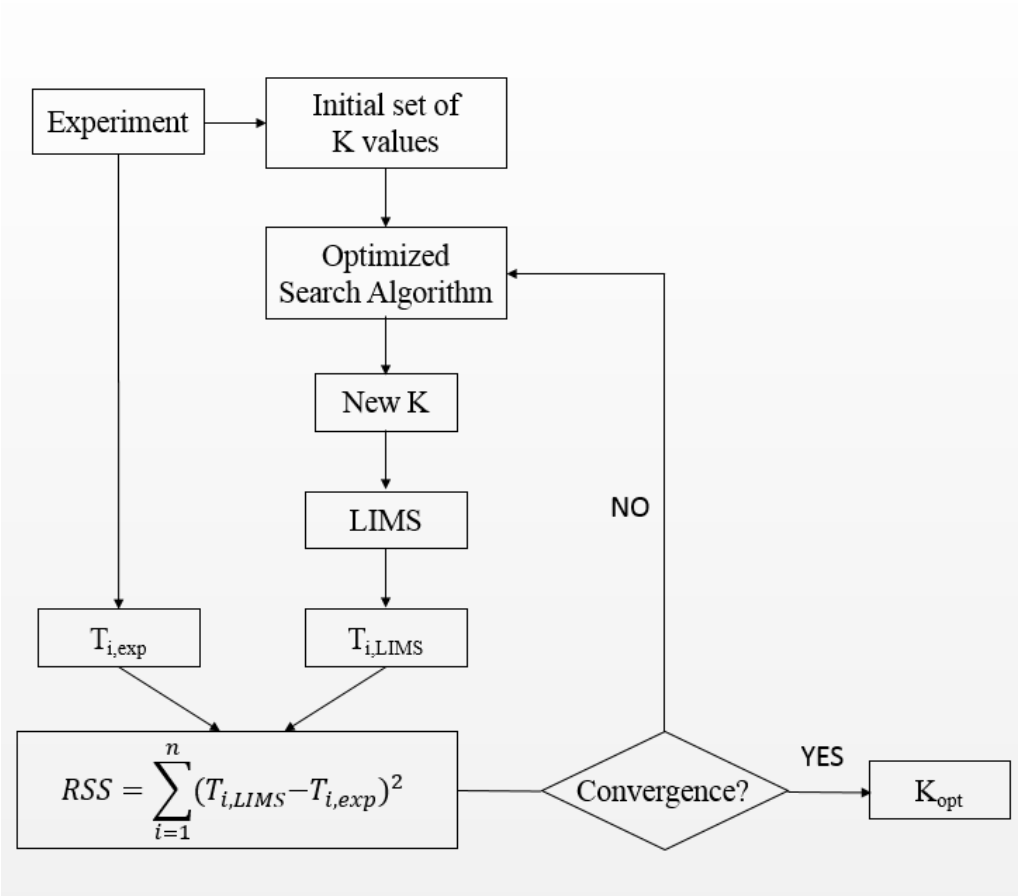

Figure 2.2 Methodology for characterization of all six independent components of the permeability tensor from a single experiment.

The methodology consists of two steps. The first step involves conducting a 3D flow experiment with a central injection gate on the bottom surface in a transparent mold. The movement of the flow front of the resin on the top and bottom side is recorded with two digital cameras. The images captured by digital cameras from the experiment are automatically processed to obtain resin flow front information at various times and to estimate initial set of three in-plane permeability components (K_{xx},K_{yy}, K_{xy}). Initial through the thickness permeability components (K_{zz},K_{zx},K_{zy}) are calculated using the grid method and image processing information. The second step uses this initial set of six permeability values as an input in LIMS (Liquid Injection Molding Simulation)

which is used to describe the flow behavior of the resin in a 3D mold. LIMS is a finite element/control volume based simulation program that uses Darcy's law to predict the flow pattern within a porous preform as a function of time. The details and capabilities of LIMS are described in Appendix A. Other input values in addition to the six components of the permeability tensor for the flow simulation are viscosity, inlet pressure or flow rate, and the fiber volume fraction. LIMS numerically simulates the flow of resin with the same geometry and the inlet location as the experimental case. The flow front arrival times from the LIMS simulation are compared with the experimentally recorded flow fronts and the Residual Sum of Squares (RSS) between the two *at all time steps* is calculated.

$$RSS = \sum_{i=1}^{N} (\left(T_{i,exp} - T_{i.lims}\right)^2) \tag{2.1}$$

Where, N is the number of nodes filled with resin, $T_{i,exp}$is a resin arrival time at each node during the experiment, and $T_{i.lims}$ is the arrival time calculated using LIMS. The permeability values in the LIMS simulation are systematically updated using the simplex optimization search algorithm. The coupled system of LIMS and the simplex search algorithm work in tandem to minimize the RSS. When the relative error between the fill times from the numerical simulation and experiments is less than 5 %, the permeability component values are deemed to be found and the search is ended.

The next two sections describe the experimental and the search algorithms in detail.

2.2.2 Experimental

Figure 2.3 is a schematic describing the experimental setting. First, fabrics are weighed to calculate the volume fraction and viscosity of resin to be injected is measured. The fabric reinforcement is placed between two transparent acrylic molds with a spacer plate in between creating a picture frame mold as in a Resin Transfer Molding setting (RTM). The fabric is compressed and clamped until the top and the bottom surface of the mold are flush with the spacer plate. The resin from a pressurized tank under constant pressure is injected through the center gate in the bottom mold. Simulated resin (corn syrup) is used here because it is as viscous as a resin and easy to clean after the experiment is completed. Also, as the interest of the study is to investigate the flow behavior of resin, the use of corn syrup is valid and well known way to simulate resin flow. The resin flow along the top and bottom surface is recorded through the transparent acrylic mold by two cameras mounted over the surfaces during the impregnation of resin into the fabric as shown in Figure 2.3.

Once the images are obtained from the experiment, they are analyzed to calculate initial in-plane permeability components as explained in the next section of the image processing step.

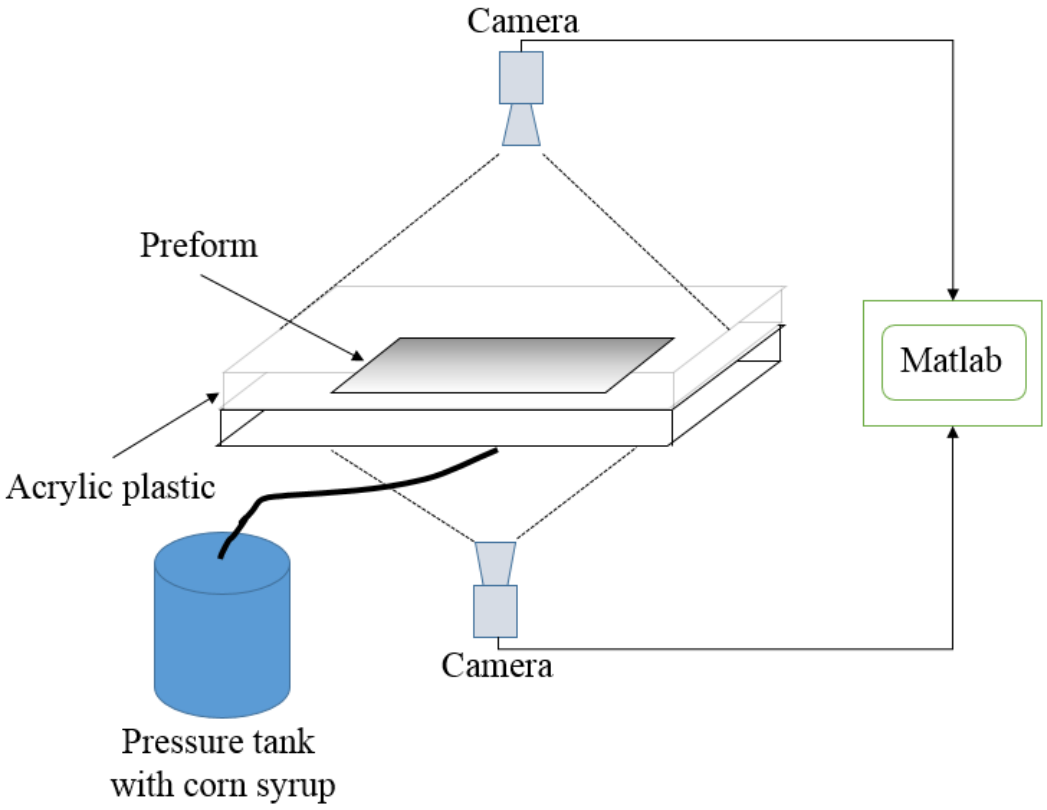

Figure 2.3 Schematic of the experimental set up to characterize six independent components of the permeability tensor of a fiber preform from one experiment.

2.2.3 Image Processing

After the experiment is recorded, the flow fronts in the images as seen from the top and the bottom surface at various times are fitted with ellipses with a least-squares fit method using MATLAB. This allows one to obtain the resin arrival time at any location. The accuracy of the methodology is confirmed by comparing the nodal fill time calculated from the image processing to the assigned fill times. The average relative error between the calculated fill time from the fitting of the ellipse and the known fill times was found to be less than 5%. The semi-major and minor diameters, the angle of rotation, and the centroid location of the ellipse are also generated in this

step. This information is used to determine the initial set of in-plane permeability components (K_{xx},K_{yy}, and K_{xy}) using the analytical solution for resin flow in 2D. These permeability values are not final for 3D flow, they serve as a good starting point for the six parameter optimization search. The semi-major and minor diameters of the fitted ellipse at different times are input values to calculate in-plane permeability (K_{xx} and K_{yy}). The rotation angle is directly related to the magnitude of in-plane skew term (K_{xy}). The initial in-plane permeability (K_{xx},K_{yy}, and K_{xy}) are calculated using the equations (2.2) – (2.4) [17]

$$K_{xx} = \frac{\mu\emptyset}{6\Delta p}\left[\frac{2x_f^3}{r_0} - 3x_f^2 + r_0^2\right]\frac{1}{t_{fx}} \tag{2.2}$$

$$K_{yy} = \frac{\mu\emptyset}{6\Delta p}\left[\frac{2y_f^3}{r_0} - 3y_f^2 + r_0^2\right]\frac{1}{t_{fy}} \tag{2.3}$$

$$K_{xy} = \frac{1}{2}(K_{yy} - K_{xx})\tan(2\theta) \tag{2.4}$$

Here, the r_0 is the inlet radius, x_f and y_f are the flow front positions along x and y axis at times t_{fx} and t_{fy}. The Δp is the applied pressure difference driving the simulated resin through a preform, μ is the viscosity of the impregnating resin, and $\emptyset$ is the porosity in the mold. θ is the angle which represents the orientation of the flow front ellipse with respect to experimental set-up axis.

The algorithm to find the optimal values needs an initial value for all the six independent components of the permeability tensor. Through the thickness permeability components K_{xz}, K_{yz}, and K_{zz}, are obtained through grid search method described in the next section using the same image processing information.

The advantage of this image processing method is that it is easy and simple to use. For example, Okonkwo et al.[17] reported that 192 sensors installed on the top and bottom molds were used to obtain the resin arrival times. The maintenance of sensors is challenging and also makes cleaning of the mold difficult because some of resin gets embedded in the sensors even after cleaning, which compromises the accuracy of the measurement. Compared to the method using sensors, image processing requires only two cameras which makes the methodology convenient. However the downside is that one must use molds that have a transparent window.

2.2.4 Grid Search Method

The Grid method was introduced because a good estimate of the initial value for through the thickness components (K_{xz}, K_{yz}, and K_{zz}) is crucial to prevent the optimization search with the simplex method from getting trapped in a local minima. Finding a global minima without getting trapped in a local minima has been an important issue for simplex algorithms. There have been multiple efforts to improve the *Nelder Meade simplex method*. [71–74]. Chelouah and Siarry[71] proposed a new hybrid method composed of a genetic algorithm and simplex search to resolve the issue in 2012. The hybrid method is called *Continuous Genetic Algorithm* (CGA). In CGA, a promising population is found first using a genetic algorithm. Later, Chelouah and Siarry employed a new hybrid method combining a *Tabu* search and the *Nelder Meade simplex search* to address the issue of local minima. *Tabu* search is described in the journal by Hertz and Werra et al.[75] The combination of the two search methods ensured the localization of the promising region with a global minima [71,72].

In this study, grid method conducted an initial search in the most promising region to provide a global minima and was implemented before the simplex search step to prevent the simplex search from being trapped in a local minima. The initial search using the grid method, is carried out by estimating through thickness skew terms from what is known about the flow along the top and the bottom surface. First, the ratio between K_{xz} and K_{yz} is obtained from the center shift of flow front appearing on the top side compared to the bottom side from the experimental results. The ratio of x-shift and y-shift gives the ratio between K_{xz} and K_{yz} (as is clear from Figure 2.1). This reduces 6 variable optimization to 5 variable optimization problem.

$$K_{yz} = K_{xz}R \tag{2.5}$$

Here, the ratio, R is defined as the distance of the center of the ellipse on the top surface from the injection location along the bottom surface in the x direction to that in y direction as can be seen in Figure 1.5

Initial $K_{zz,ini}$ and $K_{xz,ini}$ are defined as follows

$$K_{zz,ini} = \frac{0.01\left(K_{xx} + K_{yy}\right)}{2} \tag{2.6}$$

As the through thickness K_{zz} is usually two order of magnitude smaller than in plane permeability.

$$K_{xz,ini} = \sqrt{K_{xx}K_{zz}} \tag{2.7}$$

$K_{xz,ini}$ is calculated using Equation 2.7 as it needs to satisfy positive definite condition as permeability cannot be a negative value .

The grid search method takes the initial $K_{zz,ini}$ and $K_{xz,ini}$, values and searches for the optimal initial guess in its neighborhood as shown in Figure 2.4. $K_{zz,ini}$ is varied from 0.1 $K_{zz,ini}$ to 1.5 $K_{zz,ini}$ while $K_{xz,ini}$ is varied from 0.1 $K_{xz,ini}$, to $K_{xz,ini}$ to create the input set for LIMS along with the other permeability components defined by equations 2.4-2.7. The results are compared with the experimental arrival times at the nodes and RSS is calculated for each grid point as shown in Figure 2.4.

The set of permeability (K_{zz}, K_{xz}) that yields the lowest RSS value is chosen as the initial guess along with Equation (2.4-2.7) initial values for the simple method. This is a necessary step to ensure successful convergence of simplex search to find a global minima which will provide us with the six independent permeability components that match the experimental flow arrival times along the top and the bottom surfaces at various time steps.

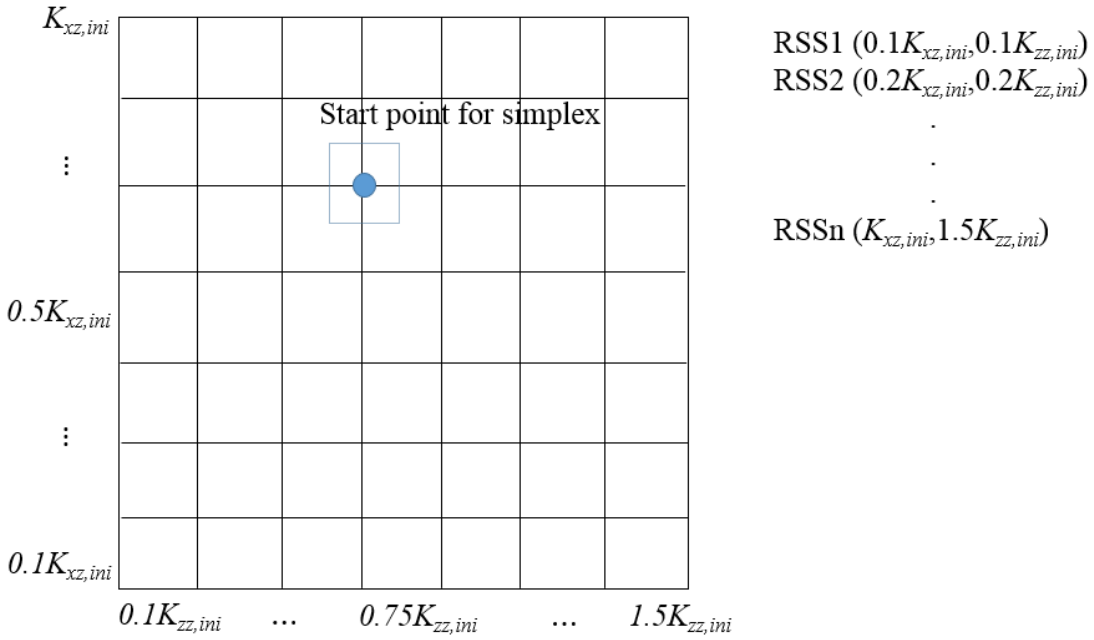

Figure 2.4 Grid search method to find the best initial guess for $K_{zz,ini}$ and $K_{xz,ini}$. $K_{zz,ini}$ is varied from $0.1K_{xz,ini}$ to $1.5K_{zz,ini}$, $K_{xz,ini}$ is varied from 0.1 $K_{xz,ini}$ to $K_{xz,ini}$

2.2.5 The Simplex Method

Simplex method can minimize a function of *n* variables. Simplex is a convex hull with *n+1* vertices in *n* dimensions. The function of *n* variables is minimized through a transformation of the simplex convex hull figure through reflection, contraction, and extension. *n* vertices of the convex hull without an origin vertex decides the vector direction for the transformation. Function values at the *(n+1)* vertices of simplex are compared and the vertex with the highest function value is replaced by another point. The process is terminated when the function value is minimized which satisfies the assigned tolerance. It is a very powerful and quick method that can optimize a function of a large number of variables. [76] Okonkwo el al. chose a golden

search method for 4 variable optimization. [17] When the golden search method was implemented to optimize a function of 6 variables, the operation time took more than 10 hours. The slow convergence is a well-known drawback of a golden search method with more than 3 variables. Simplex can deal with multiple variables in a comparatively shorter operation time of a couple of hours.

For the final step in the optimized methodology, the simplex search begins with the initial set of six permeability components as determined from the grid search method as described in the previous section. The simplex algorithm then continues to minimize the RSS of fill times between the experiment and the simulation at various time steps. When the average of relative error of all fill times becomes less than 5%, the simplex search is deemed to be converged and the search is terminated. The entire system is automated in that image processing, grid method, and simplex are all coded and linked together in MATLAB program coupled with LIMS. Once the images are recorded from an experiment, the entire algorithm can be carried out automatically and when converged will report the six independent components of the permeability tensor.

2.3 Results

The presented algorithm is validated through virtual and actual experiments.

2.3.1 Virtual Experiment

The accuracy of the developed algorithm as described in the previous section was evaluated numerically with LIMS simulation data. First, a set of six permeability components listed in Table 2.1 was assigned as an input to LIMS along with the experimental process parameters which are provided in Table 2.2. With these material

and process parameters, LIMS simulates the resin flow in the geometry of the experimental mold. LIMS records the time of arrival at each node when the resin fills that particular nodal control volume. In this way, the nodal arrival times (nodal fill times data) are generated.

Table 2.1 Assigned set of six components of fabric permeability used in the experiment

	K_{xx} (m^2)	K_{yy} (m^2)	K_{zz} (m^2)	K_{xy} (m^2)	K_{xz} (m^2)	K_{yz} (m^2)
Value:	2e-10	1e-10	1e-12	1e-11	5e-12	5e-12

Table 2.2 Parameter values for LIMS simulation

Parameter:	Numerical value:
Inlet pressure(pa)	10^5
Volume fraction (%)	40
Viscosity of resin(pa*s)	100

Transverse skew terms (K_{yz} *and* K_{xz}) are assigned with a moderate value to test the search-ability of the algorithm in the presence of skew terms. Visual images of simulated flow fronts from LIMS at different times were captured into image files as if they were recorded experimental images to be used later for image processing. From the image processing data, the found initial set of permeability is optimized by the simplex search.

The result in Table 2.3 shows the prediction is within 2% of relative error. The superimposed flow fronts presented in Figure 2.5 shows a good agreement between predicted and numerically calculated flow fronts. One important point to notice in Figure 2.5 is the shift of origin in the presence of skew terms as pointed out earlier. The shift of origin occurred both in x and y direction with both skew terms. The algorithm accurately predicted all of the six permeability components and converged in less than two hours of CPU time with a PC computer.

Table 2.3 Predicted permeability (m^2) and its relative error (%)

	K_{xx} (m^2)	K_{yy} (m^2)	K_{zz} (m^2)	K_{xy} (m^2)	K_{xz} (m^2)	K_{yz} (m^2)
Predicted Permeability (m^2)	1.97e-10	9.8e-11	9.9e-13	1e-11	5.01e-12	4.98e-12
Relative Error (%)	1.05	1.16	1.05	0.05	1.03	1.06

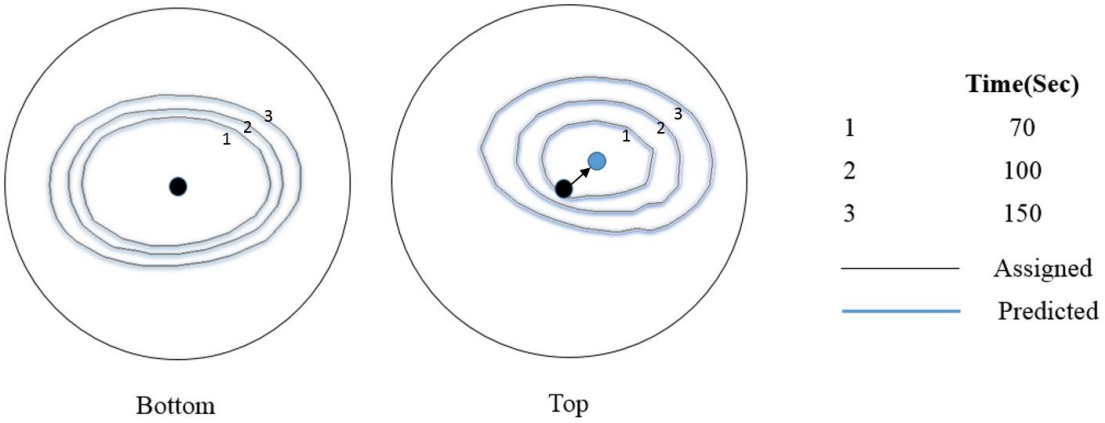

Figure 2.5 Predicted flow fronts superimposed on numerically obtained flow fronts along the top and the bottom surface at time of 70, 100,150s. Black dot represents the inlet gate.

2.3.2 3D Fabric Permeability Characterization

3D woven E-glass fabric with 6230 g/m^2 aerial density was used as a reinforcement sample. Two layers of the fabric were used and the spacer plate of 0.18" was used. Corn syrup was used as a simulated resin for convenience. Radial experiment was carried out in the setting described in Figure 2.3. Experimental conditions are displayed in Table 2.4. The proposed methodology was used to characterize the

permeability tensor. The results are presented in Figure 2.6, Figure 2.7, and Table 2.5. Figure 2.6 shows the experimental flow front, the flow front from numerical simulation with predicted permeability and the comparison at 6s between the two for both the top and bottom side.

Table 2.4 Experimental conditions for the permeability characterization test

Parameter:	Numerical value:
Inlet pressure (pa)	10^5
Volume fraction of E-glass	0.54
Viscosity of corn syrup(pa*s)	0.98
Diameter of injection hole (cm)	1.27
Mold size (cm x cm)	30.48×30.48

Table 2.5 Predicted six components of permeability tensor of 3D glass fabric

	K_{xx} (m^2)	K_{yy} (m^2)	K_{zz} (m^2)	K_{xy} (m^2)	K_{xz} (m^2)	K_{yz} (m^2)
Numerical value:	3.2e-10	2e-09	4e-12	6.7e-14	7e-12	4.5e-12

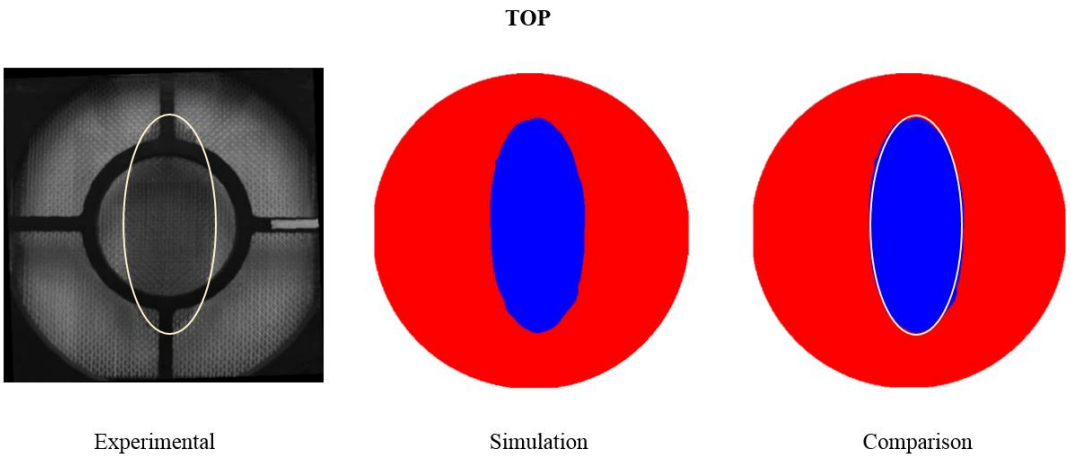

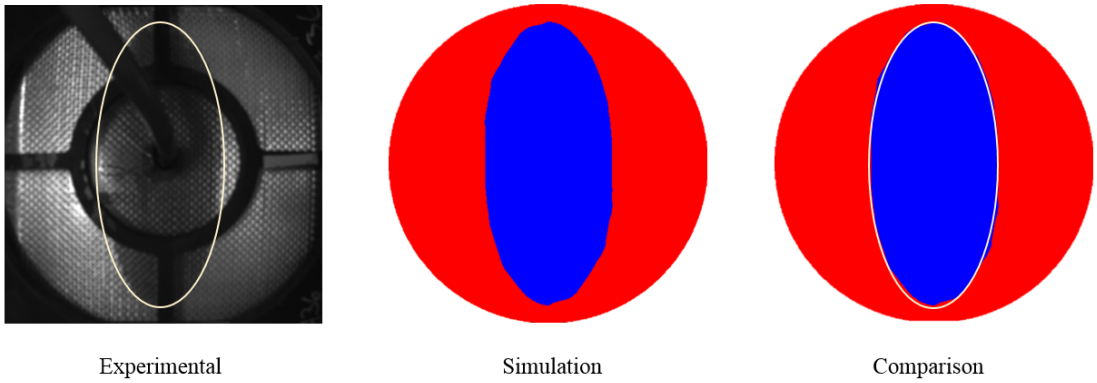

Figure 2.6 Experimental flow front, the flow front from numerical simulation with predicted permeability and the comparison at 6s between two for both the top and bottom side

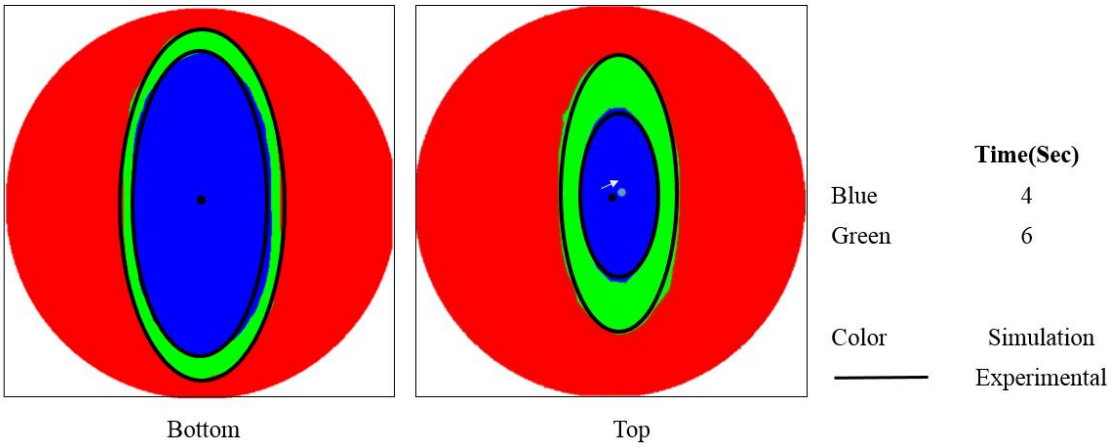

Figure 2.7 Predicted flow fronts superimposed on experimental flow fronts on the top and bottom at different times

The superimposed images from experiment and numerical simulation are presented in Figure 2.7. The experimental result shows a good agreement with predicted flows on both the top and bottom sides. The predicted set of permeability seems reasonable based on the shape of the flow front on the bottom and top surfaces. Firstly, K_{xx} is about 6 times smaller than K_{yy}, which can be explained by the ellipse shape

extended in the y-direction. The square of the ratio of major to minor axis of ellipse gives a good approximation of K_{yy} to K_{xx} ratio. The ratio of major axis of an ellipse at 6s in y direction to minor axis in x direction is found to be 2.3. The square of the ratio is about 5.5 which shows a good approximation for the ratio of predicted in plane permeability ratio of 6.25. As the measured rotation angle of the ellipse is 0.6° on average with respect to the coordinate direction, we would expect K_{xy} to be insignificant. The result shows that K_{xy} is four orders of magnitude smaller than other in plane permeability component confirming what is observed that the principal directions of the fabrics are very much aligned with the coordinate direction in the x-y in-plane direction. K_{yz} and K_{xz} causes a shift of the center of the ellipse on the top side. The measured center shift of ellipse on the top is 8.5 mm in the x direction and 6.5mm in the y direction. The shifts of the center of the top side ellipse in both directions explains the significant skew terms which are of the same order as Kzz. The result of this study shows that the permeability set of 3D fabric can possess the skew terms which causes resin to flow in skewed way in through the thickness direction as was shown in Figure 2.1. Hence, it is essential to identify all six components of permeability set to fully understand resin flow through unbalanced and 3D fabrics during LCM process.

2.4 Summary and Conclusion

An optimized algorithm has been developed to find all of the six independent components of the permeability tensor of a fiber preform from a single experiment. A 3D radial flow experiment was developed to record the movement of the flow front along the top and the bottom surface. With image processing algorithms information about the flow arrival times at various locations and the shape of the ellipses along the

top and bottom could be extracted automatically. Initial values of the six independent components of the permeability tensor were successfully found with analytical 2D solution, image information captured via recording the movement of the flow front through transparent mold walls along the top and the bottom surface, and the grid search method. The simulation resin flow arrival times were compared with the experimental values at all time steps with the goal of minimizing the error. The grid search method allowed the simplex search to reach a global minima without getting trapped in a local minima. The proposed methodology demonstrated fast convergence and was able to predict the permeability values accurately. Simplex method was found to be highly advantageous with ability to optimize more than 3 variables at a time over other search methods such as golden search method.

This novel methodology was used to characterize a plain woven fabric with pinholes with 6 components of bulk permeability. The bulk permeability is the essential part for numerical simulation to study the behavior of resin with presence of pinholes which are the main cause of variability in through the thickness permeability and a leading cause for voids during manufacturing with SCRIMP process which will be addressed in the next chapter.

Chapter 3

STOCHASTIC MODELING OF THROUGH THE THICKNESS PERMEABILITY VARIATION IN A FABRIC AND ITS EFFECT ON VOID FORMATION DURING VACUUM ASSISTED RESIN TRASFER MOLDING (VARTM)

3.1 Introduction

It is a well known that higher the value of the DM permeability, K_{DM}, faster will be the filling process during Vacuum Assisted Resin Transfer Molding (VARTM) process. However, one must explore the influence of this higher DM permeability on the flow dynamics and void formation because void formation is undesirable for the part and will eventually lead to lower yield. In this process, resin flow is largely affected by variation in through the thickness permeability of a woven fabric when distribution media (DM) is placed on top of the reinforcement. The variation in through the thickness permeability of a woven fabric is caused by the pinhole regions around the junctions of fiber tows. The variation in the pinhole regions can create uneven flow along the bottom surface of the mold and thus trap voids or dry regions. Process modeling and simulation of resin flow in such processes have improved our understanding of how flow patterns can dramatically change because of variability in fabric permeability [77–79]. These values of permeabilty exhibit significant variations [31,80] due to many factors, such as fiber architecture, spacing and angle variations [47,63,64]. The variability in the permeability values is responsible for anomalies in the resin flow that can cause voids in the final composite. A number of studies[46–48,61,63–65,81,82] described the variability in fabric permeability and have

characterized its effect on resin flow. However, most of the studies conducted so far have investigated in-plane permeability (K_{xx} and K_{yy}) variations but not through the thickness permeability (K_{zz}) variations. Markicevic et al.[43] were the first ones to study the randomness in through the thickness permeability numerically when distribution media (DM) is used in a VARTM process. However, some experimental variable such as degree of nesting was not considered when modeling heterogeneity in K_{zz} for numerical simulations. Degree of nesting is a measure of how consecutive layers of fabrics are aligned relative to each other and is one of the important factors that affects the degree of variation in through the thickness permeability[41]. Also, experimental work is necessary to validate the approach towards modeling of the pinholes within the fabric using three dimensional flow simulation.

Figure 3.1 shows an image of the bottom layer of four plies of fabric when resin reached the vent in a VARTM setting. The experimental setting is described in Figure 3.2. A distribution media (DM) was placed on the top of these four layers of woven glass fabric and a Newtonian liquid (corn syrup, simulating resin) was introduced via a line injection on the top surface in contact with DM. Resin impregnated the fabric layers from the right to the left end. Dark areas highlighted with circles indicate voids and unsaturated tows. These are defects which lower the mechanical performance of the composite part. [81,83,84]. They are non-uniform and unsymmetrical, which strongly suggests stochastically varying material properties. When the inlet gate opened, resin raced through the distribution media first and then through the fabric layers in the through the thickness direction as schematically shown in Figure 3.2. In the through the thickness direction, there are two possible passages for resin to travel as shown in Figure 3.3: the first passage is through meso-scale pores (pinholes) between tows, the

second passage is through micro scale pores (tows). Resin prefers to go through the pinholes first because of its higher permeability compared to the one of the micro scale pores within a fiber tow. As can be seen in Figure 3.3, the size of pinholes vary throughout the fabric and this random variation directly affects the resin flow. This study aims to study the effect of randomly distributed pinholes and the role of DM permeability on the resin flow and void formation, numerically and experimentally.

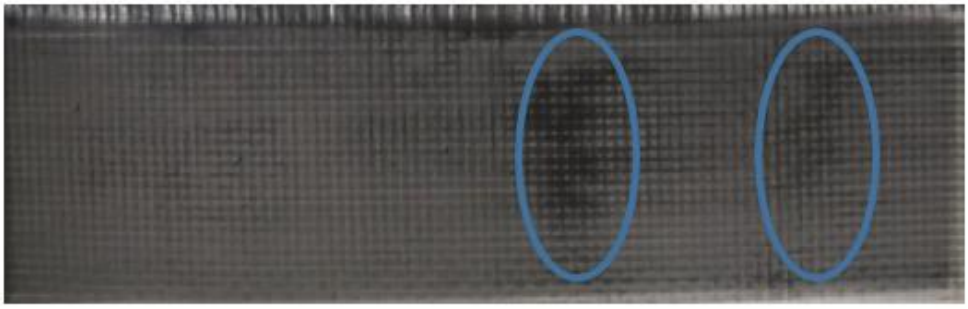

Figure 3.1 Image of the bottom layer of a fabric at the end of the VARTM experiment. The dark areas represent void regions.

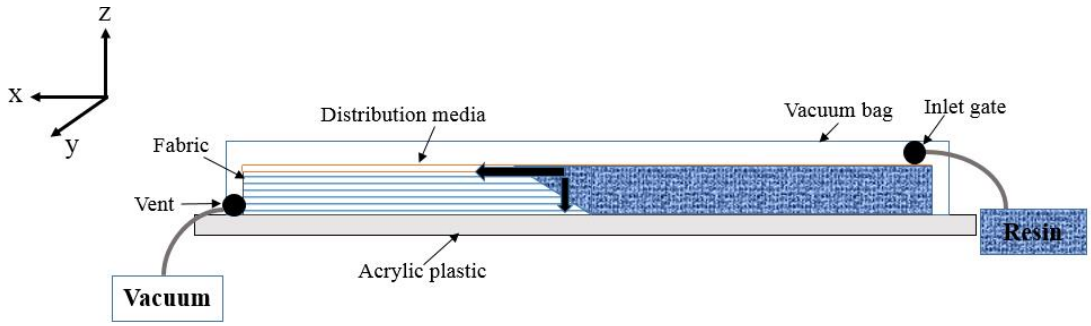

Figure 3.2 Schematic of the VARTM process to describe the impregnation of resin into the reinforcing woven fabric with distribution media placed on top of four layers of fabric.

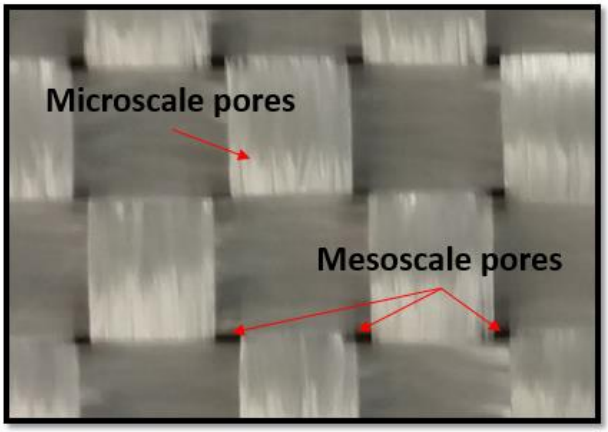

Figure 3.3 Image of a woven fabric which shows two types of pores with micro-scale pores and meso-scale pores. Note that the size of mesoscale pores vary

3.2 Characterization of the woven fabric permeability

3.2.1 Bulk permeability of the fabric

E glass fabric with an aerial density of 2.95 Kg/m^2 (shown in Figure 3.4) was used as reinforcement for our experiments. The six components of the bulk permeability of the fabric to be characterized are the in-plane permeability (K_{xx}, K_{yy}, and K_{xy}) and through the thickness permeability (K_{zz}, K_{xz}, and K_{yz}). The material symmetry dictates the principal directions of the tensor and only three components should be non-zero (K_{xx}, K_{yy}, and K_{zz}) as long as the x and y axes are aligned with the warp and weft directions. The bulk permeability components were found for a fiber volume fraction of 50% using a VARTM experiment [30]. These permeability components are listed in Table 3.1 and assumed to be uniform throughout the fabric. While all the components were determined, the non-diagonal terms are effectively zero and the principal directions are aligned with tows/through the thickness as expected. Moreover, the ratio

of K_{xx} and K_{yy} values is close to unity, which is reasonable considering how tows are woven in the same way in both the x and y directions.

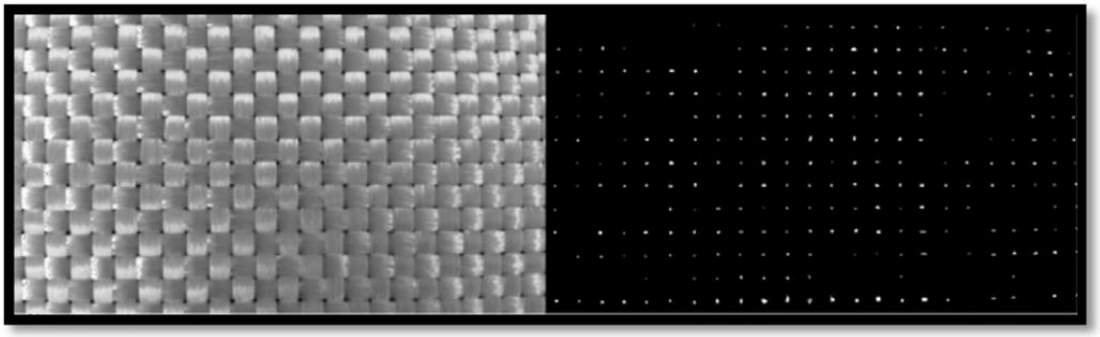

Figure 3.4 K_{pin} areas detected through image filtering tools using MATLAB. Left is the original picture (12.5 cm × 7 cm) and right is the filtered image with highlighted regions as detected pinholes between fiber tows.

Table 3.1 Permeability of a plain woven E glass fabric

$K_{xx}(m^2)$	$K_{yy}(m^2)$	$K_{zz}(m^2)$	$K_{xy}(m^2)$	$K_{xz}(m^2)$	$K_{yz}(m^2)$
8.86×10^{-11}	9.10×10^{-11}	1.36×10^{-12}	9.89×10^{-16}	1.58×10^{-15}	1.00×10^{-15}

The continuum model is somewhat inadequate as the transverse flow in this study is dominated by the pinholes. To address this inadequacy, the continuum model was altered to include enhancement in the K_{zz} permeability by flow through discrete channels, as shown in Figure 3.5. The pinholes exhibit randomly distributed permeability (K_{pin}) as can be seen from Figure 3.4.

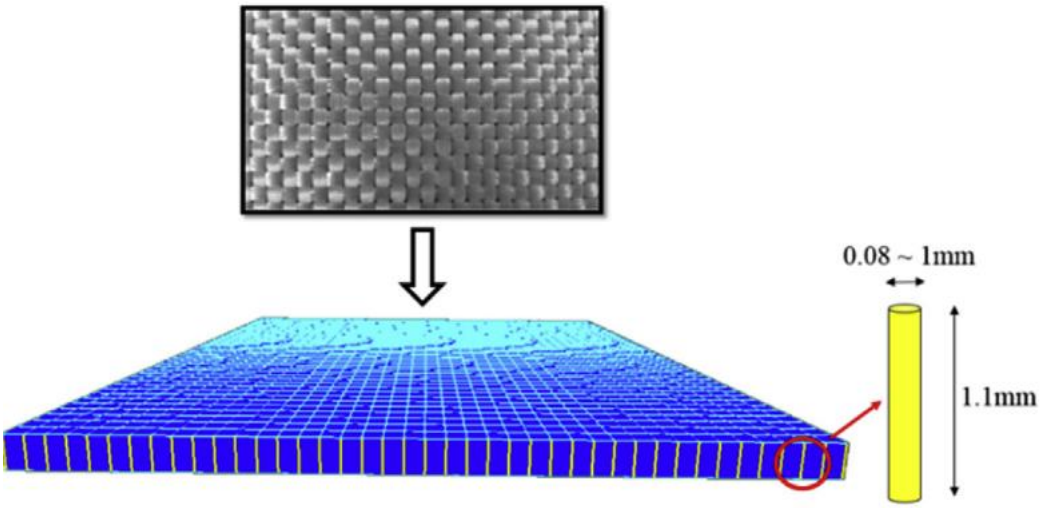

Figure 3.5 Woven fabric layer modeled as 3D elements (blue-representing micro pores of tows) and pinholes as 1D elements (yellow-representing meso pores) in the flow simulation, LIMS.

3.2.2 Pinhole permeability (K_{pin})

The flow resistance of a hole of given dimensions has been studied in some detail [85], albeit with impermeable rather than porous boundary, and mapped to the hole dimensions. The permeability of pinholes was found to be well estimated by the dimension of the pinholes. The cross sectional area of the pinholes was measured by means of image analysis consisting of two steps. First, dozens of pictures were taken of a 2 m^2 piece of fabric. The pictures were then imported to MATLAB and filtered with a suitable threshold value to produce images which contained only pinholes against a blank background. An example of a processed image is shown in Figure 3.4. The areas of the pinholes were then calculated using the filtered image. The areas were later used as an input to calculate K_{pin}. There are some regions where no pinholes are detected because tows are tightly woven so no gaps between tows are visible. For this case, a micro-scale fiber tow permeability value was assigned to the channel in the mesh shown

in Figure 3.5. The calculation of the fiber tow permeability is explained in detail in the next section.

A cylindrical shape is assumed to model the pinholes, as shown in Figure 3.5, and the pinholes are modeled as a 1D element (yellow color) adjacent to 3D element (blue color) which represents bulk glass fabric for the numerical simulation. This assumption allows one to calculate permeability of a pinhole as permeability of a cylindrical tube as follows (Equation 3.1):

$$K_{pin} = C\frac{R^2}{8} \tag{3.1}$$

Where R is radius of the pinhole and C is a correction factor (hydraulic radius) which accounts for the porous walls and non-circular geometry of the pinhole [85]. To find the correction factor, VARTM experiments were conducted with DM on top of the fabric and the lead length (the difference between the location of the flow front along the top surface and the location along the bottom surface) was recorded at all times. A value of 0.9 for the correction factor C provided a good match between the lead lengths obtained from the numerical simulation and the experiments. The K_{pin} realization obtained using this methodology is presented in Figure 3.6 which shows the heterogeneity of K_{pin} throughout the fabric. The total sample size used for the image analysis and the mean and standard deviation of K_{pin} are given in Table 3.2. The study of spatial correlation of pinholes will be discussed in the next chapter. The spatial correlation of K_{pin} is conserved in numerical simulations as the K_{pin} required for a x b domain (0.12cm x 0.53cm) is found from randomly chosen *a* x *b* domain from a very large section of the fiber preform (2 m^2).

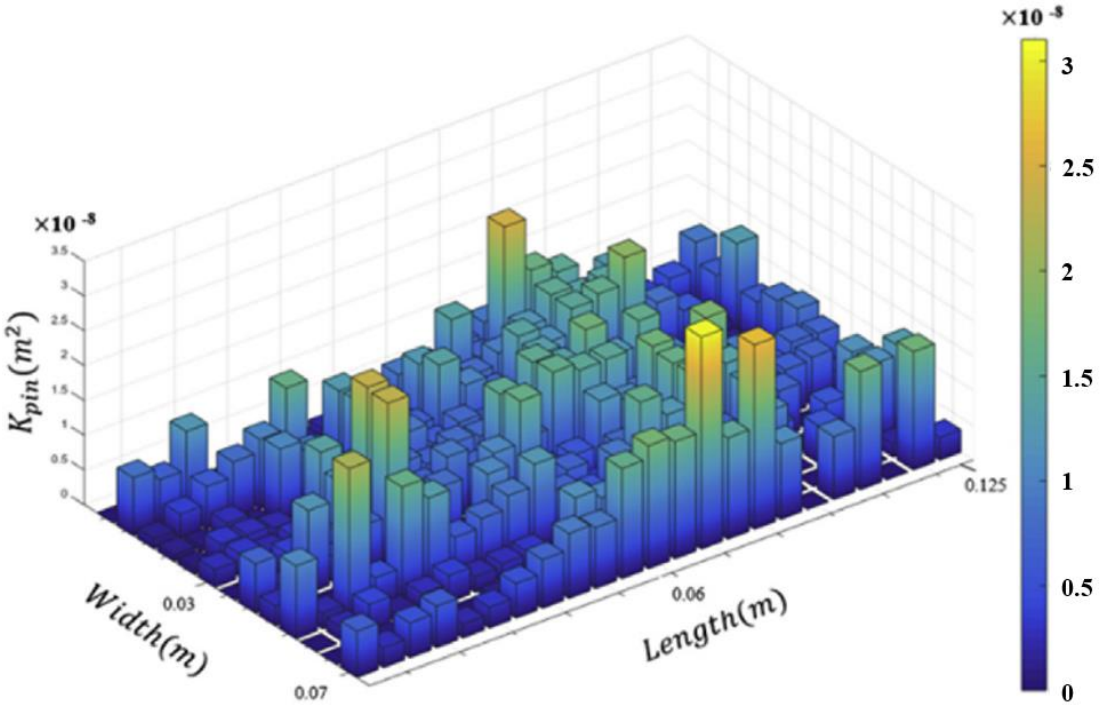

Figure 3.6 Calculated pinhole permeability values for the fabric area of 7 cm × 12.5 cm section shown in Figure 3.3.

Table 3.2 Mean and standard deviation of calculated K_{pin} from Image Analysis on Fabric

$Fabric\ Area$ (m^2) to measure K_{pin}	1.936
K_{pin} Mean(m^2)	9.7 x10^{-9}
K_{pin} Standard deviation (m^2)	9.4x10^{-9}

3.2.3 Micro scale fiber tow through the thickness permeability ($K_{zz,mic}$)

If no pinhole exists at any of the intersections, then the resin has to flow through the fiber tows (micro pores). The flow through the fiber tow is governed by micro scale

fiber tow permeability, $K_{zz,mic}$. This can be described, for example, with the equation developed by Bruschke and Advani et al. [86] that describes the flow of a Newtonian fluid across an array of cylinders as shown below.

$$\frac{K_{zz,mic}}{r^2} = \frac{\frac{1}{3}((1-L^2)^2)}{L^3}\left(\frac{3Ltan^{-1}\left(\sqrt{\frac{1+L}{1-L}}\right)}{\sqrt{1-L^2}} + \frac{L^2}{2} + 1\right)^{-1} \tag{3.2}$$

Where r is the radius of a single glass fiber, and L is a non-dimensional parameter. ($L^2 = 4V_f/\pi$, here V_f is assumed to be 0.75 for a fiber tow hence L is equal to 0.97). The radius of a glass fiber was measured and used as a value for r in the calculation of Equation 3.2. The image of cross sectional areas of fibers and a histogram of fiber diameters are both shown in Figure 3.7. The average diameter was found to be 9.2μm. $K_{zz,mic}$ is calculated to be 4.1×10^{-16} m^2. This permeability value is assigned to the K_{zz} component of the 3D element (glass fabric) in Figure 3.5 and also used as K_{pin} for 1D elements where no pinholes are detected.

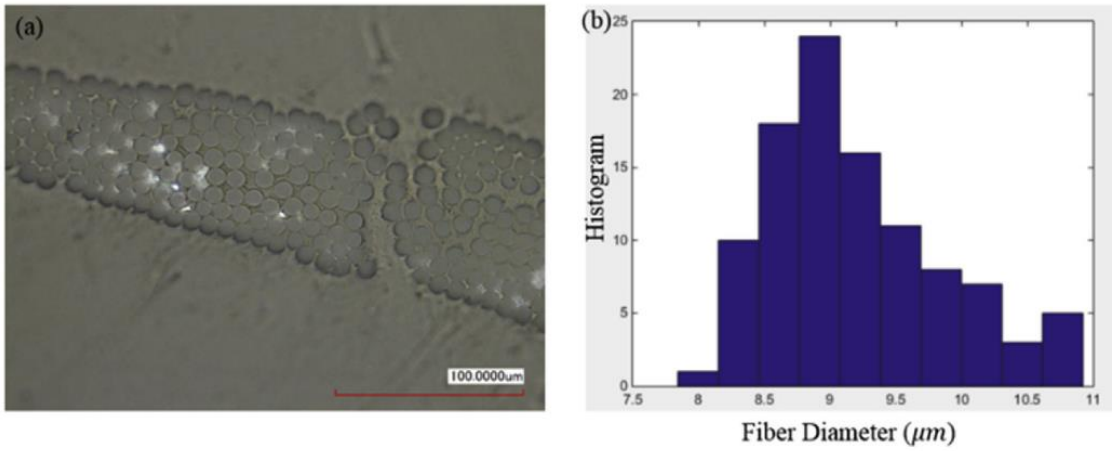

Figure 3.7 Microscope image of cross sectional area of tows (a) and histogram of fiber diameter (b) measured from the micrograph.

3.2.4 Degree of nesting between fabric layers

For a single layer of reinforcement, the model represents the fiber tows and pinhole permeability as calculated and depicted in Figure 3.4. It respects the structure's repetition in-plane which makes the continuum model suitable in this direction while allowing for discrete pathways through the thickness where no averaging takes place. The preform used in this study is, however, a multi-layered structure. For example, there are four layers in this study. There are too few layers to assume that the system behaves as a continuum in the thickness direction. Thus, it calls for a repetition of a single layer model structure, four times in our case. The question is how do the pinhole patterns in individual layers align? The misalignment is caused due to two reasons. First, if the adjacent fabric layers are not aligned with each other, the slight rotation of the pinhole arrays will result in some form of offset of the pinholes from one layer to the next. Second, the pinholes in two adjacent layers tend to be offset relative to each other to allow maximal possible nesting as can be seen in Figure 3.8 (a). In this case the

offsets are repetitive. With hand layup, there may be significant variability both from ply to ply and from part to part.

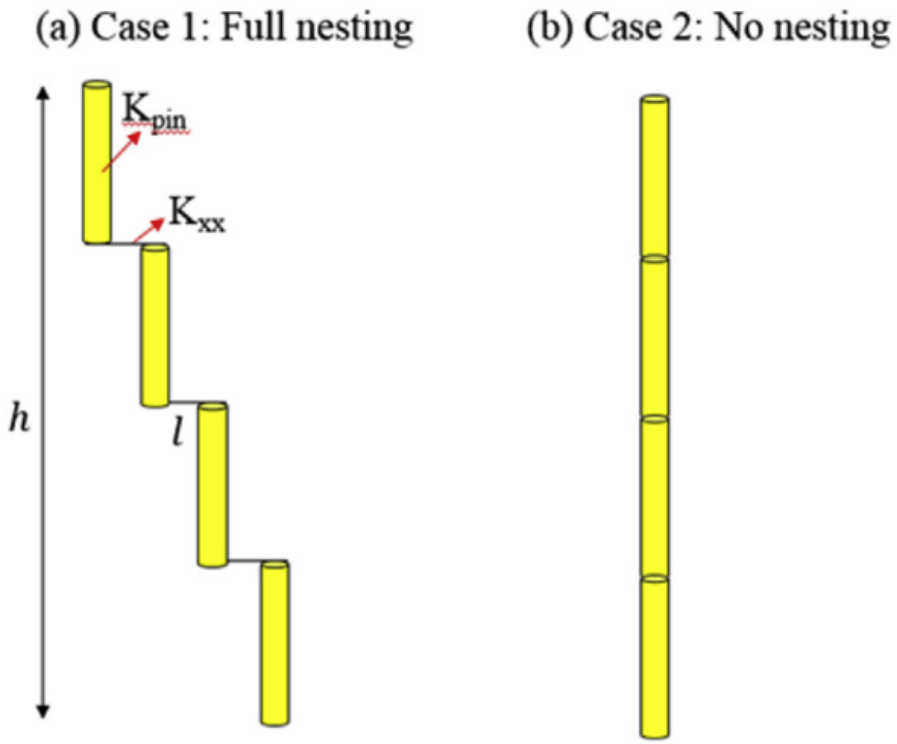

Figure 3.8 Schematic of the alignment of pinholes (a) The full nesting case and (b) The non-nesting case.

The full alignment (no nesting) and offset by a half pinhole spacing (full nesting) as shown in Figure 3.8 are the two limiting cases. Intuitively, the former is very unlikely but the latter is quite possible as the nesting between layers tends to be maximal at this configuration. We will examine these two cases by comparing globally measured through the thickness permeability with through the thickness permeability calculated by a combination of pinhole permeability and the permeability of aligned fiber beds using the rule of mixtures.

(a) Case 1 : Fully nested

Pinholes and fabrics are connected in series from top to bottom. Thus, the effective permeability can be calculated using Equation. 3.4.

$$\frac{h+3l}{K_{pin,eff}} = 3\left(\frac{l}{K_{xx}}\right) + \sum_{k=1}^{4}\left(\frac{h}{4K_{pin,k}}\right) \tag{3.4}$$

Where h is the total height of the alignment, $K_{pin,k}$ is permeability of kth pin hole, and l is the distance between two pin holes.

The first term on the left side in Equation 3.4 accounts for $K_{pin,eff}$ over the distance of h + 3l. on the right side, first term accounts for resin traveling the K_{xx} direction over the distance of l. The second term on the right side is for resin to travel only through pinholes over 4 layers.

The term with $K_{pin,k}$ on the right side is negligible because K_{pin} (2×10^{-10}~3×10^{-08}m^2, mean 9.73×10^{-09}m^2) is two orders of magnitude higher than K_{xx} (8.86×10^{-11}m^2). l is 0.25cm and h is 2.8mm. $K_{pin,eff}$ is calculated to be 2.1×10^{-10}m^2.

(b) Case 2 : Not nested

Four pin holes are connected in series as shown in Figure 3.8 (b). The pin holes in series are also connected in parallel throughout the fabric. There are total 30×104 (3120) sets of pin holes in series for $0.15m \times 0.30m$ fabric. The permeability for the series model can be expressed as shown in Equation 3.5. Once the individual series model permeability (K_s) is calculated, effective pin hole permeability ($K_{pin,eff}$) can be finally obtained by calculating K_s in parallel model using Equation 3.6. Equation 3.5 is

calculation of K_s in series. Equation 3.6 shows calculation of $K_{pin,eff}$ in a parallel connection.

$$\frac{h}{K_s} = \sum_{k=1}^{4} \left(\frac{h}{4K_{k,s}} \right) \tag{3.5}$$

$$K_{pin,eff} = \left(\frac{1}{A_{k,tot}} \right) \sum_{k=1}^{3120} A_k K_{k,s} \tag{3.6}$$

Where $A_{k,tot}$ is total area of fabric ($0.15m \times 0.30m$), A_k is a surface area of kth pin hole, and $K_{k,s}$ is kth series model permeability. $K_{pin,eff}$ is calculated to be 1.5×10^{-08}m^2.

$K_{pin,eff}$ in the fully nested case is two order of magnitude higher than the one in the non-nested case. This is a reasonable result because only bulk in-plane permeability (9×10^{-11}m^2) determines the effective permeability value in the fully nested case. On the other hand, K_{pin} (mean 9×10^{-09}m^2) is only factor that determines $K_{pin,eff}$.

When the obtained values of $K_{pin,eff}$ from two cases are introduced to Equation 3.7, K_{zz} can be calculated. And this K_{zz} is compared to the experimentally determined one ($1.3\times 10^{-12}m^2$)

$$K_{zz} = \left(1 - A_{fpin}\right) K_{zz,mic} + A_{fpin} K_{pin,eff} \tag{3.7}$$

Where A_{fpin} is the fraction of the area of the pinholes to the total area of the fabric, $K_{pin,eff}$ is effective permeability that averages individual K_{pin} values, $K_{zz,mic}$ is the micro scale through the thickness permeability, and K_{zz} is the bulk through the thickness

permeability measured experimentally in a VARTM setting. A_{fpin} is found to be 0.03. $K_{pin,eff}$ is largely affected by the degree of nesting when multiple layers (4 plies in this case) of fabrics are used for the VARTM test. $K_{pin,eff}$ is determined for the two cases mentioned above, fully nesting and non-nesting.

When K_{zz} is calculated for the fully nesting and non-nesting cases with different values for $K_{pin,eff}$, the K_{zz} values are 5.25×10^{-12}m^2 for the fully nested case and 3.4×10^{-10} m^2 for the non-nested case. The fully nested case model yields a K_{zz} which is closer to the experimentally determined K_{zz} value of 1.36x10^{-12} m^2. This confirms the heuristic observation that the pinholes are unlikely to align. The calculations for effective permeability suggest that to match the experimental through the thickness permeability, the degree of nesting is high, otherwise the measured permeability would be much higher. Thus, we include full nesting (overlap of half the pinhole spacing, Figure 3.8 (a)) in the model.

3.3 Experimental Result

3.3.1 Experimental setting

The schematic and a photograph of the experimental setting are presented in Figure 3.9. The schematic is presented in Figure 3.9 (a), and the photograph of the setting is given in Figure 3.9 (b). A VARTM experiment was carried out in a dark room with diffusive light above the fabrics and DM to enhance the visibility of tow saturation and voids being formed as resin impregnates the reinforcement. The camera was mounted below the acrylic mold to record the resin flow as shown in the schematic in Figure 3.9. Previously characterized E-glass fabric was used as the reinforcement

sample. The width of the sample is 0.12m and length is 0.53m. Corn syrup was used as the simulated resin at room temperature. The viscosity of the liquid was measured and the fabrics were weighed to calculate the volume fraction before each test. The experimental procedure is described below:

Four plies of fabrics were placed on the acrylic plastic table. Distribution media of width 0.11m and length 0.48m was placed on top of the plies. A spiral plastic tube served as the injection line and was placed on the right end and the vacuum line was placed on the left of the layers of fabric as shown in Figure 3.9. The width of DM was slightly narrower than that of the fabric to avoid race tracking during the infusion process. Lastly, the mold was sealed by adhering a vacuum bag on top of the assembly with a sealing tape. After the vacuum seal was secured, full vacuum inside the bag was drawn introducing the simulated resin under atmospheric pressure into the mold. The resin first entered the DM through the inlet gate and then infused into the fabric layers. The inlet gate was closed when the resin reached the vent which was about 2.54cm passed the end of DM.

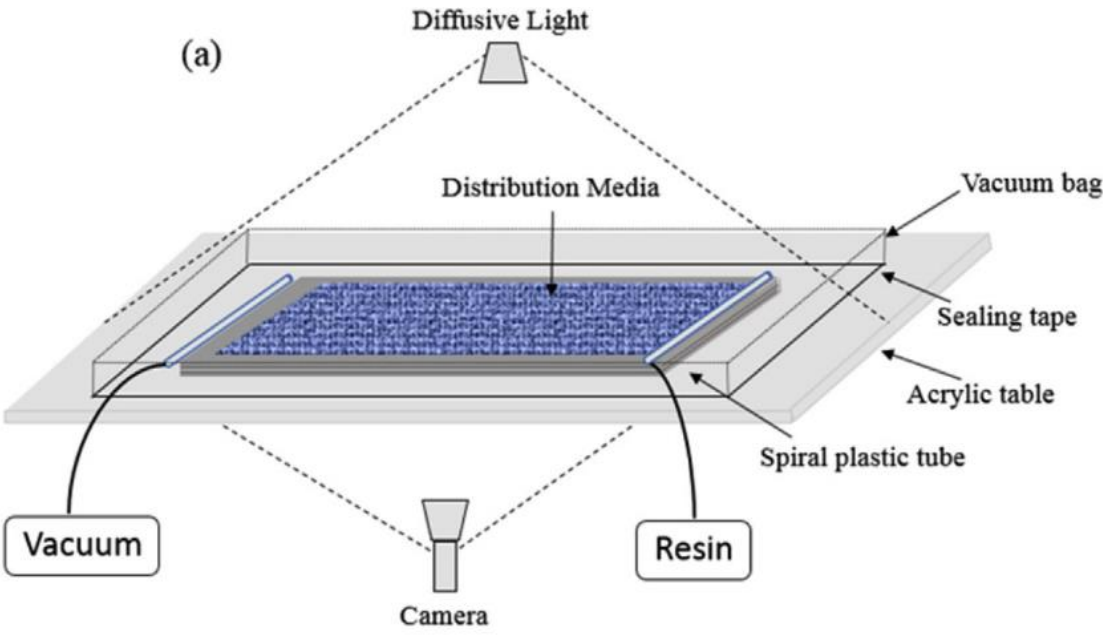

(b)

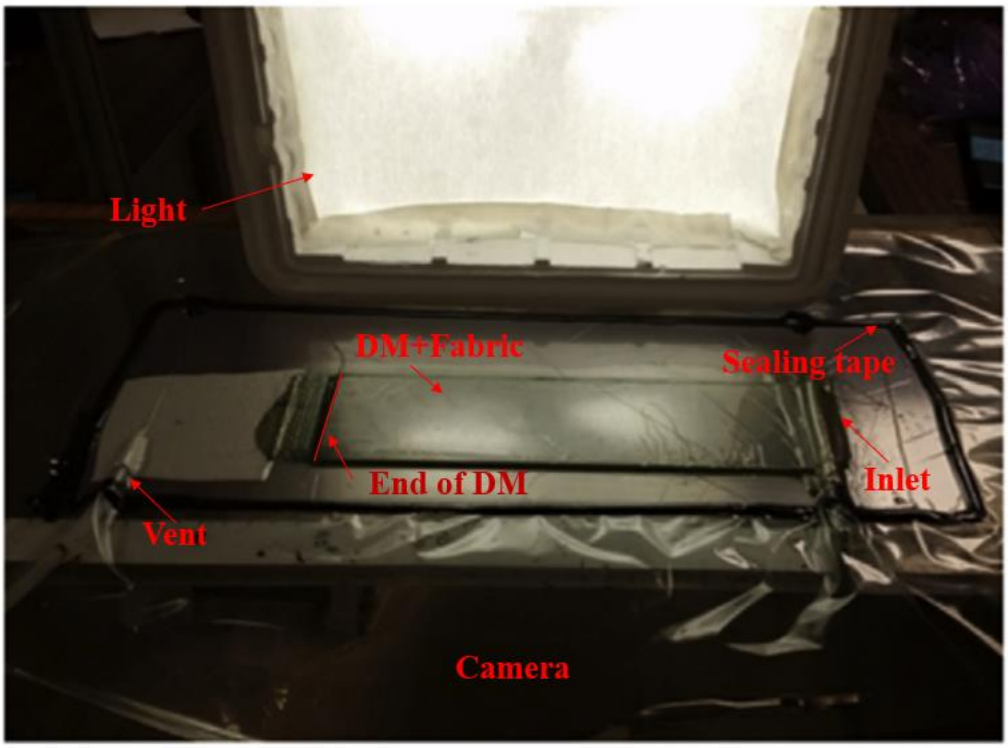

Figure 3.9 (a) Schematic and (b) Image of a VARTM experiment setting.

An image of the bottom layer at the end of each experiment was used to calculate void percentage using MATLAB imaging tools. The images are presented in Figure 3.10. As can be seen in Figure 3.10, the original image in (a) is filtered with a suitable threshold to produce the processed image in (b). The area of black regions in the filtered image represents the void region, which is the unsaturated area. The void percentage is calculated as a fraction of the area of black region over the total area (0.48 x0.12 m). The thickness of dry spots, which is required to calculate the void percentage, was assumed to be the thickness of the bottom layer of fabric. In this study, only voids at the bottom layer are considered. This is a good approximation of total void content because numerical simulation shows that the majority of voids (>90%) are found in the bottom layer.

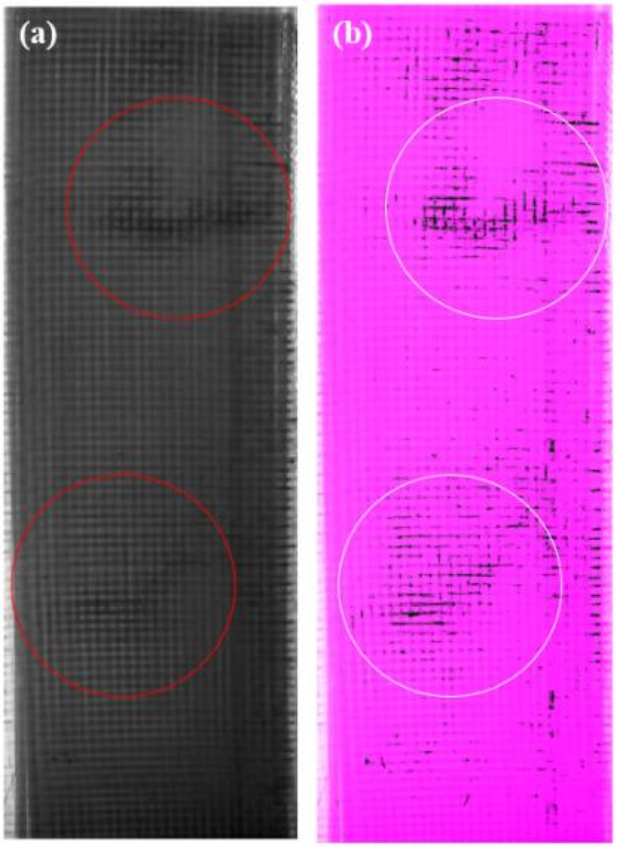

Figure 3.10 Image of the bottom layer with DM of K_{DM}= 1.45e-8m^2 when resin reaches 2.54cm past the end of DM. (a) original image (b) image filtered and combined with original image highlighting the unfilled regions (voids)

3.3.2 Experimental results: Flow front data

A total of 60 experiments (20 experiments for each DM permeability value K_{DM} of 4x10^{-09}m^2, 8.5x10^{-09}m^2 and 1.45x10^{-08}m^2, respectively) were conducted and representative images of the flow fronts are presented in Figure 3.11. This figure shows the flow fronts at the bottom when resin reached 30cm from the inlet gate for no DM used (a), and with the three other cases of increasing K_{DM} (b-d). The first thing to notice is that, as expected, a longer lead length is observed as the K_{DM} value increases. The lead length is zero with no DM, 2.43cm with K_{DM} of 4x10^{-09} m^2, 9.9cm with K_{DM} of

$8.5x10^{-09}$ m^2, and 16cm with K_{DM} of $1.45x10^{-08}$ m^2. This means that with increasing K_{DM}, there is more available resin in the distribution media to race through pinholes to reach the bottom. That is, more resin travels in the through the thickness direction where the stochastic pinholes exist. The second observation is that the flow front becomes more wavy and spotty with increasing K_{DM} which eventually led to a higher percentage of voids or unsaturated tows. Wavy and spotty flow fronts are more likely to enclose air pockets. For the higher DM permeability in (c) and (d) in Figure 3.11, we can see the discontinuous resin spots appearing ahead of the continuous flow front.

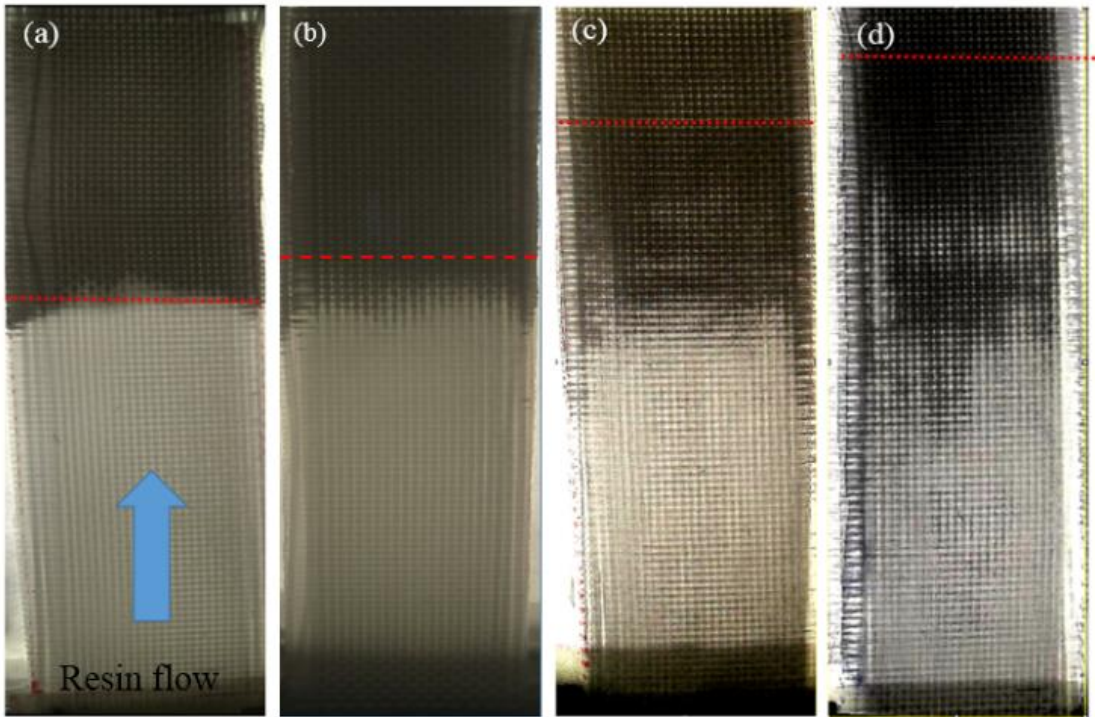

Figure 3.11 Experimental image of the bottom layer when the flow front reached 30cm from the inlet gate with (a) No DM (b) K_{DM}= 4e-09 m^2 (c) K_{DM}= 8.5e-09 m^2 (d) K_{DM}= 1.45e-08 m^2 in a VARTM process. Red dotted line represents the position of flow front along the top surface

3.4 Numerical simulation results: Flow fronts

Numerical simulations were carried out using the Liquid Injection Molding Simulation (LIMS) model, developed at the University of Delaware [77] (See appendix A for more details). A panel of four layers (0.12m x 0.53m) of fully nested fabrics (with thickness of 0.44 cm) and a ply of distribution media (0.11m x 0.48m) of constant thickness of 0.1cm are simulated using 3D (representing the glass fabric), 2D (representing the distribution media) and 1D (representing the pinholes) elements respectively. The experimentally determined bulk permeability is presented in Table 3.1. This bulk permeability except for K_{zz} was assigned as permeability of 3D elements. Fiber tow permeability obtained using Equation 3.2 was used for K_{zz} ($4.1x10^{-16}m^2$). Three types of DM with permeability of $1.45x10^{-08}m^2$, $8.5x10^{-9}m^2$ and $4x10^{-09}m^2$ were used for this study. These DM permeability were determined experimentally through 1D flow experiment in a VARTM process. A mesh refinement study was carried out to ensure convergence. It was found that the difference of resin arrival time at each node between the current mesh (element size : 43272) and twice refined mesh was within 1%. The test conditions, such as volume fraction, inlet pressure, and viscosity that were used for this simulation study are given in Table 3.3.

Table 3.3 Experimental condition used for the numerical simulation study

Fabric volume fraction	0.5
Pressure (Pa)	$1 x10^5$
Viscosity (Pa.s)	0.1

A total of 500 simulations with random combinations of pinholes were carried out for each DM case (permeability of $1.45x10^{-08}m^2$, $8.5x10^{-09}m^2$ and $4x10^{-09}m^2$). The

pinhole distribution for each layer of the four layers of fabrics was obtained by randomly choosing an area of 0.12m x 0.53m out of the total sample of $2m^2$ containing measured pinhole locations and diameters, which preserves the spatial correlation between the adjacent pinholes. Each layer was randomly positioned into the four layer stacks for the numerical simulation.

The shape of the flow front at the bottom fabric as resin impregnates the fabric is a key feature recorded during the simulation of the VARTM experimental conditions. The shape of the flow front along the bottom layer distinctively changed with varying magnitude of DM permeability. Figure 3.12 presents simulation results of the flow fronts at different times in the bottom layer for the four cases modeled: no distribution media and three varying distribution media permeability (permeability of $1.45x10^{-08}m^2$, $8.5x10^{-09}m^2$, $4x10^{-09}m^2$). Flow fronts at the bottom when no DM is used are uniform as seen in Figure 3.12 (a). As K_{DM} value increases, the flow front at different times becomes progressively and distinctively wavy and spotty as shown in Figure 3.12 (b) to (d). The spotting and wavy appearance of resin at the bottom is due to the resin racing through the permeable distribution media at the top and making its way to the bottom through easy pathways (pinholes) to reach the bottom ahead of the resin front as also noted by Markicievic [43] and corroborated by our experimental results.

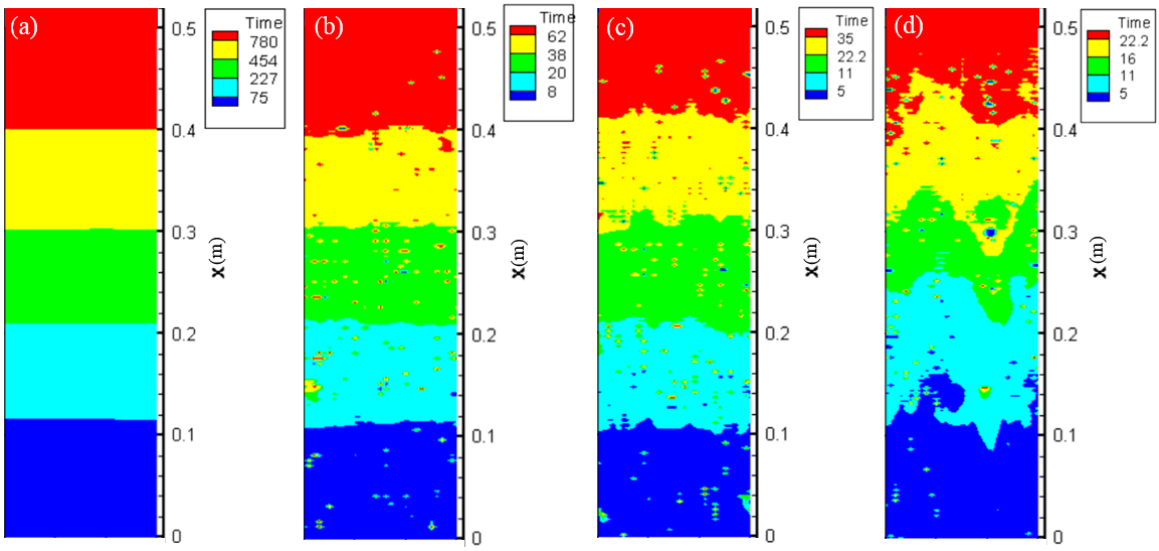

Figure 3.12 Simulation images of the bottom layer showing flow front patterns at different times with (a) No DM (b) K_{DM}= 4e-09 m^2 (c) K_{DM}= 8.5e-09 m^2 (d) K_{DM}= 1.45e-08 m^2 in a VARTM process. Time is in second.

3.5 Comparison between experimental and numerical results: Percentage of voids

The non-uniformity in flow front pattern at the bottom is not straightforward to quantify. However, the separation of voids behind the flow front and the size of these voids can be characterized as described in the experimental section. We will represent it as a fraction of bottom surface that remains dry behind the flow front. Void percentage in the bottom is calculated using the image filtering analysis and is presented in Figure 3.13. Both experimental and numerical results show a clear trend of faster flow advancement and increasing percentage of void with higher DM permeability. Although there is some visible discrepancy between numerical model and experimental values, they still match reasonably well qualitatively and quantitatively. From the numerical simulations, void percentage ranges from 0.19~4.71% when K_{DM} is $4x10^{-09}m^2$, 0.73~6.05% with a K_{DM} of $8.5x10^{-09}m^2$, and 1.06~6.81% with a K_{DM} of $1.45x10^{-09}m^2$.

Experimental results show that void percentage ranges from $5x10^{-4}$~3.33% when K_{DM} is $4x10^{-09}m^2$, 0.19~5.21% with a K_{DM} of $8.5x10^{-9}m^2$ and 1.00~8.45% with a K_{DM} of $1.45x10^{-8}m^2$. The results from experiments and simulations are displayed in Table 3.4. Note that the range for the experimental values is obtained from 20 experiments whereas the range for the simulations is from 500 different runs for each type of DM.

(a) Experimental

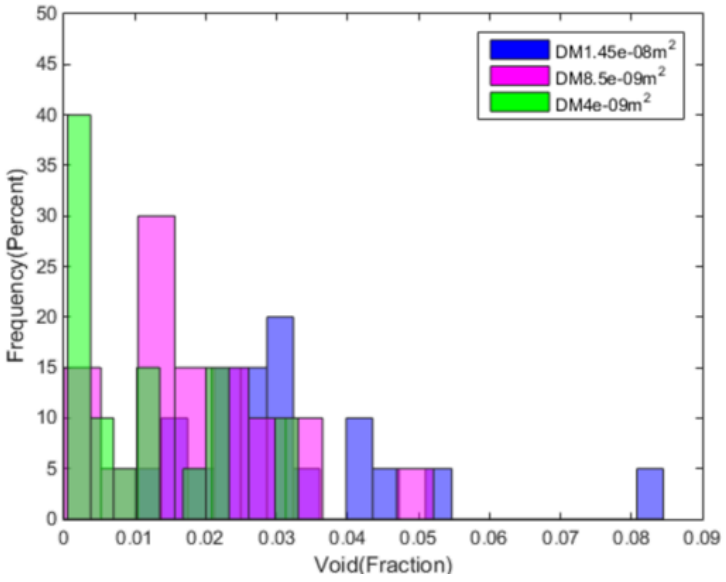

(b) Simulation

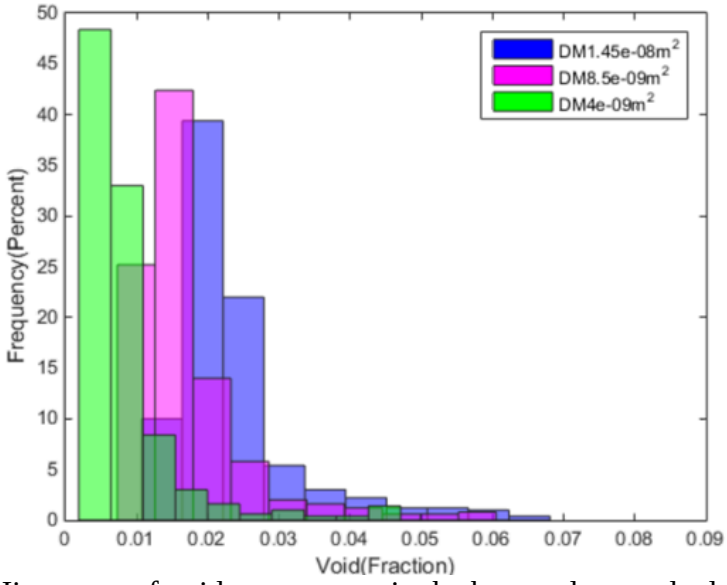

Figure 3.13 Histogram of void percentages in the bottom layer calculated from both experimental (a) and simulation (b) study. Different color represents different K_DM magnitude.

Table 3.4 Void percentage obtained from experimental and simulation work

	Experimental study			Simulation study		
$K_{DM}(m^2)$	Void (%)	Mean	Standard Deviation	Void (%)	Mean	Standard Deviation
$1.45x10^{-8}$	1.00~8.45	3.15	1.63	1.06~6.81	2.33	0.91
$8.5x10^{-9}$	0.19~5.21	1.59	0.77	0.73~6.05	1.72	0.82
$4x10^{-9}$	$5x10^{-4}$~3.33	1.09	1.00	0.19~4.71	0.85	0.71

Note that the porosity detected at the particular stage of filling is not the same as final porosity, as resin is allowed to bleed out of the vent in an attempt to further reduce the void content. Description of this part of the process is not addressed in this thesis.

3.6 Summary and Conclusions

Monte Carlo method was used to successfully characterize the pinhole through the thickness permeability (K_{pin}) and introduce it as input to conduct 3D numerical simulations of resin flow during the SCRIMP process. Its influence on resin flow patterns and void formation were investigated. A flow model with pinholes was created to simulate the flow through layered materials that exhibit an in-plane characteristic of continuum but discrete flow pathways (pinholes) in through the thickness direction. The realistic degree of nesting for multilayered reinforcements was estimated and the fully nested case was chosen to represent the experimental conditions.

The numerical simulation results based on experimentally determined pinhole data captured the important characteristics of resin flow, such as spotting and wavy flow fronts, which qualitatively compares well with recorded experimental flow fronts. This study clearly shows that higher the value of K_{DM}, higher will be the void percentage in both the observed and modeled cases. The void fractions found in experimental and numerical results agreed quantitatively within ~20%.

The necessity to constrain flow velocity to reduce voids has been observed numerous times. One study attributed it to the competition between capillary action in fiber tows and pressure driven advancement in larger channels but not for the VARTM process or with the presence of DM [87]. The current research in the presence of DM suggests a different (or additional) explanation for this phenomenon is needed, such as percentage of voids, and also highlights the stochastic nature of these voids. Therefore, the effect of the distribution and stochastic nature of the pinholes for woven and stitched fabrics on void formation should be studied to design a robust process with an optimum window of K_{DM} which results in low void percentage and a reasonable manufacturing time.

The K_{pin} random fields obtained from the image analysis and used for numerical simulations are not yet characterized statistically within a mathematical framework. With a formal approach the random fields can be generated instead of being obtained through time-consuming image analysis once these statistical properties of spatial correlations or a distribution function are identified. The next chapter introduces the statistical characterization of such random fields which can then be used as an input to the numerical simulations.

Chapter 4

RANDOM FIELD GENERATION OF STOCHASTICALLY VARYING THROUGH THE THICKNESS PERMEABILITY

4.1 Introduction

Most composite parts are long and wide but only a few millimeters in thickness. In previous studies [28,45,47,49,50,52,63,64,88,89], it was found that variability in permeability exists in both the in-plane and through the thickness directions. There are many reasons for this variability such as handling, placement, and variations in fabric and the VARTM manufacturing process. The variability in permeability causes random resin flow variations through the fabric during the impregnation process. The effect of variability in though the thickness permebailty, which is due to the pinhole regions is well presented in Chapter 3. An example of the fabric with pinholes is shown in Figure 4.1. These pinholes vary in size throughout the fabric, hence their K_{pin} values which is the K_{zz} value at that location will be different as well. It is also notable that there are areas with pinholes (*pinhole areas*) and areas without pinholes (*no pinhole areas*), which are demonstrated through an image analysis in Figure 4.1 (b). This variation causes the resin to race preferentially through different pathways with varying K_{pin} in through the thickness direction, and this variation leads to uneven resin flow causing formation of air pockets due to the merging of the flow fronts which result in voids. It was also found by experimental and numerical studies that more voids were formed when DM with higher permeability was used, because the higher permeability DM increases resin flow in through the thickness direction through the pinholes [88].

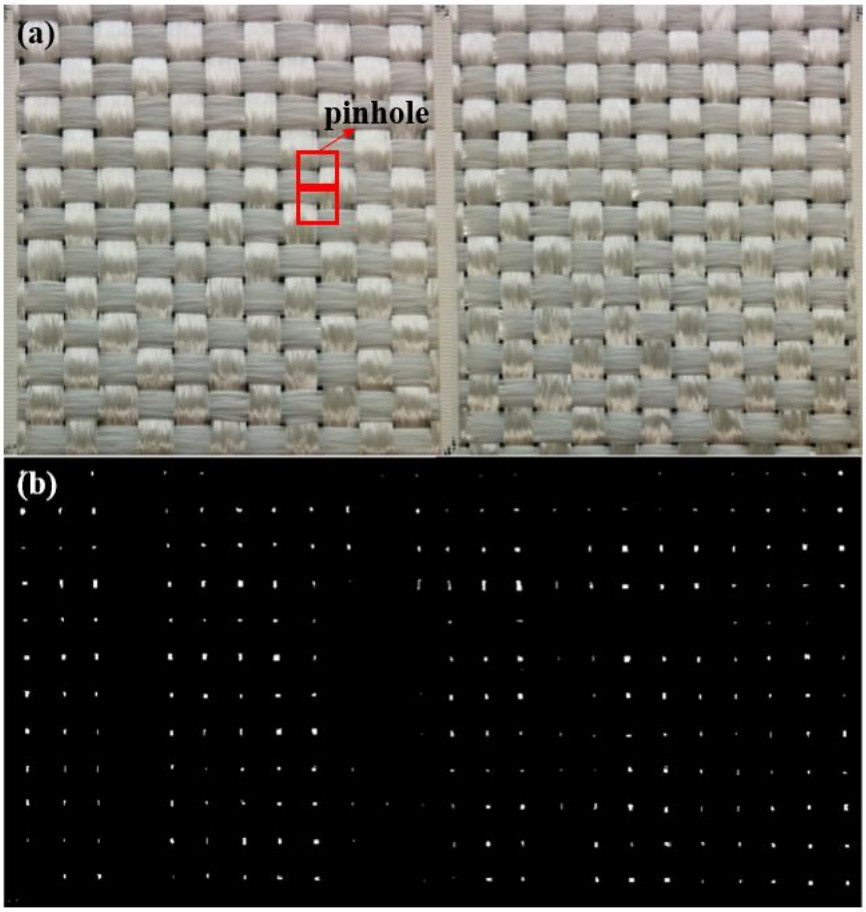

Figure 4.1 Image of E-glass fabric (120mm by 60mm) (a) and filtered image using image analysis (b)

Although the effect of K_{pin} on resin flow and void formation was well studied using experimental and numerical work in the previous chapter, a formal framework of the statistical analysis of the heterogeneous K_{pin} field was not conducted. To obtain random fields of K_{pin} for use in numerical simulations, a number of images of a large sample must be taken. Obtaining the K_{pin} values for large section of fabrics for composite parts such as a wind turbine blade can be time consuming and may not be

feasible. Thus, the statistical study of the random K_{pin} field is important for (a) understanding the degree of heterogeneity and (b) so to generate the random K_{pin} field using statistical variations in a fabric without the time-consuming step of acquiring many images of a large fabric sample. The statistically generated random K_{pin} field can then be incorporated into a numerical flow simulation which predicts the resin flow and void formation in the presence of this heterogeneity. In this section of the study, the novelty is that the pinhole field is statistically analyzed and the statistical properties found from this analysis are used to generate K_{pin} random fields. First, the heterogeneity in K_{pin} was statistically characterized by spatial correlation with Moran's *I* index and semi-variogram. Then the random field of K_{pin} was generated by transforming the normal numbers from Karhunen–Loève (KL) expansion to gamma numbers. A numerical flow simulation of the VARTM process with the generated random fields was performed using Monte Carlo method for three types of Distribution Media (DM). The effect of the heterogeneity on the resin flow was studied and compared with the previously reported experimental results.

4.2 Methodology

4.2.1 Gamma random numbers and *no pinhole area*

There are various works[90–93] published in the past which present a method to create a random field. However, most of the cases are regarding a random field of normal random numbers (Gaussian random numbers). One more important thing to note is that the random field is, regardless of discrete or continuous, filled with the random values using a random number generation which is function of not only random

Gaussian number but also coordinate (location) and is a smooth procedure without discontinuities. There are available codes online to implement this methodology (Matlab, python, and C++ etc).

However, in this specific study, the condition to carry out the process is quite different because (a) the random numbers are not normal (Gaussian) random numbers and (b) the random field space has regions which do not need to be assigned any random numbers. These regions for our case are called *no pinhole areas* and the rest of the domain is called the *pinhole area*. Hence a methodology was developed to convert non-normal numbers to normal numbers and to characterize the *no pinhole area* which is presented in the next section.

4.2.2 Methodology overview

Generating the K_{pin} random field requires several steps including image acquisition, image analysis, and statistical analysis. An algorithm illustrating the methodology used in this study to generate the K_{pin} random field is presented in Figure 4.2. First, multiple images of a fabric of interest are captured and filtered using a MATLAB image analysis tool. Then, K_{pin} are calculated using the cross-sectional area of pinholes from the image analysis[88]. Next, the mean, standard deviation, and spatial correlation (semi-variogram) of K_{pin} are calculated. To understand the spatial correlation of *pinhole areas* and *no pinhole areas*, a cluster analysis is carried out using Moran's *I* index. Moran's *I* is a widely used statistical measure of spatial autocorrelation[94]. Once Moran's *I* index of the K_{pin} samples is obtained, random fields of this index are generated, which supply the locations of the pinholes. Next step is to generate actual K_{pin} values which will be assigned to the found locations. The

probability density function (PDF) of the experimentally found K_{pin} field fits a gamma distribution, but it is difficult to directly generate gamma random numbers. Thus, the transformation between gamma and normal random numbers is used in this study. In this transformation, the covariance function of the K_{pin} gamma distribution is converted to the covariance function of a normal distribution. The result from the cluster analysis, along with the converted covariance function, is utilized to generate normal random numbers by Karhunen–Loève (KL) expansion. Finally, normal random numbers are transformed to gamma distribution numbers, which are used to generate the K_{pin} field to be used as input in the numerical flow simulation.

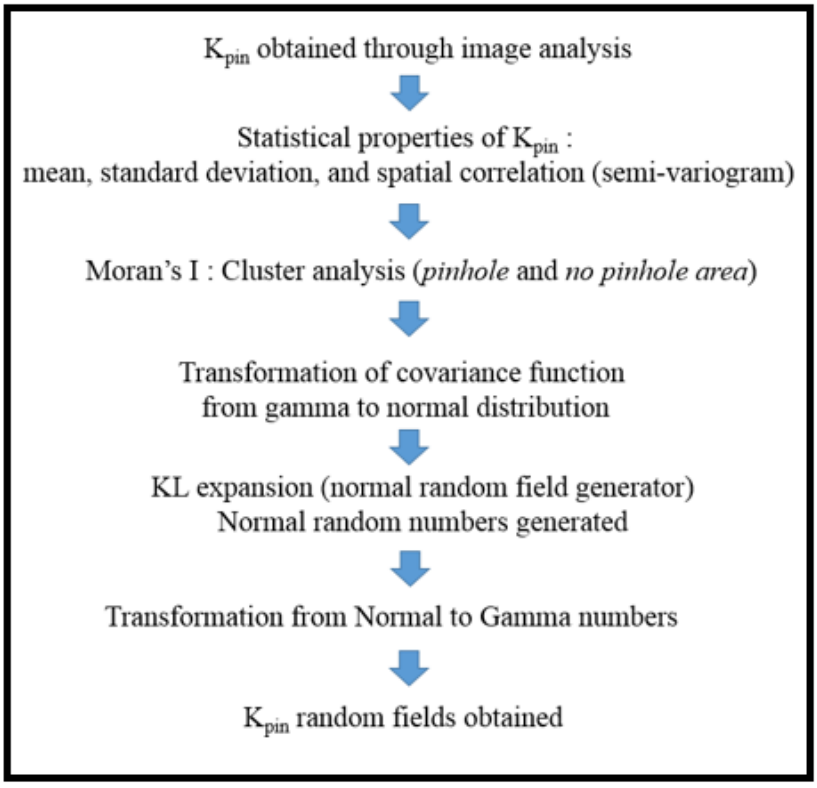

Figure 4.2 Steps for methodology to generate K_{pin} random field

4.2.3 Material and K_{pin} property

Plain woven E-glass fabric, with a volume density of 2.5g/m^3, was used as a sample in this study so one could compare it to previously obtained results. An image of the fabric is shown in Figure 4.1. The image on the top (Figure 4.1 a) is an unedited picture and the image on the bottom (Figure 4.1 b) is the image from Figure 4.1 a filtered to show only the pinholes. As can be seen in Figure 4.1 b, the pinholes vary in size throughout the fabric. The optimum number of pixels for a 5cm x 6cm image was found to be 1605 x1905 pixels. This optimum number of pixels was determined by taking images with various ranges of pixels to find the smallest number of pixels with which the size of K_{pin} does not change. K_{pin} is calculated using the measured cross-sectional area of each pinhole which is obtained from the image analysis. The detailed equation and method are presented in 3.2.2 A realization of the random field obtained using this methodology is presented in Figure 4.3, in which color signifies permeability, and Figure 4.4, in which white signifies *pinhole area* and black signifies *no pinhole area*.

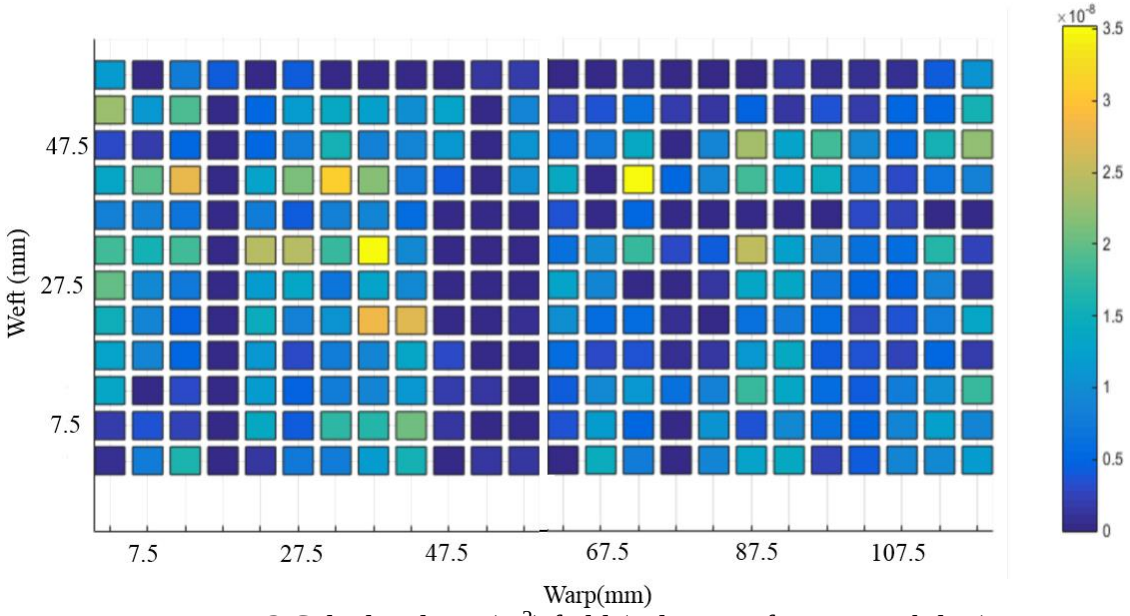

Figure 4.3 Calculated $K_{pin}(m^2)$ field (color signifies permeability)

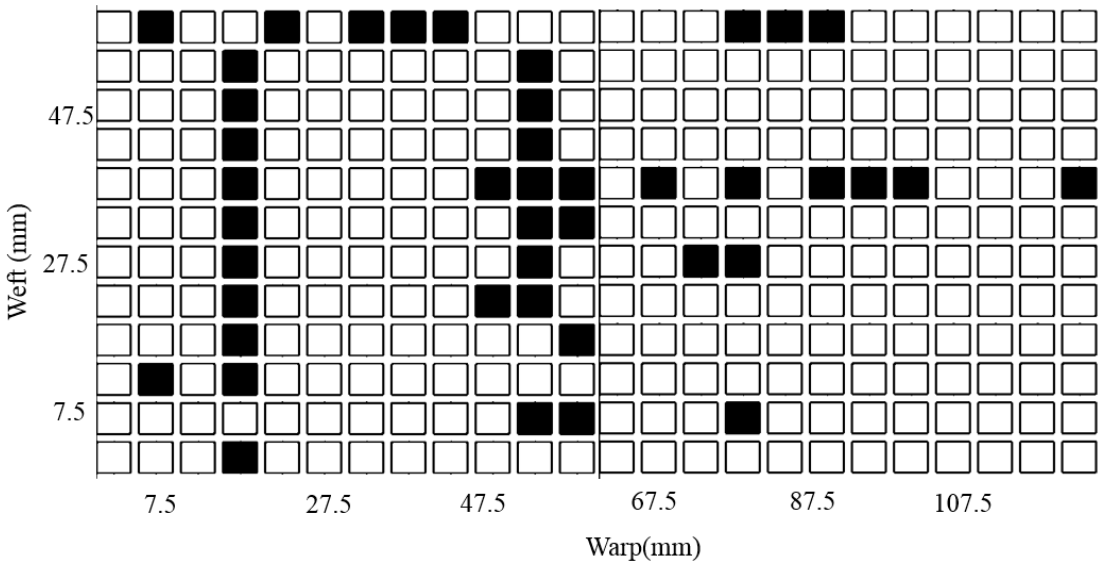

Figure 4.4 K_{pin} field with pinhole and no pinhole area. White area represents pinhole areas and black area represents no pinhole areas

As can be seen in Figure 4.4, there are areas with pinholes and areas without pinholes. Regions in K_{pin} field with *no pinhole area* are present because at the intersection of some tightly woven tows no pinhole was detected. For these *no pinhole*

areas, a permeability of $K_{zz,mic}$ ($8.2\times10^{-14}m^2$) is assigned, and this value is calculated from an analytic result of resin flow across a fiber tow[86].

$$\frac{K_{zz,mic}}{r^2} = \frac{\frac{1}{3}((1-L^2)^2)}{L^3}\left(\frac{3Ltan^{-1}\left(\sqrt{\frac{1+L}{1-L}}\right)}{\sqrt{1-L^2}} + \frac{L^2}{2} + 1\right)^{-1} \tag{4.1}$$

$$L^2 = \frac{4V_{f,tow}}{\pi} \tag{4.2}$$

$$V_{f,tow} = \frac{V_f - f_{pin}}{(1-f_{pin})} \tag{4.3}$$

In Equations 4.1-4.3, r is the radius of a single glass fiber, L is a non-dimensional parameter, $V_{f,tow}$ is a volume fraction of a tow, V_f is a measured volume fraction of 4 layers of fabric under vacuum, and f_{pin} is fraction of *pinhole areas*. $V_{f,tow}$ is calculated to be 0.66 with V_f of 0.45 and f_{pin} of 0.16 and L is found to be 0.91. Average fiber diameter was measured to be 9.2μ as can be found in 3.2.3 and Figure 3.7.

The location of *no pinhole areas* in a random field is obtained from a spatial correlation study of the two areas, *no pinhole* and *pinhole areas*, using Moran's *I* index. The PDFs of the random fields with and without $K_{zz,mic}$ (the *no pinhole* permeability) show a clear discrepancy, which is presented in Figure 4.5. The PDF without $K_{zz,mic}$ fits a gamma distribution (in Figure 4.5 bottom) and this gamma distribution is used to generate the K_{pin} values in a random field. The gamma distribution is fitted using maximum likelihood estimation (MLE). The gamma distribution fits the PDF of K_{pin} reasonably except for the range of low K_{pin} ($0\sim5\times 10^{-10}m^2$) which is acceptable because the K_{pin} effect is more prominent at higher values.

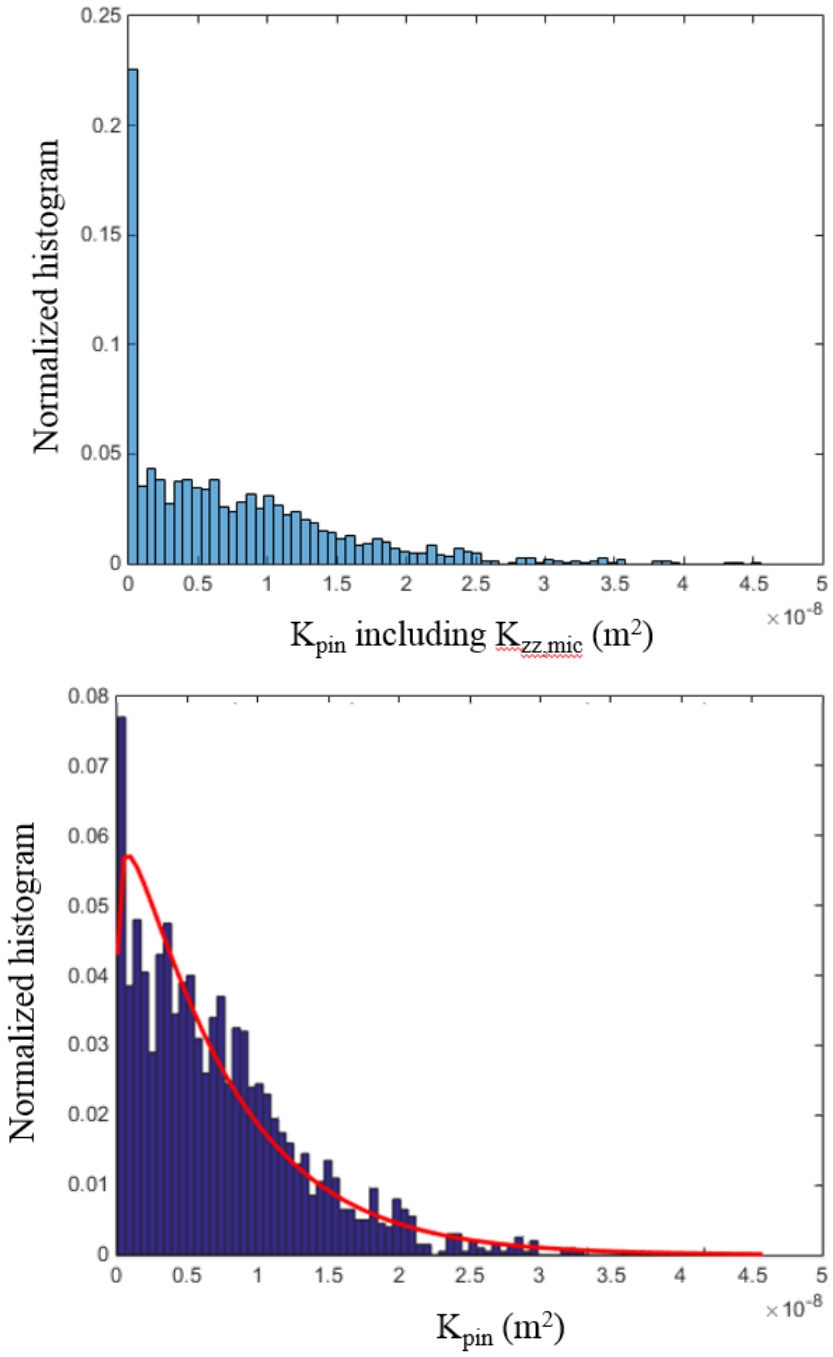

Figure 4.5 Probability Distribution Function (PDF) of K_{pin} including $K_{zz,mic}$ (Top) and K_{pin} without $K_{zz,mic}$ (Bottom). Red line represents the fit using a gamma distribution.

Basic statistical properties such as mean and standard deviation were calculated for the whole area analyzed (~ 2 m^2) and are provided in Table 4.1.

Table 4.1 Mean and standard deviation of calculated K_{pin} from image analysis

Fabric Area (m^2)	1.936
K_{pin} Mean (m^2)	9×10^{-9}
K_{pin} Standard deviation (m^2)	9×10^{-9}

Spatial correlation of K_{pin} is another critical statistical property which is obtained using a semi-variogram function. Semi-variogram ($\gamma(h)$) is a measure of the spatial correlation between two random values at a function of distance (h).

$$\gamma(h) = \frac{1}{2N(h)} \sum_{i=1}^{N(h)} (Kpin(z_i) - Kpin(z_i + h))^2 \tag{4.4}$$

In the semi-variogram given in Equation 4.4, z is the coordinate of the random variable, $N(h)$ is the total number of pairs of random variables at a lag distance h, $Kpin(z)$ is K_{pin} value at the z location, and $Kpin(z + h)$ is K_{pin} value at $z + h$ location. A semi-variogram of $(10^8)\times K_{pin}$ is obtained and plotted in Figure 4.6. An exponential function is fitted to the experimentally obtained semi-variogram as shown in Figure 4.6. The exponential semi-variogram function is given by Equation 4.5. The exponential covariance function is presented in Figure 4.6. Here h is selected to be 5mm which is the width of a tow of the selected plain woven fabric.

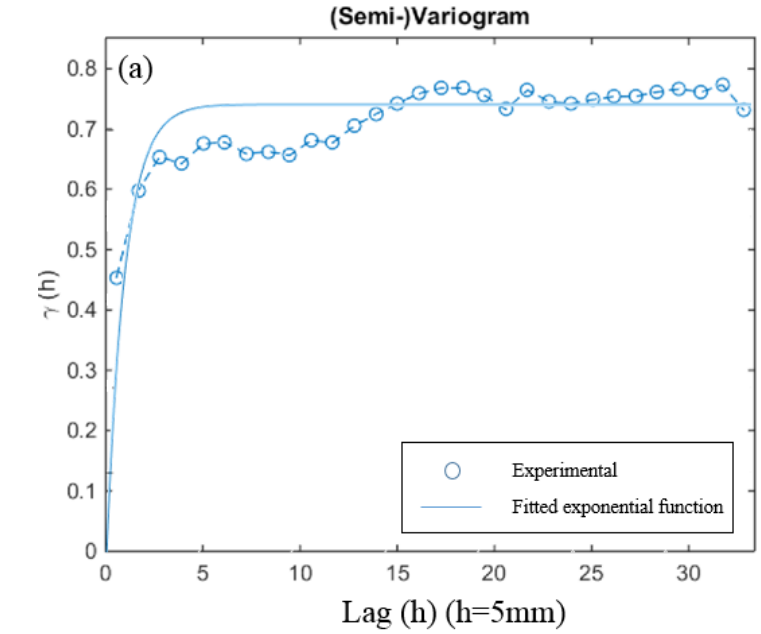

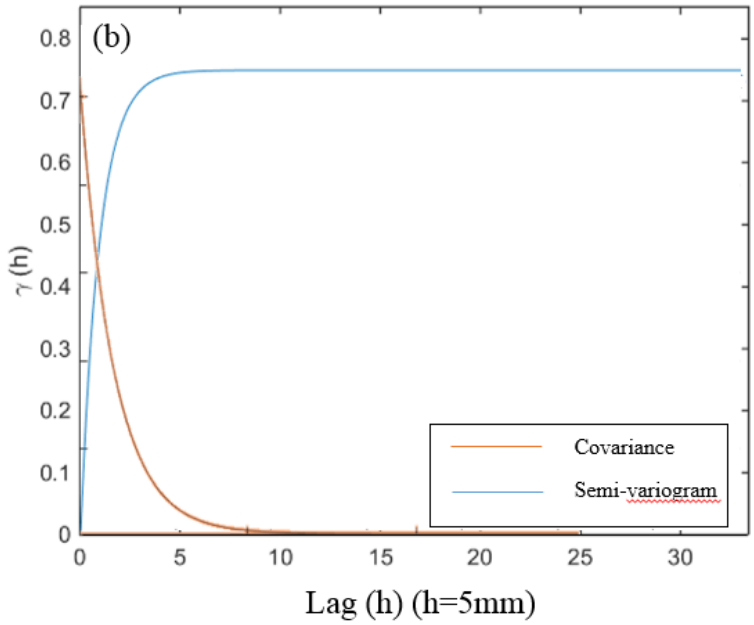

Figure 4.6 (a) (Semi-) variogram of (10^8) K_{pin} (b) Exponential function fitting semi-variogram and covariance exponential function.

$$\gamma(h) = \sigma^2\left(1 - \exp\left(-\left|\frac{3h}{a}\right|\right)\right) \tag{4.5}$$

$$C(h) = \sigma^2 \exp(-\left|\frac{3h}{a}\right|) \quad (4.6)$$

In Equations 4.5 and 4.6, σ^2 is the maximum variance of the spatial process of the sample data (sill), in which the semi variance reaches 95% of the maximum variance, and h is the spatial distance between two data points. The semi-variogram exponential function and the corresponding covariance function are presented in Figure 4.6 b. The exponential fit in Figure 4.6 (b) has a value of σ^2 of 0.73 (sill) and a value of 3 (15mm) 95% of sill (maximum variance) value is reached at the distance of h of 3 (15mm) and 99% is reached at 5 (25mm). Semi-variance varies a little over the distance lag of 5(25mm) to 15 (65mm). This means that K_{pin} values are spatially correlated within a distance of up to 15(65mm). As the tow shifts or curves, the size of nearby pinholes (K_{pin} value) are affected and this influence is found to be within the distance range (15 tows or 65mm).

4.2.4 K_{pin} cluster analysis: Moran's I

As can be seen in Figure 4.4, the total random field consists of two parts: *no pinhole areas* and *pinhole areas.* The location of *no pinhole areas* must be identified so that $K_{zz,mic}$ can be assigned to these areas. The generated K_{pin} is then assigned to the remaining area in a random field. The spatial correlation between these areas (*no pinhole* and *pinhole areas*), which is the degree of clustering, is investigated using Moran's *I* index. Moran's *I* index varies from -1 (negatively correlated) to 1 (positively

correlated) depending on the spatial correlation of the random values in the domain. Moran's *I* is described in Equation 4.7.

$$I = \frac{n}{\sum_{i=1}^{i=n}\sum_{j=1}^{j=n} W_{ij}} \frac{\sum_{i=1}^{i=n}\sum_{j=1}^{j=n} W_{ij}(x_i - \bar{x})(x_j - \bar{x})}{\sum_{i=1}^{i=n}(x_i - \bar{x})^2} \tag{4.7}$$

Where W_{ij} is the binary weight matrix, x_i is K_{pin} at location i, x_j is K_{pin} at location j, and $\bar{x}$ is the global mean of K_{pin}, n is a total number of K_{pin}.

The effect of size of sample on Moran's I index was also studied. This is to investigate if the value of Moran's I is affected by size of fabric sample to be studied. The shape of sample is square. The calculated Moran's I with varying size of sample is shown in Figure 4.7. This shows that Moran's *I* index rapidly increases up to a specimen width of 50 mm and slowly increases up to 100mm. The value of Moran's I saturates to 0.30 for specimen widths exceeding 100 mm. This indicates that the optimum fabric sample size for random field generation should be 100 mm x 100 mm over which the Moran's I index is independent of the size of sample. The unit size for generating a random field used is therefore 105 mm x 105 mm, which is also over the maximum distance required for the spatial correlation between K_{pin} (max 65mm). Figure 4.8 presents two examples of samples, each with an index of 0.30 and a size of 105 mm by 105 mm.

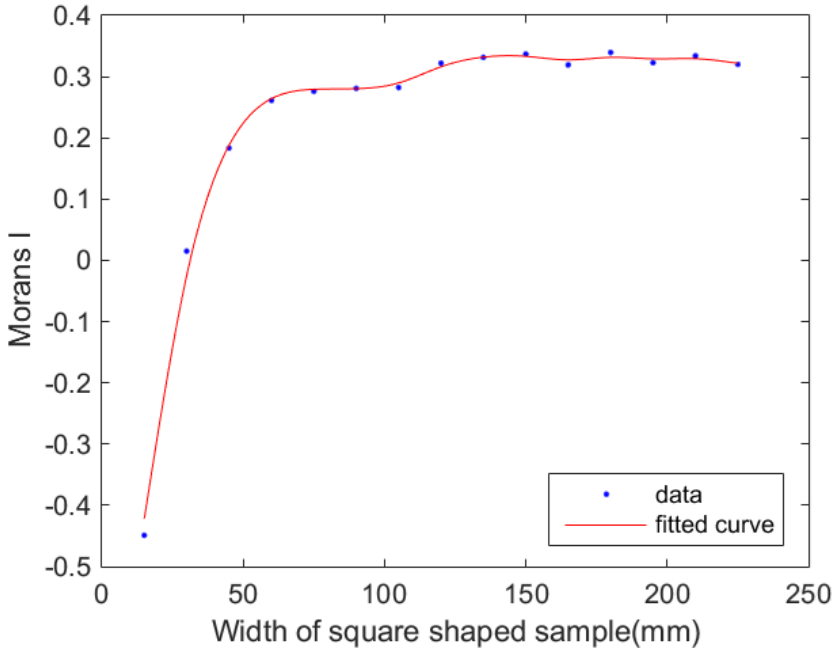

Figure 4.7 Moran's I index calculated with varying sample sizes.

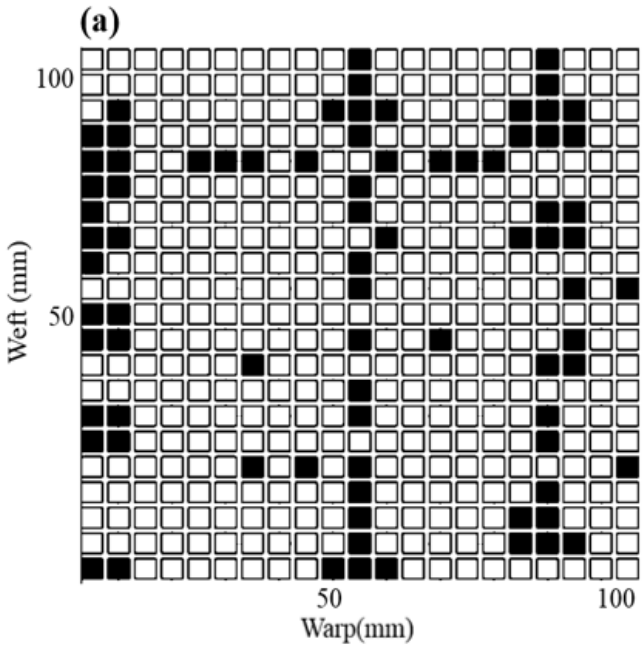

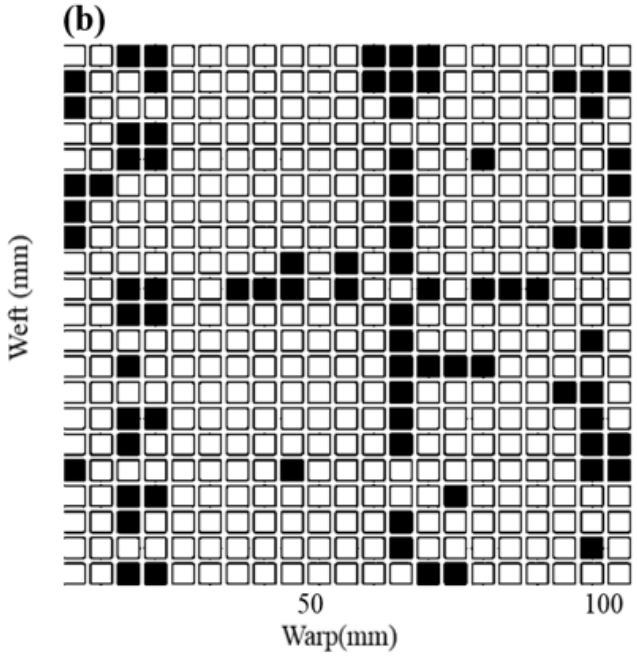

Figure 4.8 Two examples (a,b) of a unit size of matrix with Moran's I of 0.3. White area represents pinhole areas and black area represents no pinhole areas

In Figure 4.8, black areas (*no pinhole areas*) have $K_{zz,mic}(8.2\times10^{-14}m^2)$ assigned, and white areas (*pinhole areas*) have K_{pin} assigned. Finally, it remains to generate K_{pin} to be assigned. The generation of K_{pin} values is documented in detail in the following section.

It's worth emphasizing again that the determined unit size of 105mm x 105mm is the size of fabric of interest which needs to be sampled for random field generation. The unit fabric size of 105mm by 105mm (~.01 m^2) is over two orders of magnitude smaller than the sample size of $2m^2$ used in the previous chapter in which statistical analysis was not carried out and random field for numerical simulation was obtained by sampling larger size of fabric. The statistical study of spatial correlation of random values introduced here determines the necessary sample size to generate random fields,

which greatly reduces the effort and time to collect data from unnecessarily large sizes of samples.

4.2.5 Transformation between gamma and normal random variables

As mentioned above, the PDF of K_{pin} fits a gamma distribution rather than a normal distribution. Usually, random numbers can be easily created with the normal distribution function. However, in this case, it is difficult to obtain the random numbers because they are gamma random numbers and it's known to be difficult to generate gamma numbers directly. So, if possible, normal random numbers are generated instead and the numbers can be transformed to gamma numbers. In this study, characteristics of the fit gamma distribution function such as covariance function is transformed to one of normal distribution. The transformed covariance function is used as an important input to a Gaussian random generator such as KL expansion[95]. The Gaussian random generator creates normal random numbers. The obtained normal random numbers are then transformed to gamma random numbers. The transformation between gamma and normal random numbers is conducted with the method presented in the work by Liou et al. [95].

The very first step of this process, transformation of gamma covariance function to normal one, is carried out using the Equations 4.8-4.9. In Equation 4.8, *x* is a gamma random variable (X~G (α, λ)) and $f_X(x)$ is the gamma random variable density, α is a shape parameter, and λ is a scale parameter.

$$f_X(x) = \frac{\lambda^\alpha}{\Gamma(\alpha)} x^{\alpha-1} e^{-\lambda x}, \alpha, \lambda > 0 \; and \; 0 \leq x \leq +\infty \tag{4.8}$$

For the $(10^8)\times K_{pin}$ fitted gamma distribution, α is 1.08 and λ is 1.16.

The covariance function of two normal variables w_1 and w_2 (ρ_{W1W2}) is related to the covariance function of two gamma variables x_1 and x_2 as shown in Equation 4.9. Using the Equation 4.9, the covariance function of normal variables is obtained.

$$COV(x_1, x_2) \approx \left(\frac{\alpha_1}{\lambda_1}\frac{\alpha_2}{\lambda_2}\right)\left(A + B\rho_{W_1W_2} + C\rho_{W_1W_2}^2 + D\rho_{W_1W_2}^3\right) - \left(\frac{\alpha_1}{\lambda_1}\frac{\alpha_2}{\lambda_2}\right) \quad (4.9)$$

$$\xi_1 = \left(\frac{1}{\alpha_1}\right), \xi_2 = \left(\frac{1}{\alpha_2}\right)$$

$$A = (1-\xi_1)^3(1-\xi_2)^3 + 3(1-\xi_1)\xi_1(1-\xi_2)^3 + 3(1-\xi_1)^3(1-\xi_2)\xi_2 + 9(1-\xi_1)\xi_1(1-\xi_2)\xi_2$$

$$B = 9(1-\xi_1)^2\xi_1^{0.5}(1-\xi_2)^2\xi_2^{0.5} + 9\xi_1^{1.5}(1-\xi_2)^2\xi_2^{0.5} + 9(1-\xi_1)^2\xi_1^{0.5}\xi_2^{1.5} + 9\xi_1^{1.5}\xi_2^{1.5}$$

$$C = 18(1-\xi_1)\xi_1(1-\xi_2)\xi_2$$

$$D = 6\xi_1^{1.5}\xi_2^{1.5}$$

The conversion of covariance functions works well when $\alpha_1, \alpha_2 > 0.5$.

α_1 *and* α_2 are calculated to be 1.08. A coefficient of skewness (γ_1) is less than 3. Using Equation 4.10, γ_1 is calculated to be 1.9.

$$\gamma_1 = \frac{\frac{(\alpha+1)(\alpha+1)\alpha}{\lambda^3} - 3\frac{\alpha}{\lambda}\frac{\alpha}{\lambda^3} - \frac{\alpha^3}{\lambda^3}}{\left(\frac{\alpha}{\lambda^2}\right)^{\frac{3}{2}}} = \frac{2}{\sqrt{\alpha}} \quad (4.10)$$

Next, the covariance of normal numbers is used to generate normal random numbers (w) in the KL expansion process. Then the numbers (w) are transformed back to gamma random numbers (x) point by point using Equation 4.11.

$$x = \frac{y}{2\lambda} \approx \frac{\alpha}{\lambda}\left\{1 - \frac{1}{9\alpha} + w\sqrt{\left(\frac{1}{9\alpha}\right)}\right\}^3 \tag{4.11}$$

These generated gamma random numbers (x,K_{pin}) through the transformation are assigned to the *pinhole areas* (white areas in Figure 4.8) in a random field of Moran's *I* index of 0.3.

4.2.6 Random number generation:

4.2.6.1 Karhunen–Loève (KL) expansion

KL expansion represents an infinite stochastic process which is a type of Fourier expansion as presented in Equation 4.12. KL expansion generates normal random numbers

$$w(x,\theta) = \overline{w}(x) + \sum_{i=1}^{\infty}\sqrt{\lambda_i}\xi_i(\theta)f_i(x) \tag{4.12}$$

In Equation 4.12, w is a normal random function, $\overline{w}$ is a mean value, ξ is a Gaussian random number, λ is eigenvalue, and $f(x)$ is orthonormal eigenfunction of a covariance function (kernel, ρ). The eigenvalues and eigenfunctions are obtained by solving the integral equation over the domain Ω presented in Equation 4.13.

$$\int_{\Omega} \rho(x - x')f(x')dx' = \lambda f(x) \tag{4.13}$$

Where $\rho(x - x')$ is the covariance function.

Its infinite series can be properly truncated with a right value by studying the decay of eigenvalues. The truncation step is well described in the next step.

4.2.6.2 Application of KL expansion

The transformed covariance function of normal random numbers was used in the normal random generator, KL expansion, to generate gaussian normal random variables (w(x,θ)) in Equation 4.14.

$$w(x,\theta) = \overline{w}(x) + \sum_{i=1}^{N} \sqrt{\lambda_i}\xi_i(\theta)f_i(x) \tag{4.14}$$

In Equation 4.13, λ_i and $f_i(x)$ are the eigenvalues and eigenfunctions of the covariance function, $\xi_i(\theta)$ is a normal random variable with mean of 0 and variance of 1, $\overline{w}(x)$ is the mean of normal random variables which is 0, and N is the finite number of terms which is 33 determined by studying the estimated decay of eigenvalues. The sum of 33 eigenvalues reaches 92% of sum of total eigenvalues

4.2.7 Numerical simulation

To study the effect of K_{pin} values and through thickness permeability On flow, LIMS is used the details of which are provided in Appendix A and [75]. The woven fabric with pinholes was modeled into 3D mesh with 1D elements representing the pinhole values for the simulation. The mesh is shown in Figure 3.5. Four layers of fully nested fabrics (0.12 m by 0.53 m) and pinholes are simulated using 3D elements (representing the woven fabric) and 1D elements (representing the pinholes). The thickness of each layer of fabric is 0.7 mm under vacuum (fully nested). One layer of DM (0.11 m by 0.48 m) with thickness of 1 mm is simulated using 2D elements. The permeability tensor of the woven fabric was obtained experimentally using the methodology presented in chapter 2 and [30]. The bulk permeability is presented in Table 4.2.

Table 4.2 Permeability of the plain woven fabric

$K_{xx}(m^2)$	$K_{yy}(m^2)$	$K_{zz}(m^2)$	$K_{xz}(m^2)$	$K_{yz}(m^2)$	$K_{xz}(m^2)$
8.8×10^{-11}	9.1×10^{-11}	1.36×10^{-12}	9.89×10^{-16}	1.58×10^{-15}	1.00×10^{-15}

The K_{pin}, generated using the methodology described earlier, was assigned to the 1D elements. Three values of DM permeability (K_{DM} of $1.45 \times 10^{-08} m^2, 8.5 \times 10^{-09} m^2,$ and $4 \times 10^{-09} m^2$) were used to study the effect of K_{DM} on void formation. Other experimental conditions such as fabric volume fraction, pressure, and viscosity are presented in Table 4.3.

Table 4.3 Experimental condition for numerical simulation study

Fabric volume fraction	0.45
Pressure (Pa)	1×10^{5}
Viscosity (Pa.s)	0.1

Monte Carlo simulations were conducted for each type of DM. The number of iterations for each DM type is determined using a method presented in [96]. The equation to calculate the necessary iteration number is presented in Equation 4.15.

$$n = \frac{100 z_c S_x}{E \bar{x}} \tag{4.15}$$

In Equation 4.15, z_c is a confidence coefficient, S_x is sample standard variation, E is a percentage error of the mean, and $\bar{x}$ is the mean. For 95% confidence level and 5% error, z_c is 1.96, S_x and $\bar{x}$ are presented in Table 4.4, and E is 5. Using this, the number of runs n is calculated to be 134 for K_{DM} of 1.45×10^{-08} , 232 for K_{DM} of 8.5×10^{-09}, and 543 runs for K_{DM} of 4×10^{-09}. Mean of void fraction as a function of run number is presented in Figure 4.9. It shows that 440 runs are sufficient for the case of K_{DM} of 4×10^{-09} because the value of mean of void fraction asymptotes by 440 runs.

(a) DM 4×10^{-9}

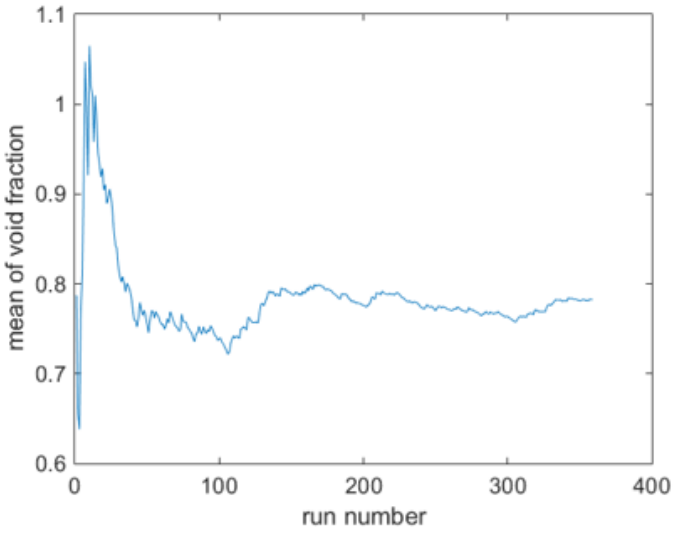

(b) DM 8.9×10^{-9}

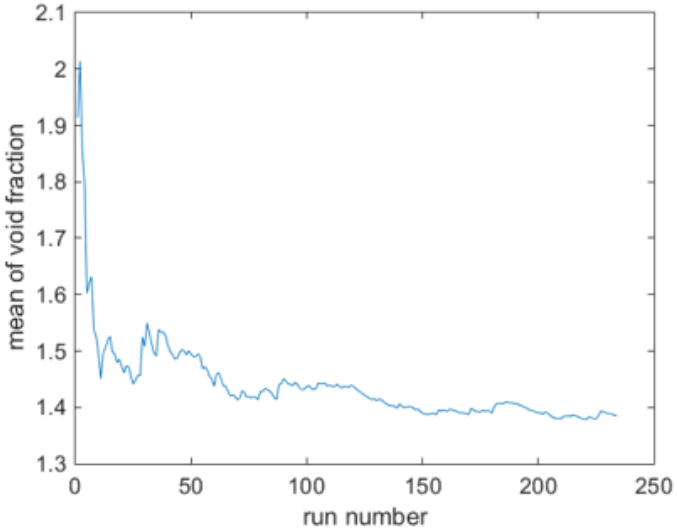

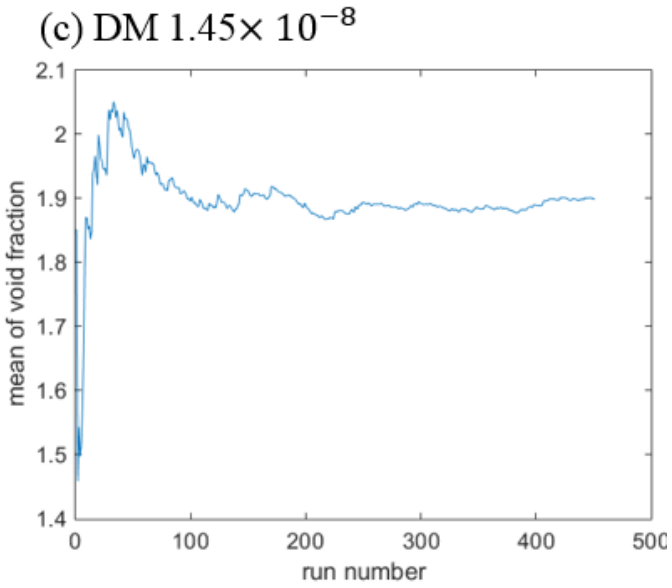

Figure 4.9 Mean of void fractions as a function of run number in Monte-Carlo simulations ((a) DM 4e-09m^2 (b) 8e-09m^2 (c) 1.45e-08 m^2)

The random K_{pin} field is generated for each simulation run. The void fraction was calculated as the area of the void divided by the mold area. The simulation result (void fraction) from this study was compared to the void fraction found in the experimental work and the simulation work with an experimentally determined K_{pin} field presented inthe previous chapter.

4.3 Results and discussion

4.3.1 K_{pin} random field

The properties of $(10^8)K_{pin}$ random field generated using the methodology described earlier are presented in Table 4.4. The parameters of the probability density function of the gamma distribution, α and λ, fits the values of the observed K_{pin} fields

within 5% error. The parameter of semi-variogram, σ^2, also matches the experimentally observed value within 5%.

Table 4.4 Parameters of generated density function and the semi-variogram model [From observed (10^8)K_{pin} field, α=1.08,λ=1.16,σ^2=0.73]

	α	λ	σ^2
Simulation	1.04~1.14	1.08~1.19	0.70~0.76
Experiment	1.08	1.16	0.73
Error	$\pm$4.5%	$\pm$4.8%	$\pm$4.3%

4.3.2 Numerical simulation

The normalized histogram of void fractions obtained from the simulation runs for each type of DM is presented in Figure 4.10.

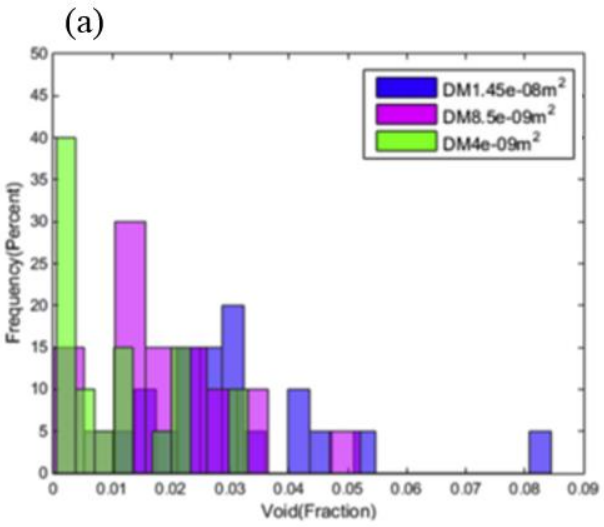

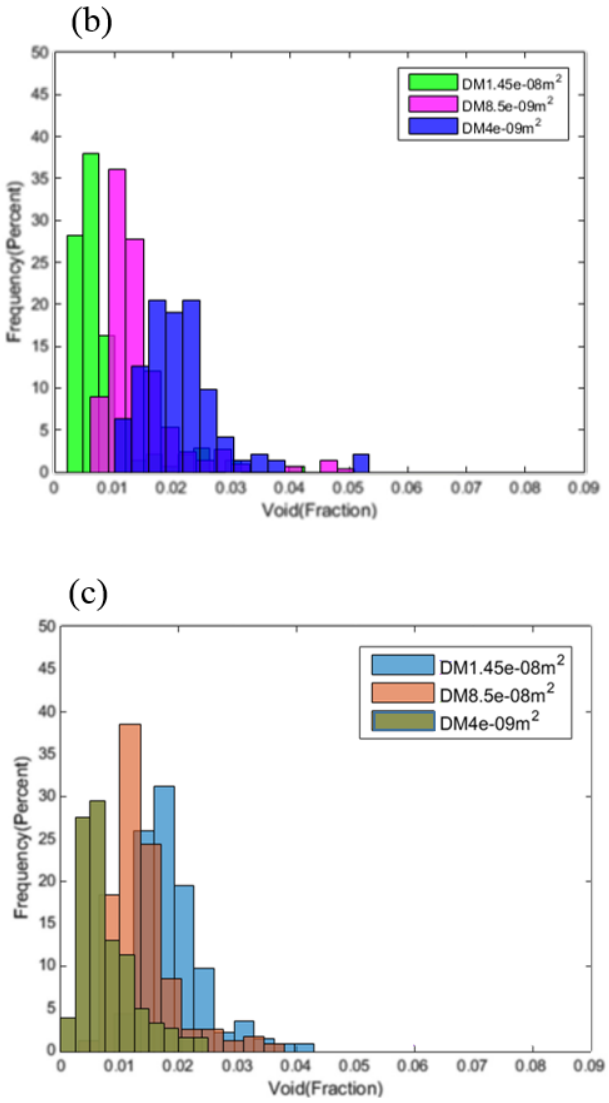

Figure 4.10 Histogram of void percentages in the bottom layer calculated from both experimental (a), simulation with experimentally obtained K_{pin} fields (b), simulation with generated K_{pin} fields (c). Different colors represent different K_{DM} magnitude.

In Figure 4.10, the experimental result is given in (a), simulation result using experimentally determined K_{pin} fields is presented in (b), and the simulation result using generated K_{pin} fields is presented in (c). The results with generated random field qualitatively match the other two results. It shows the trend of void fraction increasing

with higher K_{DM}. The void percentages for all three case studies are presented in Table 4.5. This confirms that it is possible to generate the behavior of flow in a fibrous porous media through statistical analysis of the fabric pinholes by characterizing a small sample of the fabric.

Table 4.5 Void percentage obtained from (a) experimental and (b-c) simulation runs. ((b) Simulation 1 : simulation with experimentally determined K_{pin}, (c)Simulation 2: simulation with generated K_{pin} field)

K_{DM} (m^2)	(a)Experimental study Void (%)			(b)Simulation 1 Void (%)		
	Range (%)	Mean (%)	Standard deviation	Range (%)	Mean (%)	Standard deviation
1.45×10^{-08}	1.00~8.45	3.15	1.63	1.14~5.32	2.12	0.72
8.5×10^{-09}	0.19~5.21	1.59	0.77	0.63~4.74	1.40	0.67
4×10^{-09}	0.0005~3.33	1.09	1.00	0.2~4.11	0.80	0.71

K_{DM} (m^2)	(c)Simulation 2 Void (%)		
	Range (%)	Mean (%)	Standard deviation
1.45×10^{-08}	1.06~4.26	1.90	0.56
8.5×10^{-09}	0.31~3.72	1.39	0.54
4×10^{-09}	0.12~3.33	0.79	0.47

4.4 Conclusion

In this study, the methodology to generate gamma random field is presented. The K_{pin} random field with a gamma distribution was successfully created based on the statistical analysis using the methodology. The spatial correlation between *pinhole* and *no pinhole* areas was studied using Moran's *I* index. The covariance function of gamma random numbers was converted to the covariance function of normal random numbers. The converted normal covariance function was then used for KL expansion to generate Gaussian normal random numbers. The normal numbers were converted to gamma random numbers. The property of density function and a semi-variogram of generated K_{pin} field matched well with experimentally obtained K_{pin} samples. The results of numerical simulations also show reasonable match with the experimental results and simulation results using experimentally obtained K_{pin} fields. Through the statistical study, the properties of randomness such as correlation length and Moran's *I* index are well understood and generation of the random field is possible. Using this methodology, a proper size of fabric sample (105mm x 105mm) which needs to be studied was found and hundreds of random fields were generated for numerical simulation, which eliminated the need to sample a large size of fabric to obtain K_{pin} random field. This methodology to generate random fields is useful to characterize variability with a small sample of the fabric and determine its effect on manufacturing by predicting flow behavior and void formation in the presence of heterogeneity in a VARTM process. It should prove useful for numerical simulations of a manufacturing process of large composite parts.

The Kpin random field can be created once a woven fabric is identified with the statistical properties (α and MI). A new methodology to identify these properties efficiently is presented and explained in detail in the following chapter.

Chapter 5

Manifold embedding of heterogeneity in permeability of a woven fabric for optimization of the VARTM process

5.1 Introduction

There are several reported causes for the stochastic variation in the permeability values of a fabric. Variation in the fabric architecture, handling of layers as they are placed over a tool surface, placement of the layers that nest to form the preform, and the manufacturing process all play a role[14,69]. Chapter 3 and 4 has demonstrated that there is an inherent randomness in through the thickness permeability of any woven fabric which can locally cause large variations in resin flow in through the thickness direction resulting in void formation. The inherent variation in through the thickness permeability arises from the varying size of meso-scale spaces (pinholes) between woven tows. An example of an image of a woven fabric is presented in Figure 5.1(a). The raw picture of a woven fabric is given in Figure 5.1(a) and a filtered image using a proper threshold by MATLAB is presented in Figure 5.1(b).

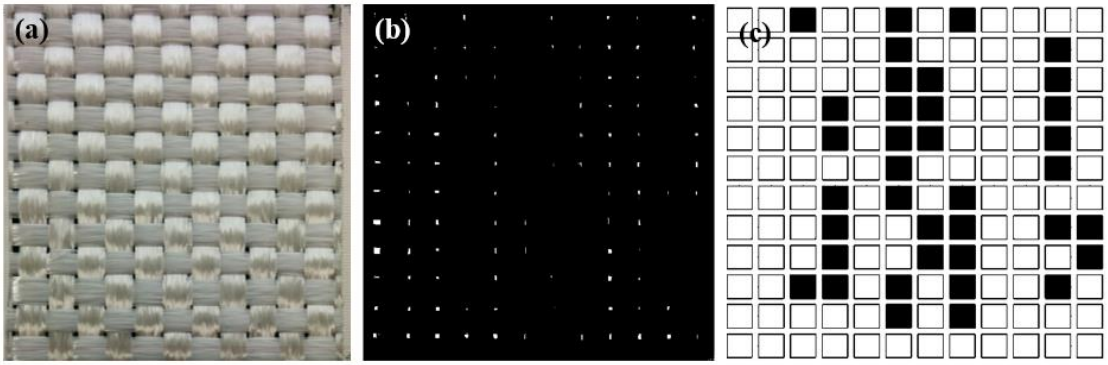

Figure 5.1 Image of E-glass fabric (60mm by 60mm) (a), binary image (b), and pinhole matrix(c). Black indicates no pinhole area and white signifies presence of pinhole.

The pinholes of varying sizes act as easy pathways for resin from the DM to race through the thickness direction to reach the bottom layer of the stacked layers of fabrics. This results in uneven flow and possible merging of the flow fronts trapping air which forms the voids. The varying sizes and locations of the pinholes are statistically characterized with two statistical properties : a distribution function fit to the histogram of calculated permeability of pinholes (K_{pin}) and spatial correlation of pinhole areas[97]. The method to calculated K_{pin},α, and MI is well described in Section 4.2. The distribution function best fit to the histogram is found to be gamma distribution and one of its parameter, the shape factor α, has been explored to investigate its effects on the overall K_{pin}. The example of the gamma distribution fitting the histogram of pinhole permeability of the fabric presented in Figure 5.1 is displayed in Figure 5.2 (a)[97]. The gamma distribution shifts to the right as α increases from 1 to 4 as seen in Figure 5.2 (b).

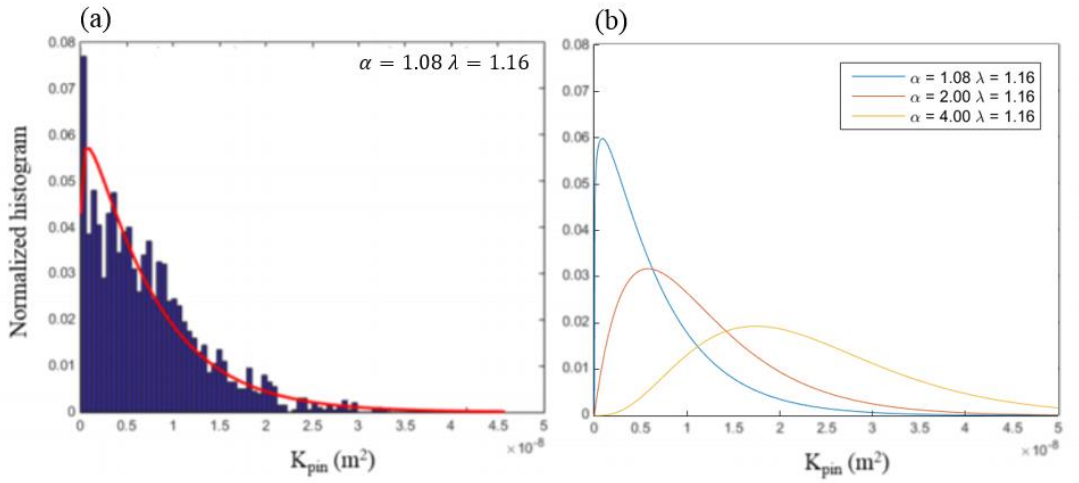

Figure 5.2 Histogram of pinhole permeability of a plain woven fabric in Figure 2 and its best fit gamma distribution function (a) and gamma distributions with varying α (b)

Physically this means that as α increases the average pinhole size increases and consequently K_{pin} values also increase. The spatial correlation between pinhole areas and no pinhole areas is visually shown in Figure 5.1 (c) as a matrix composed of black (no pinhole) and white (pinhole) areas. Moran's I (MI) is a statistical measure of spatial correlation[94]. For this study, MI is used to study the spatial relationship between pinhole areas and no pinhole areas. The examples of varying MI are presented in Figure 5.3. The value of MI varies from 0 (no spatial correlation) to 0.5 (statistically significantly positively correlated). The range for these two important parameters of K_{pin} field to describe the fabric variability (α of 1 to 4 and MI of 0 to 0.5) should cover most of the woven fabrics. The mean radius of a pinhole as α increases from 1 to 4 increases from 0.7mm to.1.7mm. One will rarely encounter a woven fabric with pinhole size between two tows to be larger than 1.7 mm. For MI, one is hardly likely to encounter a woven fabric of MI over 0.5 as can be seen in Figure 5.3. The sample with

MI of 0.5 as shown in (c) and (d) of Figure 5.3 shows the pinholes arranged in highly ordered manner which is highly unlikely with random variability of pinholes in terms of positions.

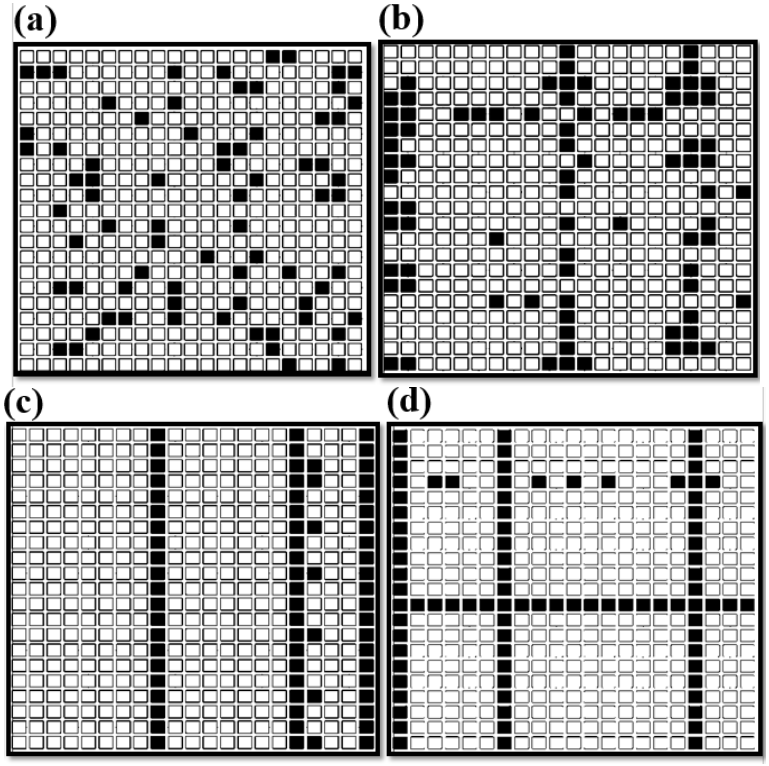

Figure 5.3 Samples of 21x21 mesh size and varying Moran's I. MI of 0 (a), 0.3 (b), and 0.5 (c and d representing two different realizations)Black indicates no pinhole area and white means pinhole area.

Numerical simulations were carried out to study the effects of MI and α on the flow pattern of resin and resulting void percentage. Table 5.1 shows the effect of these two parameters of fabric on the void percentage formed in a VARTM process. Liquid Injection Molding Simulation (LIMS) was utilized to run numerical simulations that describe Darcy's flow of resin into an anisotropic fabric in a 3D mold in which pinholes can be introduced in through the thickness direction. The implementation of pinhole

permeability is well described in chapter 4. The pinhole location and size were selected by the value of α and MI. Note that although α and MI value may be same, the distribution of pinholes and their correlation matrix can embody different patterns. The DM permeability can also be changed but was set to 1.4×10^{-8} m^2. Mean percentage of voids by running 150 simulations for a given α and MI was found to increase with increasing α and MI. This is a predictable result because higher value of α results in higher permeability of pinholes and higher value of MI leads to more highly clustered pinhole spaces (positive correlation between pinhole areas).

Table 5.1 Void percentage obtained from numerical simulation with varying α and MI (MI)

	α= 1 MI= 0	α= 1 MI= 0.3	α= 1 MI= 0.5	α= 2 MI=0.3	α= 4 MI= 0.3
Range (%)	0.7~2.6	0.9~3.8	0.9~4.6	1.3~4.2	1.3~4.3
Mean (%)	1.35	1.90	2.05	2.30	2.54
Standard deviation (%)	0.37	0.65	0.75	0.47	0.50

Characterizing the fabric with these two parameters in real time can allow one to forecast the possible void percentage in a VARTM process for a given value of DM permeability. Machine learning methods are effective in achieving this goal of identifying a fabric with these two parameters quickly.

5.1.1 Machine learning

Machine learning is a field of Artificial Intelligence (AI) to train computer system to learn from data automatically to make future decisions without being explicitly

programmed. Machine learning can be divided into 4 categories: supervised learning, unsupervised learning, semi-supervised learning and reinforced learning.

First, supervised learning is where human teacher trains an algorithm or system with labeled input data with the output. The input value is labeled with information and fed to the system for training. After training step, the system can classify or define new incoming data based on the training. Examples of supervised learning examples are decision tree, neural network, and regression model[98–101].

Unsupervised learning involves incoming data without labels. In this case, human teacher is not sure how or what to look for in the data. Pattern recognition or clustering is used to find a meaningful trend or helpful information from the data. Examples include dimensionality reduction method (Principal Component Analysis, Locally Linear Embedding etc), k-mean clustering and association rule learning[102–104].

Semi-supervised learning is to train the system with labeled and unlabeled data. This method is very useful when all the input data are not labeled. Obtaining labels for all the data is a time consuming task. The key for this method is how to combine the unlabeled and labeled input data for the learning process. Examples can be found in [105].

Reinforced learning a type of machine learning process which learns the interaction of actions with an environment which provides rewards as shown schematically in Figure 5.4. The agent (the system) is first notified of the state in which decision (action) needs to be made. The agent makes the action in the environment then receives a feedback of risk or reward. The agent (system or algorithm) tries to maximize the reward or minimize the risk by learning the interactions. Reinforcement learning examples includes Q- learning and temporal difference[106,107]. More familiar application

examples would be board games such as chess or go, self-driving cars and robotic hands.

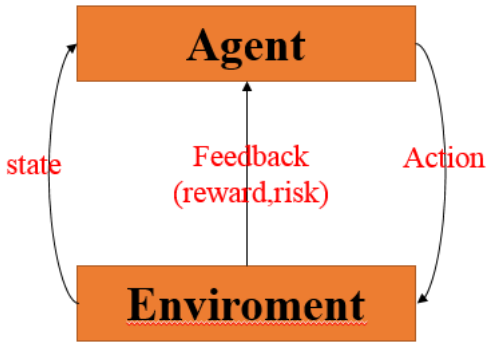

Figure 5.4 Diagram of reinforced learning process

Linear and non-linear dimensionality reduction methods are types of unsupervised learning processes which visualize and characterize a group of high dimensional input data through a reduction of dimensionality. Dimensionality reduction aims to plot the original data of high dimension in lower dimensional space so that the visual inspection or data analysis are more viable to users. Machine learning methods such as Principal Component Analysis (PCA), t – Distributed Stochastic Neighboring Embedding (t_SNE), and Locally Linear Embedding (LLE) are widely used to treat image, voice, and other types of samples with a high dimension [98,102,104,108–115]. PCA is a linear dimensionality reduction method which consists of principal components. The principal components are eigenvectors of covariance matrix of input data[113].More detailed explanation of the method is given below in the methodology section. PCA has been used prevalently for its simplicity and efficiency. Kim et al reported the use of PCA for face recognition[116]. X-ray pictures of breast has been subject to PCA for feature extraction/analysis[98].

LLE method embeds the original data in a lower dimensional space using a weight matrix obtained in the original space[110]. The weight matrix is obtained by minimizing the functional given in Equation 5.1.

$$F(W) = \sum_{i=1}^{M} \left\| \chi_i - \sum_{j=1}^{k} W_j^i \chi_j \right\|^2 \tag{5.1}$$

Where χ_i is a vector of the coordinate of ith point, χ_j is a vector of the coordinate of jth point, W_i^j is a weight matrix, M is the number of points in the original space and k is the number for k-nearest neighbors.

The data of heterogeneous thermal conductivity field has been processed using LLE to interpolate the temperature field[110,115]. Teng et al reported a study to recognize Chinese hand gestures using LLE[117].

t_SNE is a type of SNE which is non-linear dimensionality reduction method. t_SNE unlike PCA or LLE deals with stochastic probability method which could be useful to preserve important information from original space in a lower dimensional space. It maps the original data to a lower dimensional space by minimizing the cost function of probability distribution of neighboring data over input data. The detailed explanation is given in methodology section (5.2.2.2). The application of t_SNE can be found in [98,109,111].

These techniques visualize and characterize a large number of samples with a high dimension in either two or three dimensional space (map). In this study, the map refers to a 2D or 3D representation of high dimensional input data obtained through manifold learning techniques. The map is a useful co-relation tool as it helps one to identify

which cluster the new sample will belong to in the map and this way the new sample can be classified accordingly.

The objective of this study is to identify two important parameters (α, MI) from a high dimensional input using dimensionality reduction methods (PCA and t_SNE) to predict the void contents in a composite part by running numerical simulations.

5.2 Methodology

Two charts of the entire procedure which provides the void fraction range from an image of the fabric in real time is presented in Figure 5.5.

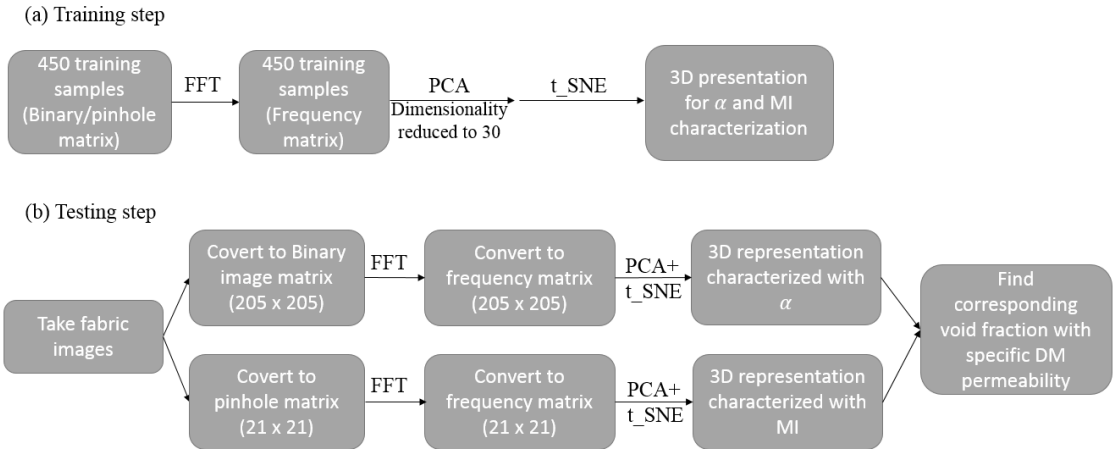

Figure 5.5 Flow charts showing the process to obtain void fraction from an image of the fabric. Training step (a) and testing step (b)

The procedure consists of a training step and a testing step. For this study, a total of 450 samples for 9 cases (3 MIs of 0, 0.3, and 0.5 and 3 αs of 1, 2, and 4) are used as a training data set. The detailed procedure to create the training samples is well documented in Chapter 4. In the training step, 450 images and matrices are first processed to generate frequency filtered version of input data by Fast Fourier

transformation (FFT). The frequency matrices are further processed by PCA first to identify the important frequencies and ignore the others. Then, the more advanced t_SNE machine algorithm is applied to create 3D maps in which the input samples are separated based on α and MI. Once the maps in three dimensions show clear separation for these parameters, a binary image of a new sample of fabric is subjected to the machine learning methods in the testing step which will place it in a cluster of the created 3D map thus identifying its α and MI value. Once these two parameters are known, the numerical simulations were performed with these values of α and MI for different DM permeability values. The corresponding range of void fractions can then be forecasted from the numerical simulations of the VARTM process from using just the binary image of the fabric sample.

5.2.1 Image processing

There are two types of image samples for the process. This binary image of size 205 x 205 (dimensionality of 44100) pixels in Figure 5.1 (b) is one type of input data which is obtained by filtering the original image with a selected threshold. The binary image contains the information of both the size and the location of the pinholes. The second input data is a pinhole matrix of size of 21x21 (dimensionality of 441) produced from the binary image as shown in Figure 5.1 (c). Each cell of the matrix has information contained in 5mmx5mm square of the binary image. The distance of 5mm is the average distance between pinholes (tows) which lie horizontally or vertically. MATLAB is employed to transform the images into the binary matrix. The accuracy of the process of importing images is well documented in Chapter4.2.3. The matrix elements are composed of 1 (no pinhole) and 0 (pinhole).

5.2.2 FFT and machine learning methods

5.2.2.1 Fast Fourier Transformation (FFT)

In order to reduce the dimensionality and the noise within the domain, the images and matrix of a woven fabric are transformed by FFT to output in a frequency domain using MATLAB [118]. FFT is a method to carry out Discrete Fourier Transformation (DFT) quickly and efficiently. DFT is a method that converts an input data in a spatial domain to output data with sine and cosine components in frequency domain. The elements in the binary image and pinhole matrix (X) are transformed to corresponding frequency (χ) by FFT. The output of FFT,χ, is a matrix with each point displaying a particular frequency which is then addressed by the machine learning algorithm PCA followed by t_SNE.

5.2.2.2 Principal Component Analysis (PCA) and t – Distributed Stochastic Neighbour Embedding (t_SNE)

PCA and t_SNE both are used to reduce the dimensionality of the processed matrix and images by FFT in this study. In PCA, the data in a principal sub-space is obtained using eigenvectors (principal components) of the covariance matrix of the input data [108,119]. t_SNE is a variation of SNE which is a nonlinear dimensionality reduction technique by minimizing a cost function of probability distributions of neighboring points over the input data. It is easier to implement and yields much better visualization in a low dimensional space than standard SNE [111,120].

The procedure begins by subtracting the mean from the processed frequency matrix, χ to obtain the matrix, D1. Covariance matrix ($\sum$) of D1 is calculated and eigenvalues and eigenvectors of the covariance matrix ($\sum$) are obtained. The *k* largest eigenvectors are then multiplied to the frequency matrix (χ) to obtain a matrix of reduced dimensionality($\chi 1$) in PCA space[116,121]. In this study, k was selected as 30 which means the initial dimensionality (44100 or 441) are reduced to 30 first eigen vectors using PCA method. The PCA treated matrix ($\chi 1$) is then processed by t_SNE to obtain a final matrix (y) of reduced dimension 3. First, the probabilities (p, q) are converted from euclidean distance between data points (in $\chi 1(\chi 1_1, \chi 1_2, \cdots, \chi 1_{n1})$ for p and y($y_1, y_2, \cdots, y_{n1}$) for q) and are presented (Equations 5.1-5.2)[111].

$$p_{ij} = \frac{\exp(-\left\|\chi 1_i - \chi 1_j\right\|^2/2\sigma^2)}{\sum_{k\neq l} exp(-\|\chi 1_l - \chi 1_k\|^2/2\sigma^2)} \tag{5.1}$$

$$q_{ij} = \frac{\exp(-\left\|y_i - y_j\right\|^2)}{\sum_{k\neq l} \exp(-\|y_k - y_l\|^2)} \tag{5.2}$$

Where σ the variance of the Gaussian is centered data point, $\chi 1_i$These pairwise similarities (probabilities, p, q) should be the same if the new map (y) models the similarities of input matrix ($\chi 1$) correctly. The cost function (C) in Equation 5.3 below measures the difference between two probabilities and it should be minimized to obtain the final matrix(y).

$$\boldsymbol{C = KL(P \parallel Q) = \sum_i \sum_j p_{ij} log(\frac{p_{ij}}{q_{ij}})} \tag{5.3}$$

The cost function, C, aims to minimize a single Kullback-Leibler divergence between p and q. The early employment of PCA in the process helps to define the main manifold from a linear dimensionality reduction perspective. It was found that FFT and PCA filters were necessary before employing t_SNE. MATLAB is employed to carry out the machine learning process implementation.

5.2.3 Numerical simulation (LIMS)

Numerical flow simulation with the generated random field where K_{pin} (permeability of a pinhole) values are assigned to through the thickness permeability allows us to study the effect of heterogeneity on the flow. LIMS was used to carry out the simulations. Details of which are provided in Appendix A, The woven fabric with pinholes in Figure 5.1 was modeled into a 3D mesh with 1D elements representing the pinhole values for the simulation. The mesh is shown in Figure 5.6.

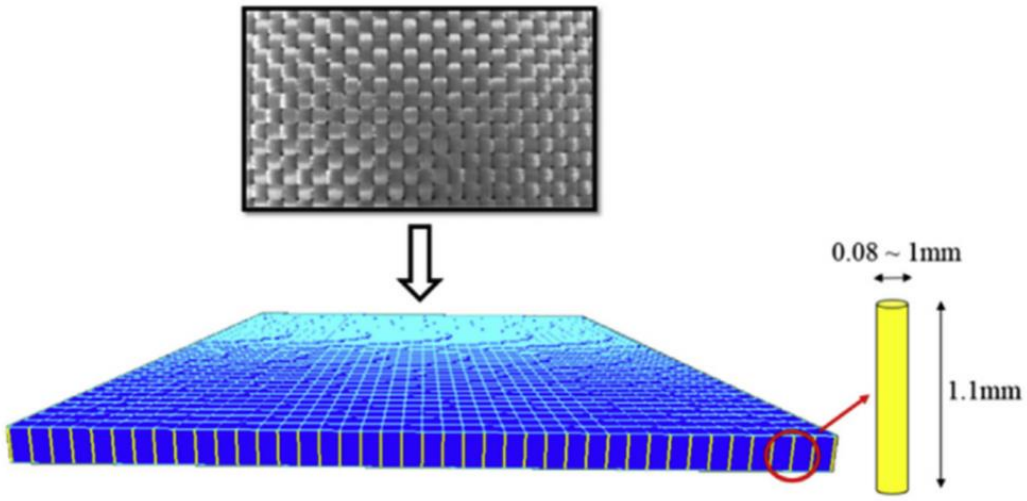

Figure 5.6 Woven fabric layer modeled as 3D elements and pinholes as 1D elements in the flow simulation

Four layers of fully nested fabrics (0.12 m by 0.53 m) and pinholes are simulated using 3D elements (representing the woven fabric) and 1D elements (representing the pinholes). The thickness of each layer of fabric is 0.7 mm under vacuum (fully nested). One layer of DM (0.11 m by 0.48 m) with thickness of 1 mm is simulated using 2D elements. The permeability tensor of the woven fabric was obtained experimentally using the methodology presented in chapter 2 and [30]. The values of the bulk permeability components are presented in Table 5.2.

Table 5.2 Experimentally determined permeability values of the components of the 3D permeability tensor of the plain woven fabric

$K_{xx}(m^2)$	$K_{yy}(m^2)$	$K_{zz}(m^2)$	$K_{xz}(m^2)$	$K_{yz}(m^2)$	$K_{xz}(m^2)$
8.8×10^{-11}	9.1×10^{-11}	1.36×10^{-12}	9.89×10^{-16}	1.58×10^{-15}	1.00×10^{-15}

The K_{pin} field was generated using the methodology documented in Chapter 4.2and was assigned to the 1D elements. Three values of DM permeability (K_{DM} of $1.45 \times 10^{-08}m^2, 8.5 \times 10^{-09}m^2,$ and $4 \times 10^{-09}m^2$) were used to study the effect of K_{DM} on void formation. Other experimental conditions such as fabric volume fraction, pressure, and viscosity are listed in Table 5.3.

Table 5.3 Experimental condition for numerical simulation study

Fabric volume fraction	0.45
Inlet Pressure (Pa)	1×10^5
Resin Viscosity (Pa.s)	0.1

The simulations were run to find the final void content. The void fraction was calculated as the area of the voids divided by the mold area. These numerical results

along with the result from the machine learning method are used to provide the range of void content for any new image of the fabric.

5.3 Results

5.3.1 Results of the manifold embedding method

The results of manifold embedding of 450 images and matrices of varying α (1, 2, and 4) and MI (0, 0,3, and 0,5) are obtained and presented in Figure 5.7 and Figure 5.8.

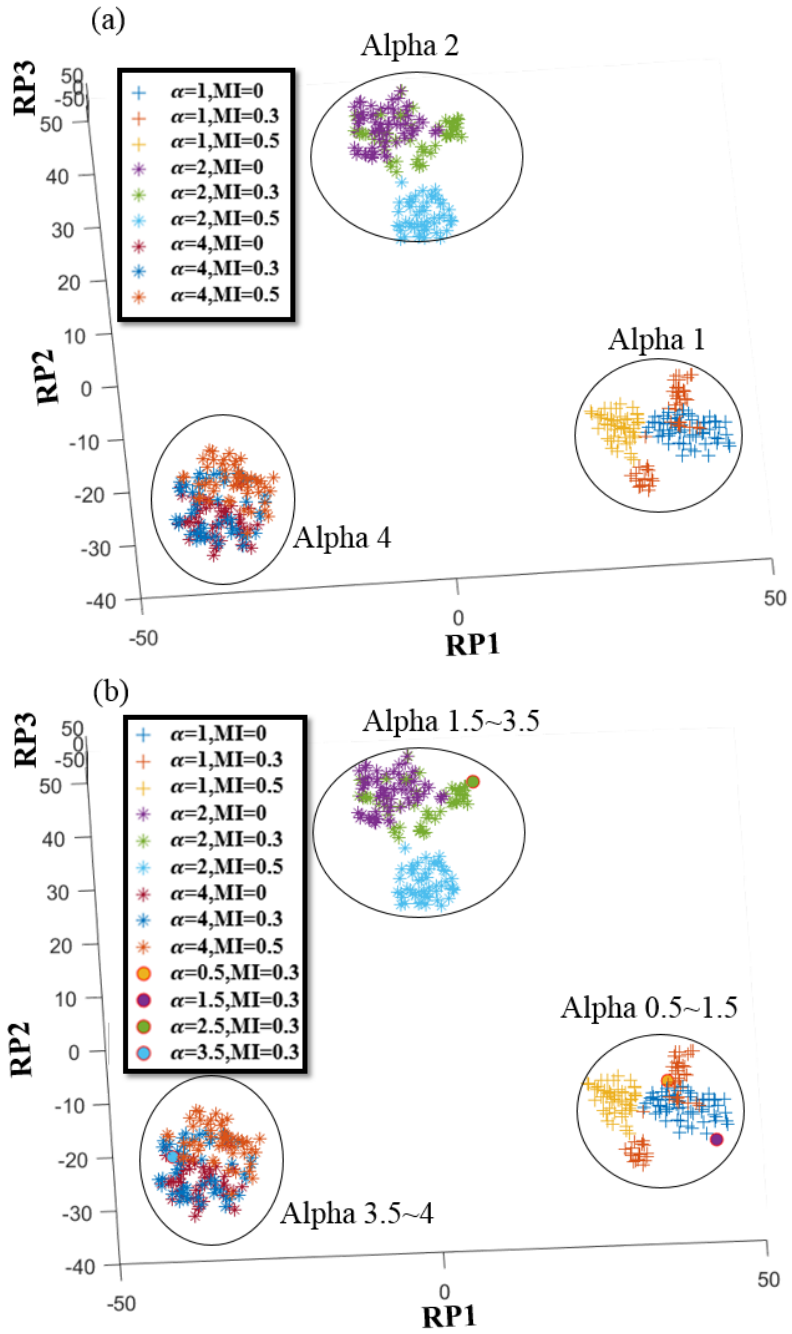

Figure 5.7 Manifold embedding of images of fabric of 205 x 205 size in 3D space. A separation of input data with value of 1, 2 and 4 (a) and A separation of input data with value varying in range (0.5~4) (b). Here RP means reduced parameter

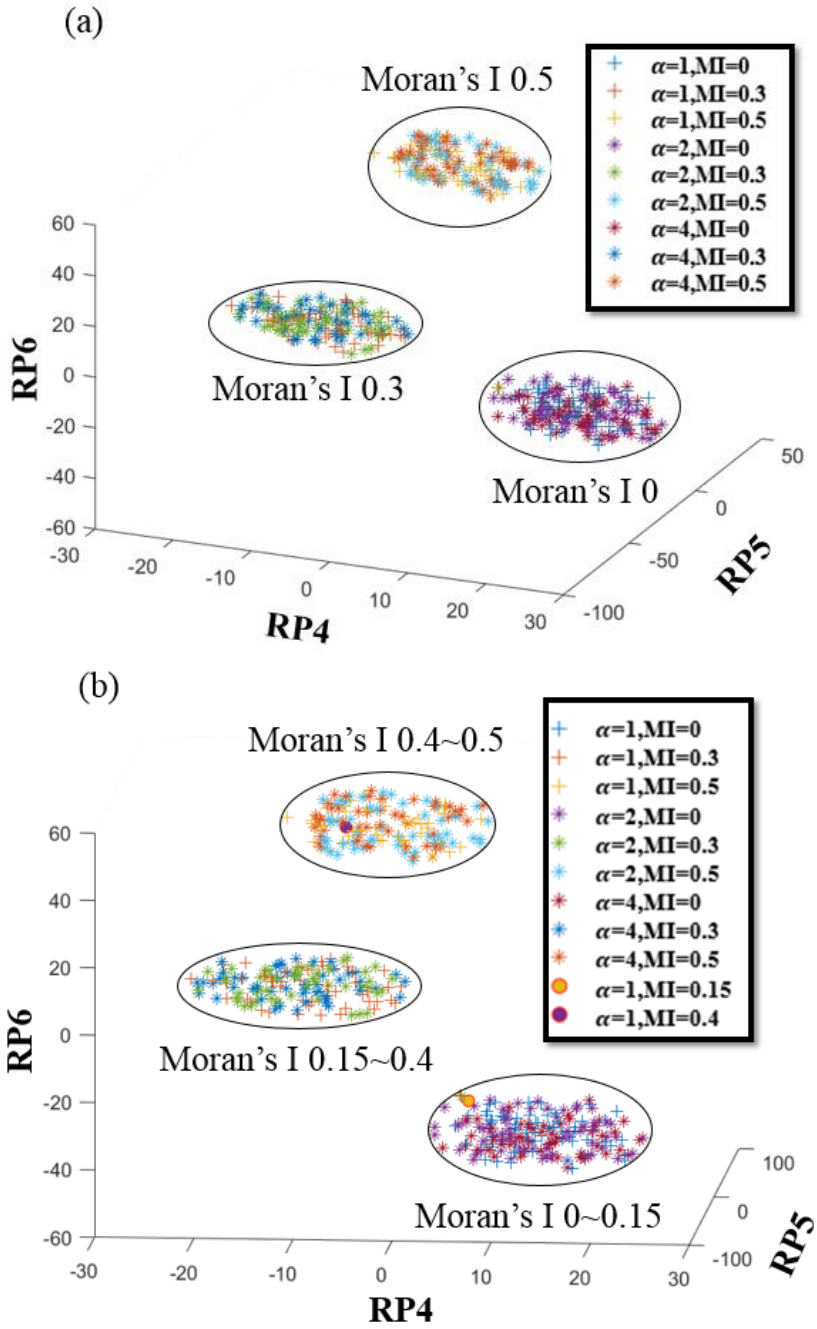

Figure 5.8 Manifold embedding of input matrix of 21 x 21 size in 3D space. MI separation of value of 0, 0.3, and 0.5 (a) and MI separation of value varying in range (0~0.5) (b). Here RP means reduced parameter

A 3D map of clearly separated clusters based on α was obtained using binary images of resolution 205 x 205 pixels in the training step as can be seen in Figure 5.7. As briefly mentioned in Introduction section, α affects the size of pinholes. The higher the value of α, it signifies on an average a larger size pinhole. Considering this, the result makes sense that images rather than matrices are proper training samples for the characterization of input data with α in a reduced 3D space because the images show the size of pinholes. On the other hand, the second type of input data, matrices of 21 x 21 elements, only contains the information of the location of pinholes in a unit size of fabric (105mm by 105mm) and of spatial correlation between pinholes and no pinhole areas. Therefore, matrices rather than images are chosen to be the training samples for characterization of data based on MI values and the results are presented inFigure 5.8. Additional samples of intermediate α of 0.5, 1.5, 2.5, and 3.5 were included in the training pool along with samples of MI of 0.15 and 0.4. Figure 5.7(a) and Figure 5.8(a) show the result from manifold learning process with 9 samples (MI 0, 0.3 and 0.5. α of 1, 2, and 4). Figure 5.7 (b) and Figure 5.8 (b) show the results with all samples including the intermediate values of α and MI. α is set to 1 for samples with varying MI, and MI is set to 0.3 for samples with varying α. These 3D maps can now be used to identify α and MI for a fabric of interest from its image as shown in the next section.

5.3.2 Experimental results

The plain woven fabric presented in Figure 5.1 was used as an input sample to identify its α and MI value using the method discussed in the previous section. The original image of size of 105mm x 105 mm, binary image (205 x 205 pixels), and pinhole matrix (21 x 21 pixels) are displayed inFigure 5.9.

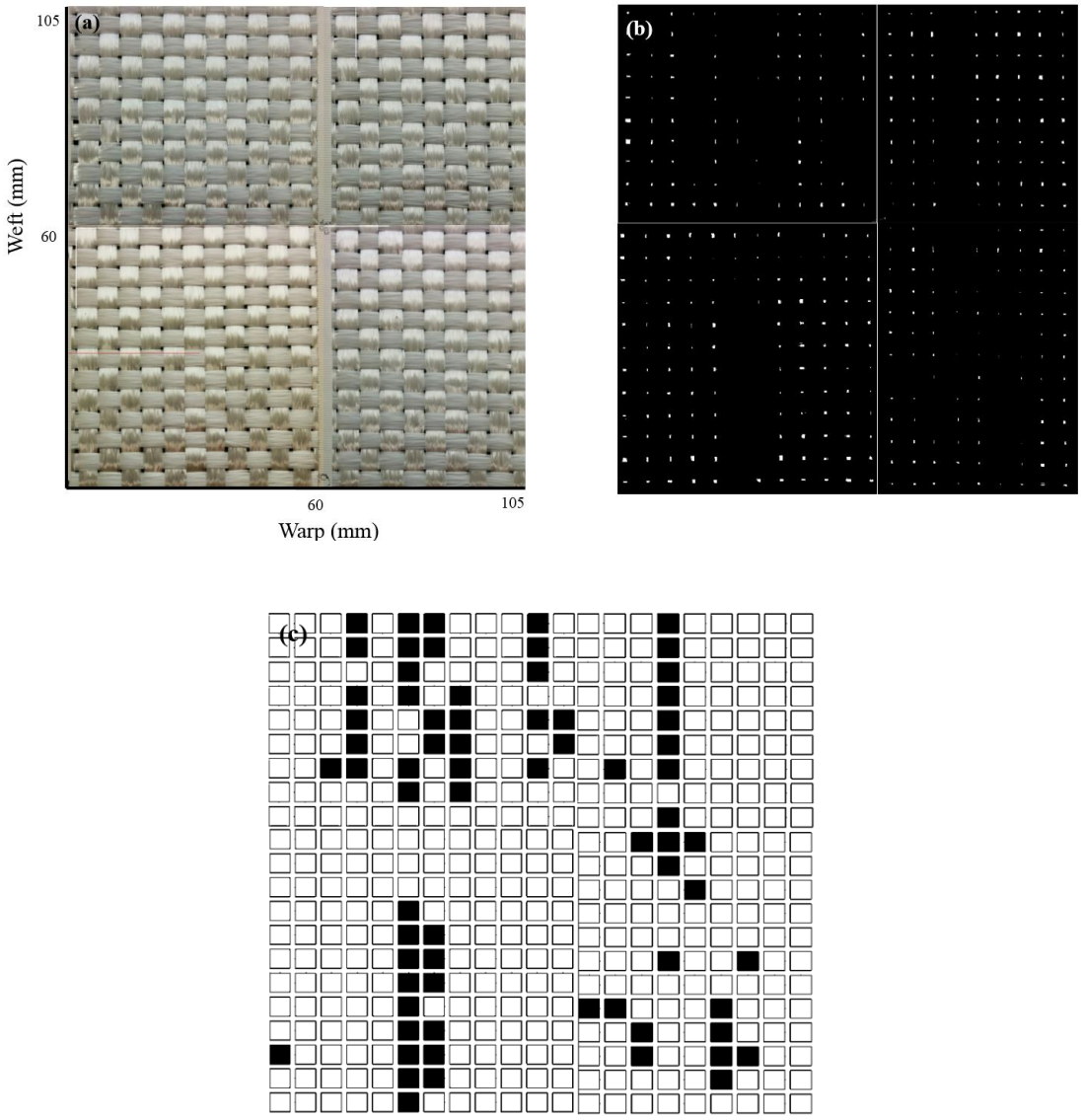

Figure 5.9 Plain woven fabric of size of 105mm x 105mm. the width of tow is 5mm. original image (a) binary image (b) pinhole matrix (c). Black indicates no pinhole area and white indicates pinhole.

The image and matrix data were processed by FFT first before subjecting it to the manifold embedding method. The position of the new sample in a 3D space is shown to belong to the cluster which has α in the range of 0.5~1.5 and MI in the range 0.15~0.4

inFigure 5.10. With this characterization of the fabric, one can forecast the expected void percentage range from the previously compiled library of numerical simulation results for various α and MI values. For α of 1 and MI of 0.3, the expected void fraction are presented in Table 5.4 and Figure 5.11.

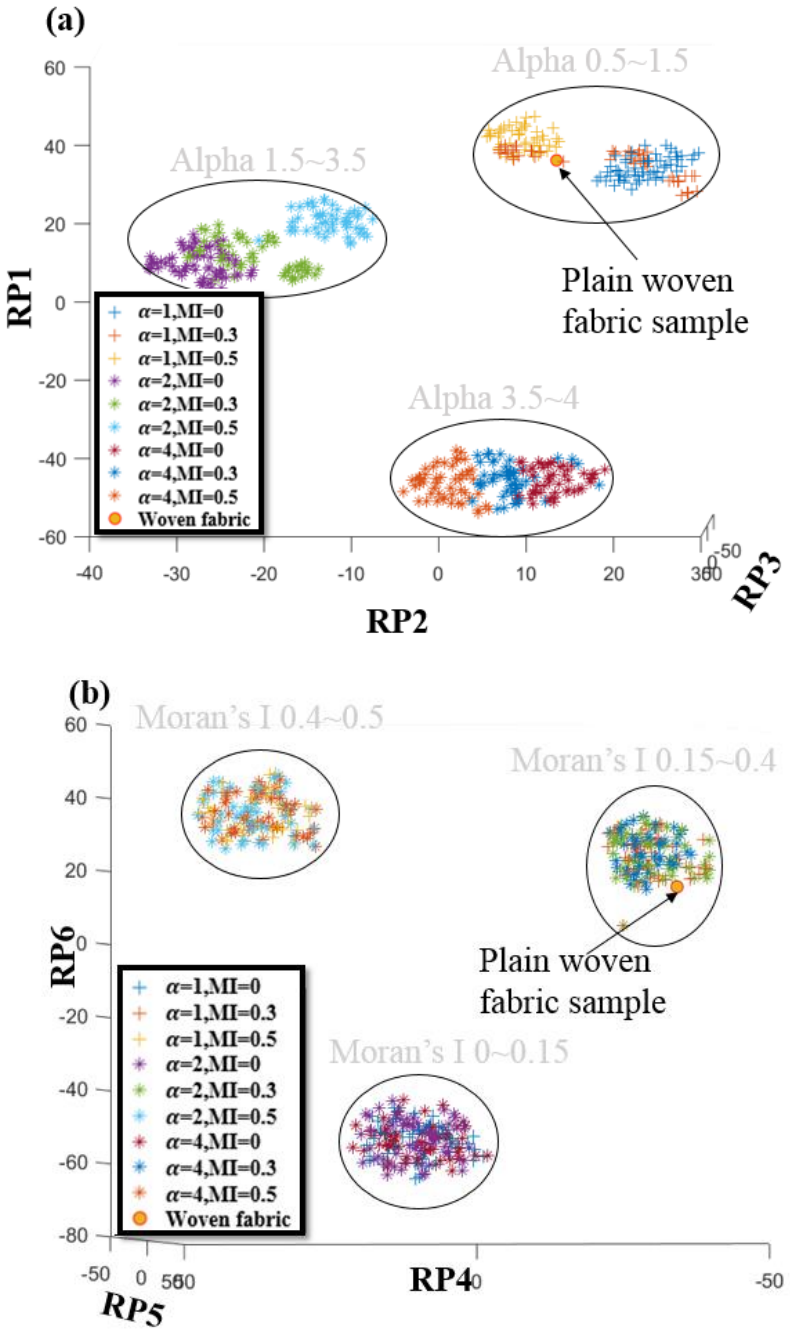

Figure 5.10 Identification of the value of α (a) and MI (b) of the new woven fabric sample in the clustered manifold map built with 450 training samples (see Figure 5.7 and Figure 5.8) Here RP means reduced parameter

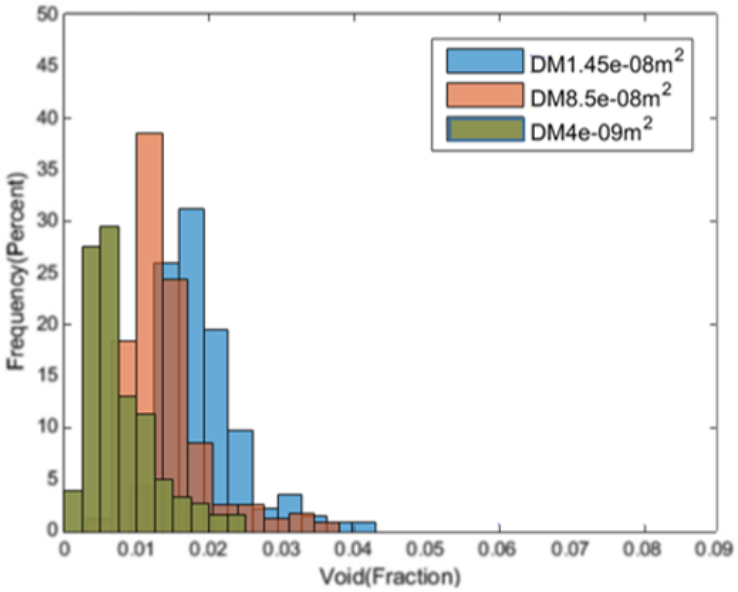

Figure 5.11 Histogram of void percentages calculated from the simulations with generated pinhole fields. Different colors represent different DM permeability magnitudes.

Table 5.4 Void percentage obtained from numerical simulations performed with generated pinhole positions and sizes for various α and MI values

$K_{DM}(m^2)$	Simulation results Void (%)		
	Range (%)	Mean (%)	Standard deviation
1.45×10^{-08}	1.06~4.26	1.90	0.56
8.5×10^{-09}	0.31~3.72	1.39	0.54
4×10^{-09}	0.12~3.33	0.79	0.47

The numerical results show that the void fraction increases with higher DM permeability[30,97] and it could result in up to 4.26% voids for this type of fabric with α of 1 and MI of 0.3.

5.4 Summary and conclusions

Manifold embedding method is successfully used to characterize the architecture of a fabric of interest with important variables such as α and MI. A total of 450 training samples of varying α and MI were used for the manifold embedding method, PCA and t_SNE, to build a 3D map showing distinctly separate clusters of input data separated based on the two variables (α and MI). To test the method, the manifold embedding method was carried out on an image of a new sample of a plain-woven fabric with tow width of 5 mm to identify the cluster of α and MI it belonged to in the 3D map of clusters created from the training samples. The α and MI were found to be in the range of 0.5~1.5 and 1.5~4, respectively for the fabric. The range of void fraction for this fabric was forecasted for the three DM cases to vary between 0.1 to 4%. This quick and efficient approach to characterize a fabric with two variables allows for forecasting the likelihood of void formation and its extend in the VARTM process and also provides textile manufacturers information on the effects of variability in their equipment on the manufacturing of the fabrics so steps could be taken to reduce this variability.

Chapter 6

Prediction of void formation during impregnation of fiber preforms using data mining, decision tree approach

6.1 Introduction

The permeability field can vary locally which leads to an undesirable result such as void formation during the impregnation step of SCRIMP (VARTM with Distribution Media (DM)) process. The variation in the in-plane permeability has been studied to show its effect on resin filling time and the filling pattern[52]. The local variation in through the thickness direction of a fabric due to meso-scale holes (pinholes) has been also studied to show that the local randomness in permeability affects resin flow and results in dry spot (void) formation [88,122]. InChapter 3, the importance of understanding the randomly varying property of pinholes is reported and supported with experimental and numerical studies. Also, the effect of pinholes is observed to be more prominent due to the presence of the DM. The effect of other process or material parameters have not been studied in the presence of pinholes. An open question is how the size, location and distribution of pinholes interact with process or material properties including permeability of DM, K_{DM}, to affect the void formation in the SCRIMP composite manufacturing process. For example, K_{DM} was found to enhance the effect of pinholes by directing flow in through the thickness direction. There are other important properties to consider other than K_{DM} such as in-plane permeability of preform and vent pressure that could affect the void formation. The goal of this chapter

is to investigate how the void formation is effected by the varying material and process variables listed below

1 Fabric architecture variation in terms of pinholes which is characterized by two independent parameters (α and Moran's I (MI)), which will be discussed later

2. Permeability of Distribution Media, K_{DM},

3. In-plane Permeability of the fabric

4. Vent Pressure

by carrying out a numerical parametric study. These data can be used to build a comprehensive library of numerical simulation results of possible scenarios. This information can be classified and analyzed using a decision tree which allows for the visual inspection of the effect of the above parameters and efficient classification of data[99,101,123,124]. A decision tree trained with the library of numerical simulation results can be used to categorize void information efficiently for various combination of the selected parameters.

In this study, we first examine and justify important experimental parameters which directly affect void formation in the SCRIMP process. The verification is done by carefully studying numerical simulation results run with varying values of the identified parameters. Monte Carlo numerical simulations are carried out with the verified parameters varying in values. Regression decision tree model is applied to classify the numerical results (data), which allows ones to forecast void formation behavior in the future.

6.2 Methodology

Process and material parameters which affect void formation are identified numerically using 3D flow simulations. Once the parameters to study are verified, Monte Carlo numerical simulations of resin impregnation into the mold are carried out. A decision tree is trained with the numerical results. To build a decision tree, key attributes and target (decision tree outcome) should be defined. In this study, the material and process parameters are called key attributes and the target is rejection percentage obtained by calculating both the void fraction and the size of the voids.

6.2.1 Numerical simulation

Liquid Injection Molding Simulation (LIMS) is used to advance the flow front in an anisotropic porous media represented by the fibrous reinforcement. Plain woven fabric is used as the fibrous reinforcement sample. The fibrous reinforcement is modeled as a 3D mesh, DM as a 2D mesh, and pinholes as a 1D mesh. The 3D mesh represents the fabric layers which are 0.12m wide and 0.53m long with thickness of 0.7mm under vacuum (fully nested). 2D mesh represents the DM which is 0.11m wide and 0.48m long with thickness of 1mm. The 1D elements along the thickness direction of the fabric represent the pinholes. The permeability tensor of the fabric is experimentally determined using the methodology in chapter 2 and presented in Table 6.1.

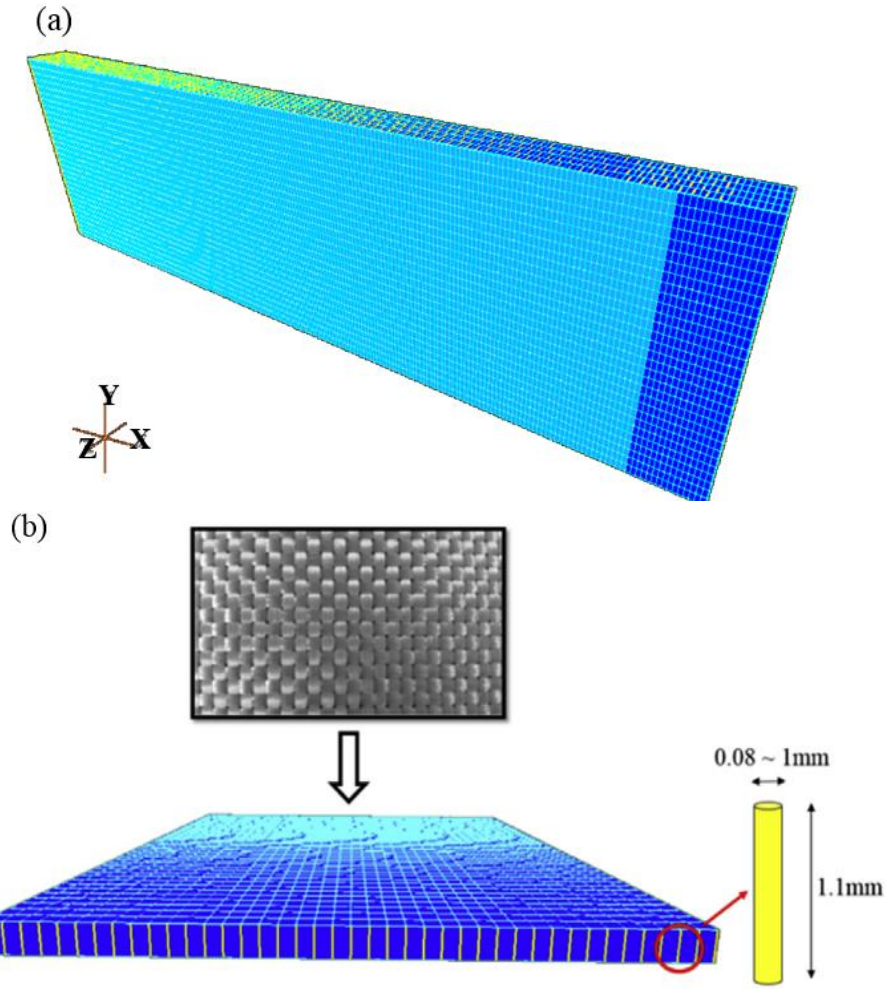

Figure 6.1 (a) Mesh used for flow simulation (b) 3D mesh (blue) with 1D element (yellow)

Table 6.1 Permeability of the plain woven fabric

$K_{xx}(m^2)$	$K_{yy}(m^2)$	$K_{zz}(m^2)$	$K_{xy}(m^2)$	$K_{xz}(m^2)$	$K_{yz}(m^2)$
8.86×10^{-11}	9.10×10^{-11}	1.36×10^{-12}	9.89×10^{-16}	1.58×10^{-15}	1.00×10^{-15}

The pinhole field is generated for each simulation run with the method described in chapter 4. Other experimental conditions such as viscosity, volume fraction, and inlet pressure are presented in Table 6.2.

Table 6.2 Experimental condition for numerical simulation study

Fabric volume fraction	0.45
Inlet pressure (Pa)	1×10^5
Viscosity(Pa.s)	0.1

6.2.2 Key attributes (parameters)

6.2.2.1 Pinhole property (α and MI)

The fabric architecture has pinholes between the fiber tows as they cross each other. These pinholes will vary in size and location as it is a function of the fabric manufacturing process. Thus the heterogeneous through the thickness permeability induced by pinholes of a woven fabric can be characterized with two key variables, gamma distribution variable (α) and Moran's I (MI) as described in chapters 4 and 5. The permeability of the pinholes, K_{pin}, is calculated from the size of the pinholes and one can characterize a histogram from their varying values. α is a shape factor of the gamma distribution which best fits the K_{pin} histogram. The overall K_{pin} value increases with higher α. This means that the influence of the pinhole on the resin flow is stronger as this shape factor increases as more resin flows through the pinholes. Three values of α (1, 2, and 4) are used for this study. The range of α (1-4) should cover most of the woven fabrics. As α increases from 1 to 4 increases, the mean radius of pinhole increases from 0.7 mm to .1.7 mm. One will rarely encounter a woven fabric with pinhole size between two tows to be larger than 1.7 mm. The gamma distributions of varying α values λ of 1.16 are presented in Figure 6.2.The value of λ is obtained experimentally by characterizing the pinhole sizes from a plain woven fabric. ($\alpha = 1 \; and \; \lambda = 1.16$ was experimentally characterized using Equation 4.8)

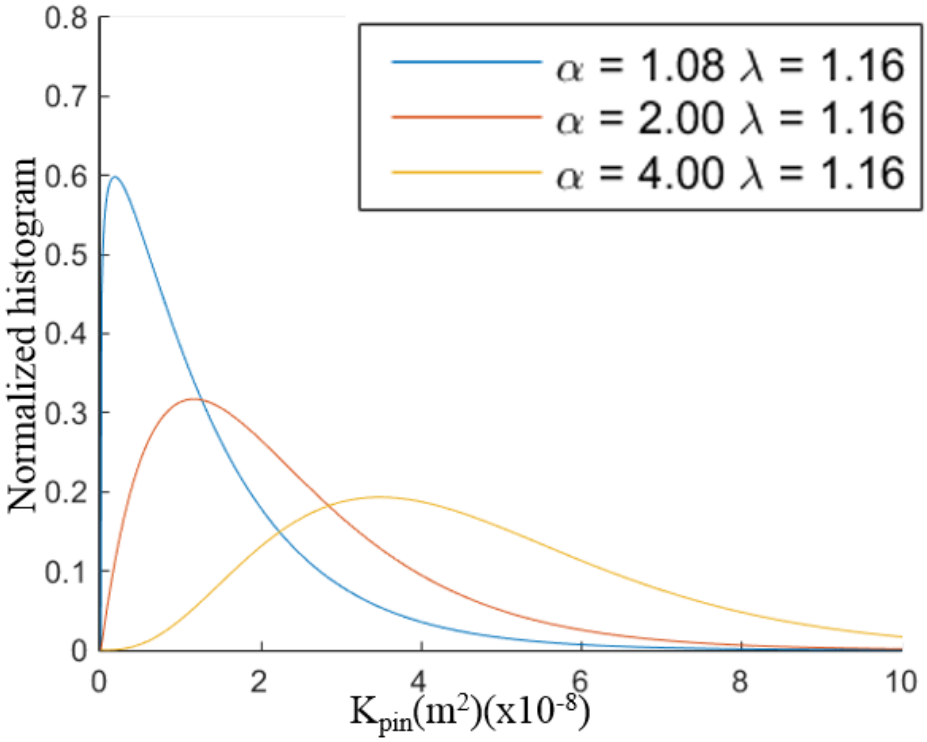

Figure 6.2 Gamma distributions with varying alpha from 1 to 4

MI is a measure of spatial correlation between pinholes. This value varies from -1 to 1 depending on how positively or negatively data (pinholes) are correlated. No spatial correlation (completely random) means MI of 0. This spatial correlation of pinholes is one of the crucial parameters affecting the resin flow, and hence the void formation. MI, for this study, varies from 0 to 0.5, a total of three values of 0, 0.3, and 0.5 were selected to cover the possible range. For MI, one is hardly likely to encounter a woven fabric of MI over 0.5 where large regions of pinholes are correlated as can be seen in Figure 6.3(c). In the 21x21 size mesh in Figure 6.3, black squares represent pinholes and white areas where the tows are touching each other and there are no pinholes. From left to right, the value of MI increases which is visually presented as completely random relation to positively correlated pinholes (black areas).

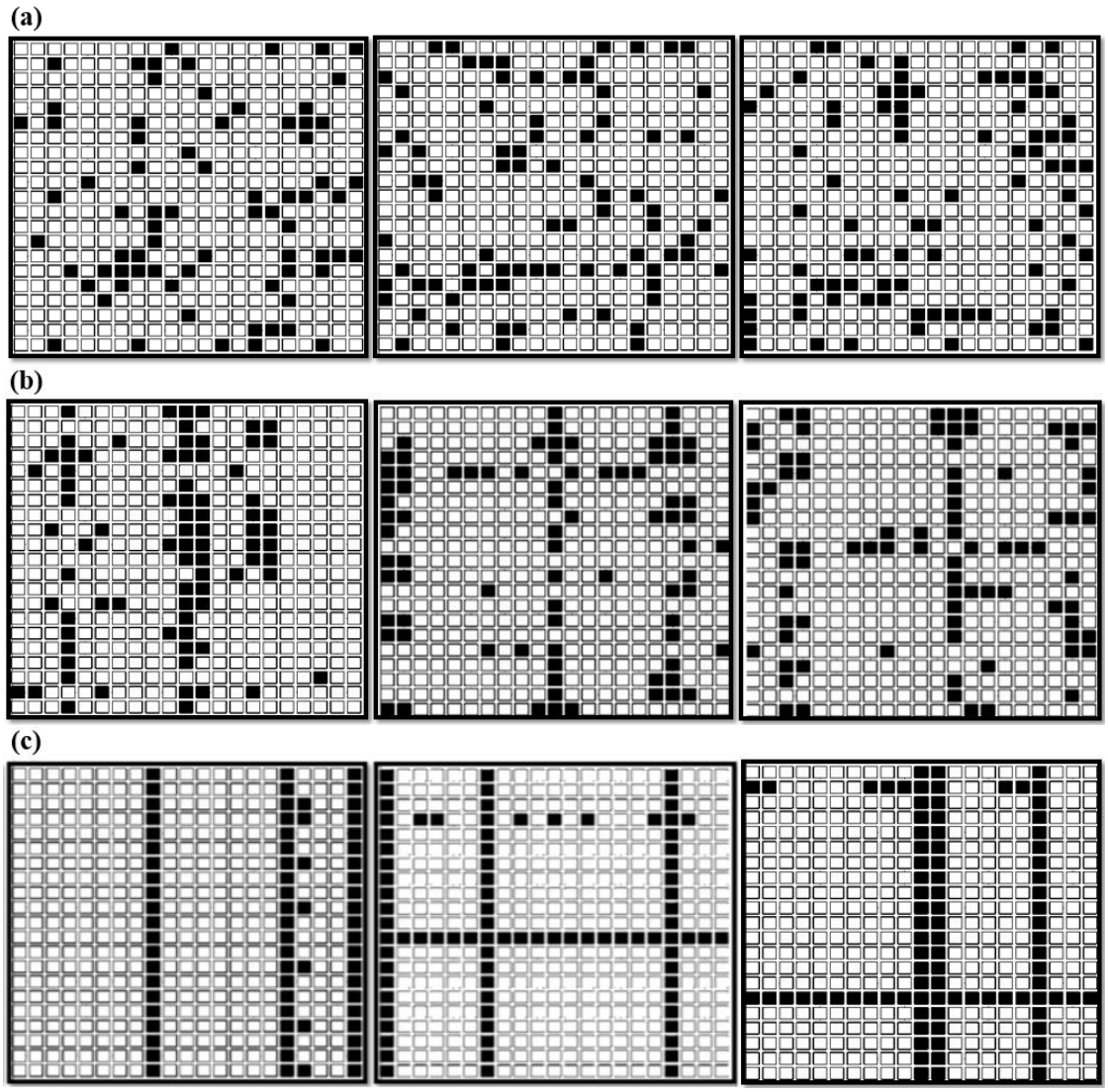

Figure 6.3 Samples of 21x21 mesh size and varying Moran's I. MI of 0 (a), 0.3 (b), and 0.5 (c) Black indicates no pinhole area and white means pinhole area. Many such pinhole location distributions can be generated for each value of MI, allowing one to conduct Monto Carlo simulations for each parameter. Here only three distributions for each MI are shown

6.2.2.2 K_{DM} (DM Permeability)

K_{DM} is an important factor that affects the main direction of resin flow in a SCRIMP process. Resin tends to flow more in the in-plane direction with lower K_{DM}, on the other hand, the flow is directed more through the thickness direction with higher K_{DM}. This more flow in through the thickness direction has more propensity to form voids (air entrapment) because permeability values in the thickness direction are highly heterogeneous. K_{DM} values selected for the parametric study are 4×10^{-9}, 8×10^{-9} and 1.45×10^{-8} m^2. These values of K_{DM} were measured from the distribution media that were available. Also, they do cover a good range of DM values used in a SCRIMP process. The development of resin flow with DM of varying K_{DM} is depicted in Figure 6.4. A total of 4 layers of woven fibrous preforms are used and the images show the bottom layer. Resin flows in the direction of the arrow shown in Figure 6.4. Red dotted line is the flow front along the top layer in contact with the DM. Figure 6.4 shows increasing value of DM from left to right. The flow along the bottom layer shows more disturbed outline of flow fronts and enclosed spaces indicating that there will be voids formed because as K_{DM} value increases it results in more non-uniform flow front. The lead length between flow fronts along bottom and top layer also increases as DM permeability value increases. It clearly shows the influence of K_{DM} on flow front and void formation behavior that higher the value of K_{DM}, higher is the possibility for void formation due to the irregularity in the flow fronts.

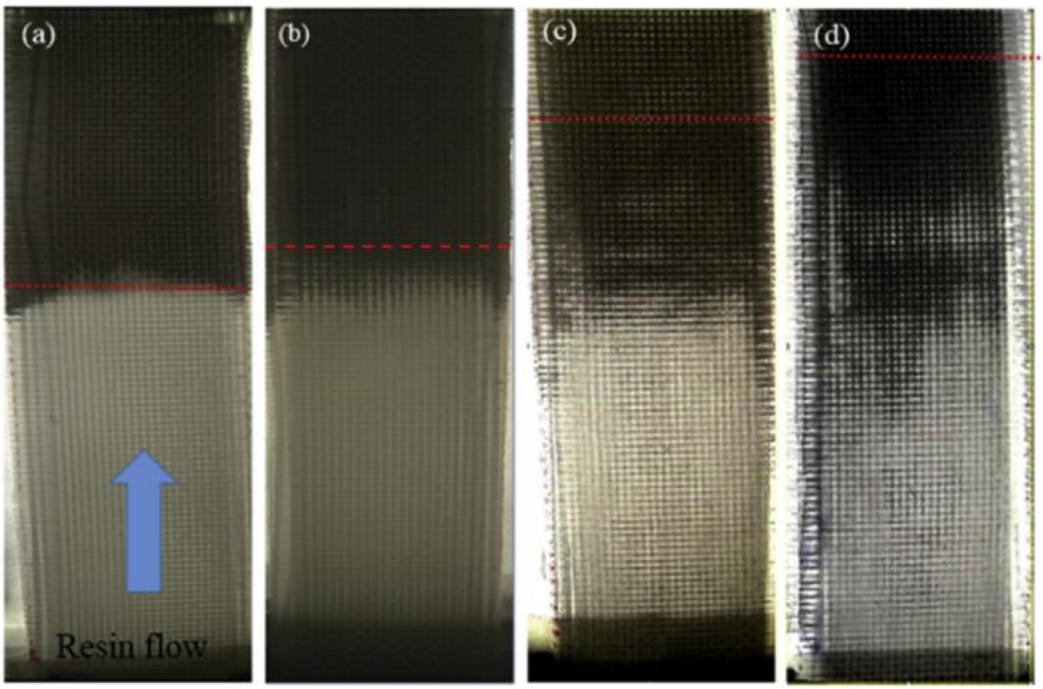

Figure 6.4 Experimental image of the bottom layer when the flow front reached 30 cm from the inlet gate during resin flow in a SCRIMP process. Red dotted line represents the position of flow along the top layer with (a) No DM (b) K_{DM} = 4e-09 m^2 (c) K_{DM} = 8.5e-09 m^2 (d) K_{DM} = 1.45e-08 m^2

6.2.2.3 Ratio of Inplane to through the thickness permeability ($K_{xx}(K_{yy})/K_{zz}$)

The effect of the ratio of in-plane permeability (Kxx and Kyy) to through the thickness permeability (Kzz) on the void formation is also explored. The ratio can affect the resin flow and void formation, because when this ratio increases more flow takes place in the in in-plane direction. This is very important because the permeability field in the in-plane direction does not have the heterogeneity to the extent in through the thickness direction. Typically, the ratio of inplane to through the thickness direction is around 2 order of magnitude (~100) for a woven glass fabric. For this study, varying higher ratios are adopted to investigate the effect of increasing ratio on the void

formation. The ratio of Kxx/Kzz varies from 100 (typical) to 500 (100,300, and 500). For simplicity, it is assumed that the fabric is isotropic (Kxx=Kyy).

6.2.2.4 Vent pressure

In VARTM process, a full vacuum is an ideal pressure condition. However it's possible to have a partial positive pressure at the vent for various reasons such as mechanical difficulty regardless of the period of the fibrous materials under vacuum. Although the vent pressure does not alter the flow pattern of resin or redirect it in certain direction, it does affect the final size of voids. Higher vent pressure means lower pressure difference driving the resin flow which results in overall slower flow and bigger size of trapped air (voids). In this study, the vent pressure is varied from 2% of injection pressure (10^5Pa) to 8% of injection pressure (total 2%,5%, and 8%).

6.2.3 Target

The target for the decision tree is the rejection percentage varying from 0~ 100%. A total of 150 numerical simulations are carried out for each combination of the mentioned 5 parameters. The number of total numerical simulations for each case (150) is determined by studying the mean of void fraction with increasing run numbers. It was found that 150 is large enough for the mean value to reach a plateau. The detailed explanation is presented in chapter 4.2.7. Void fraction and size of voids from each simulation out of 150 cases is examined to see if is the part should be rejected. In this study, a part is rejected if the void fraction is over 3.5% or if the diameter of the void is higher than 1.5cm. The rejection percentage is obtained by dividing a number of

rejected cases by the total number of cases (150). The selection of the size of the largest void in the composite and the percentage of void fraction will depend on the application and what knock down factor one can tolerate in that application. For example, for aerospace parts the largest void fraction that can be tolerated is 2% whereas in non-structural automotive parts or wind blades this fraction could be as high as 5%. For the sake of this study we decided on 3.5%. A single void that is very large in size even if the overall void fraction may be low is the weakest link in the composite failure and that has been selected here as 1.5 cm which is about a few thicknesses of the composite. Again this number could be reduced or increased based on the application. Our goal here is to demonstrate the methodology with some plausible values for the void fraction and void size.

6.2.3.1 Void fraction

Void regions found from the simulation runs are numerically characterized by calculating its void fraction. The void fraction is obtained by dividing the total area of voids found on the bottom layer by the entire area of the fabric because most of void regions are found to be formed in the bottom layer in this VARTM process.

6.2.3.2 Size of voids

Size of voids is also important information in addition to total void fraction in a part. It is because a part could have a low total void fraction with a few large voids which are more detrimental to the mechanical strength of a composite part than having a large number of small size of voids which add up to a higher void fraction. That is, total

void fraction alone is not sufficient information about voids. The locations of voids in the bottom layer are obtained from the numerical simulation and the example of void distribution in a form of binary image is presented in Figure 6.5 (a) and (b) which shows the scatter plot of the binary image with voids (blue circles). Once the image and plots are obtained, the next step is to group adjacent voids (blue circles) to determine the size of voids. Cluster analysis is, carried out using a dendrogram which shows the distance between points. Voids within certain threshold distance of each other (in this case 0.7cm) are grouped together as one void. The distance of 0.7cm is diagonal distance of 0.5cm which is the distance between two adjacent pinholes.

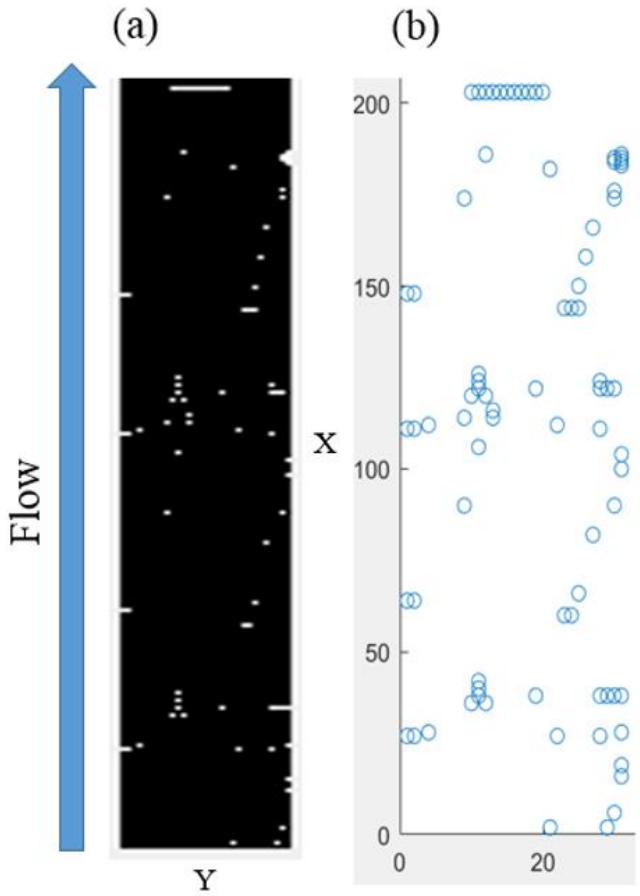

Figure 6.5 (a) Binary image of voids formed (white spots) in a bottom layer (b) Scatter plot of the binary matrix with voids (blue circles)

6.2.4 Decision tree

Decision tree is a data classification tool to place data in sub-categories depending on how the data is defined at each node. A decision tree consists of root (top) node, split node, and leaf (terminal) node as can be seen in Figure 6.6 which are organized with a test function at each node[124,125].

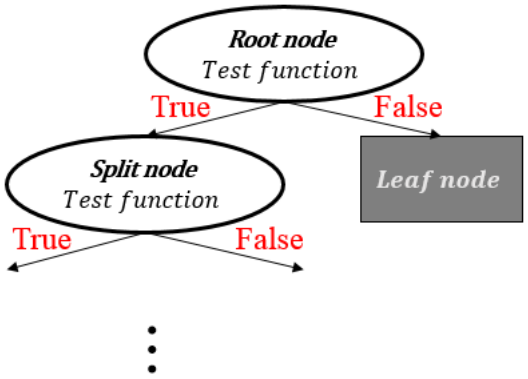

Figure 6.6 The structure of a decision tree

The test function contains a binary question of if the incoming data is bigger or smaller than a value of an attribute. The test functions at each node are selected in a way to optimize the decision tree. How test functions are determined is explained with the help of eleven example cases to illustrate the decision tree optimization process. This step shows how to determine which attribute to use for a test function. The examples used for this are presented in Table 6.3. First, the standard deviation (S0) of all of target values (rejection percentage) are calculated to be 18.2. Next, the standard deviation of the targets with each attribute (S(T,X)) is obtained as shown in Equation 6.1. S(T,X) is standard deviation of target values for a specific attribute (X). The example to calculate S(T,X) is presented in Table 6.4 and Equation 6.2.

Table 6.3 Target values from eleven examples combining various key attributes

Example	α	MI	K_{DM}(m2)	K_{xx}(K_{yy}) /K_{zz}	Vent Pressure/ Injection Pressure	Target (Rejection percentage)
E1	1	0	1.4×10^{-8}	100	0.05	0.94
E2	1	0.3	1.4×10^{-8}	100	0.05	12
E3	1	0.5	1.4×10^{-8}	100	0.05	14
E4	2	0.3	1.4×10^{-8}	100	0.05	26
E5	4	0.3	1.4×10^{-8}	100	0.05	48
E6	1	0.3	8.5×10^{-9}	100	0.05	2
E7	1	0.3	4.0×10^{-9}	100	0.05	0
E8	1	0.3	1.4×10^{-8}	300	0.05	5
E9	1	0.3	1.4×10^{-8}	500	0.05	3
E10	1	0.3	1.4×10^{-8}	100	0.02	5
E11	1	0.3	1.4×10^{-8}	100	0.08	49

$$S(T,X) = \sum_{c \in X} P(c)S(c) \tag{6.1}$$

Where c is each value of the attribute, X is an attribute, P(c) is a probability for the X attribute to have a value c, and S(c) is standard deviation of the targets with respect to the attribute X with a value c. An example to calculate S(T,X) when X is the attribute α is presented in Table 6.4. The count refers to the number of cases with that value of the attribute from the total of 11 cases presented in Table 6.3

Table 6.4 Example to calculate Standard deviation of rejection percentage (target) and count with the attribute (X) which is α for this case

Attribute (X)	Value (c)	Standard deviation of target (S(c))	Count
α	1	15.3	9
	2	0	1
	4	0	1
			11

$$S(T,\alpha) = \sum_{c\in\alpha} P(c)S(c) = \frac{9}{11}15.3 + \frac{1}{11}0 + \frac{1}{11}0 = 12.51 \quad (6.2)$$

The attribute to form the test function at the split nodes is determined by choosing the most homogeneous one that gives the highest difference between S0 (the standard deviation of all target values)and S(T,X). S0 for the 11 cases presented in Table 6.3 was calculated to be 18.2. Next the standard deviation for the 11 cases calculated for each attribute using equation 6.1 were as follows :S(T,α) is 12.5, S(T,MI) is 16.1, S(T, K_{DM}) is 15.4, S(T, $K_{xx}(K_{yy})/K_{zz}$) is 15.9, and S(T, vent pressure) is 12.4. The vent pressure is furtherest away from the total standard deviation and hence is chosen to form the first test function in the decision tree.

6.3 Results

6.3.1 Numerical simulation

A total of 243 case studies ($3\alpha \times 3MI \times 3K_{DM} \times 3K_{xx}/K_{zz} \times 3$vent pressure$= 3^5$) which means a total of (243 x 150 (for each set of parameters)) 36450 simulations were carried out. Void fraction and rejection percentage for each of the three values of the key attributes are calculated. The base value chosen for the attributes α is 1,for MI is

0.3, for K_{DM} is 1.4e-08 m^2, for K_{xx}/K_{zz} ratio is 100, and for vent pressure is 0.05×10^5pa.

6.3.1.1 Pinhole property (α and MI)

The effect of pinhole property on void fraction is presented in Table 6.5. As α and MI increase, the void fraction also increases. For α value from 1 to 4, void fraction gradually increases from 1.35 to 2.54. Mean void fraction increases from 1.35 to 2.05 when MI is increased from 0 to 0.5. AS α and MI increase, the rejection rate increases from 0.94 to 48 percent. The trend of void fraction and rejection percentage is more apparent with the parameter of α than MI. This means that the size of pinholes is more influential parameter on void formation than how the pinholes are spatially correlated. The increase in void fraction with increasing α and MI agree with the expectation that the increase in size of pinholes due to α and in spatial correlation introduces higher randomness in through the thickness direction.

Table 6.5 Range, mean, and standard deviation of void fraction and rejection percentage

	α= 1 MI= 0	α= 1 MI= 0.3	α= 1 MI= 0.5	α= 2 MI=0.3	α= 4 MI= 0.3
Range (%)	0.7~2.6	0.9~3.8	0.9~4.6	1.3~4.2	1.3~4.3
Mean (%)	1.35	1.90	2.05	2.30	2.54
Standard deviation (%)	0.37	0.65	0.75	0.47	0.50
Rejection percentage (%)	0.94	12	14	26	48

6.3.1.2 K_{DM}

K_{DM} also plays an important part in resin flow which can lead to void formation as can be seen in Table 6.6. For the range of 4×10^{-9} to 1.4×10^{-8}m^2 of K_{DM}, mean void fraction increases from 0.79 to 1.9. Rejection percentage also increases from 0 to 12 as K_{DM} increases. This result agrees with the prediction that more flow is directed in through the thickness direction with higher K_{DM} which results in higher void fraction and rejection percentage.

Table 6.6 Void fraction and reject percentage with varying K_{DM}

K_{DM}(m^2)	Range (%)	Mean (%)	Standard deviation	Rejection percentage (%)
1.45×10^{-08}	1.06~4.26	1.90	0.56	12
8.5×10^{-09}	0.31~3.72	1.39	0.54	2
4×10^{-09}	0.12~3.33	0.79	0.47	0

6.3.1.3 $K_{xx}(K_{yy})/K_{zz}$

Void fraction decreases with higher ratio of K_{xx}/K_{zz}. This trend is presented in Table 6.7. As the ratio increases from 100 to 500, the detected void percentage decreases from 1.86 to 1.30. Rejection percentage decreases from 12 to 3% with increasing ratio. There is a big difference in void fraction between the ratio of 100 and 300. There is a negligent difference between the ratio of 300 and 500. As the ratio increases, more resin is directed in the in-plane direction where there is no randomness or variability in permeability. This results in more uniform flow and less void formation.

Table 6.7 Void percentage and rejection percentage with varying K_{xx} (K_{yy})/K_{zz}

$K_{xx}(K_{yy})/K_{zz}(m^2)$	Range (%)	Mean (%)	Standard deviation	Rejection percentage (%)
100	0.82~4.37	1.86	0.67	12
300	0.37~3.41	1.36	0.68	5
500	0.14~3.81	1.30	0.93	3

6.3.1.4 Vent pressure

Mean of void fraction and rejection percentage both increase as the vent pressure was increased from 2×10^5pa to 8×10^5. Void fraction increases from 1.34 to 2.33 and rejection percentage increases from 5 to 49. As predicted above, higher vent pressure results in higher size of voids and void fraction which lead to higher rejection percentage because pressure in entrapped air is higher and so the volume is larger.

Table 6.8 Void fraction and rejection percentage with varying vent pressure

Vent Pressure (Pa)	Range (%)	Mean (%)	Standard deviation	Rejection Percentage (%)
2×10^5	0.35~3.57	1.34	0.66	5
5×10^5	0.82~4.37	1.86	0.67	12
8×10^5	1.19~1.01	2.33	0.55	49

6.3.2 Decision tree

Decision tree is built with resulting data from the numerical simulations. An example of decision tree trained with the 11 examples in Table 6.9 is presented in Figure 6.7 and Figure 6.8. In Figure 6.8, R(%) means rejection percentage. The 11 examples in Table 6.3 are the combination of each attribute study (Chapter 6.3.1). The three values investigated in this study with the attribute α are shown with cases E2,E4, and E5 in Table 6.3. The three MI values investigated are presented with cases E1-E3. The three

K_{DM} values are presented with cases of E2, E6, and E7 in Table 6.3. Three values of K_{xx}/K_{zz} are examined in E2, E8, and E9. Vent pressure changes are represented by E2, E10, and E11.

Table 6.9 11 examples cases using 5 identified attributed used to build a decision tree as a function of two targets: mean void fraction and rejection percentage

Example	α	MI	K_{DM}(m2)	$K_{xx}(K_{yy})/K_{zz}$	Vent Pressure/ Injection Pressure	Target (Mean Void fraction)	Target (Rejection percentage)
E1	1	0	1.4×10^{-8}	100	0.05	1.35	0.94
E2	1	0.3	1.4×10^{-8}	100	0.05	1.86	12
E3	1	0.5	1.4×10^{-8}	100	0.05	2.05	14
E4	2	0.3	1.4×10^{-8}	100	0.05	2.30	26
E5	4	0.3	1.4×10^{-8}	100	0.05	2.54	48
E6	1	0.3	8.5×10^{-9}	100	0.05	1.39	2
E7	1	0.3	4.0×10^{-9}	100	0.05	0.79	0
E8	1	0.3	1.4×10^{-8}	300	0.05	1.36	5
E9	1	0.3	1.4×10^{-8}	500	0.05	1.26	3
E10	1	0.3	1.4×10^{-8}	100	0.02	1.34	5
E11	1	0.3	1.4×10^{-8}	100	0.08	2.33	49

Here the mean void fraction is the average of void fraction from 150 simulations conducted for the selected five attributes where as rejection percentage is the percent of rejected parts from 150 simulations based on the size of the void (in our case greater than 1.5 cm in diameter) and/or the void percent for that simulation being greater than a threshold void fraction which in our case was selected to be 3.5%. Among the considered attributes, α seems to be most effective as the rejection percentage reaches almost half (48%) with highest value of α of 4. Vent pressure is also an effective attribute as α the rejection percentage reaches close to half (49%) with the highest vent

pressure. This clearly indicates that it is important to ensure that the pinhole characterization of fabrics have a lower value of alpha and during the process an effective vacuum is maintained to reduce rejection rate and void content.

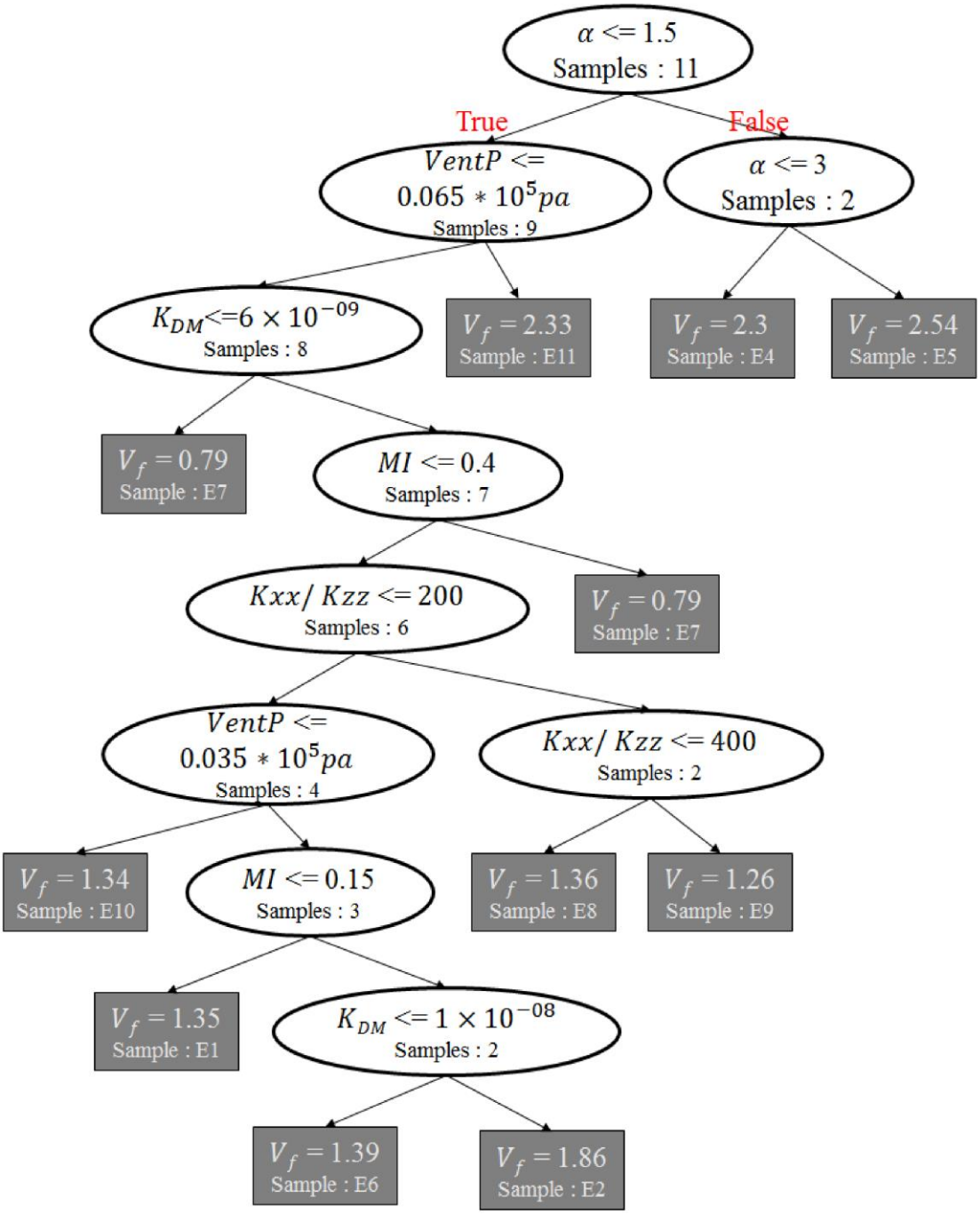

Figure 6.7 Decision tree to visualize the classification of the results of the void fraction from 11 examples in Table 6.9. Circular block presents split nodes with a test function and rectangular block shows final node.

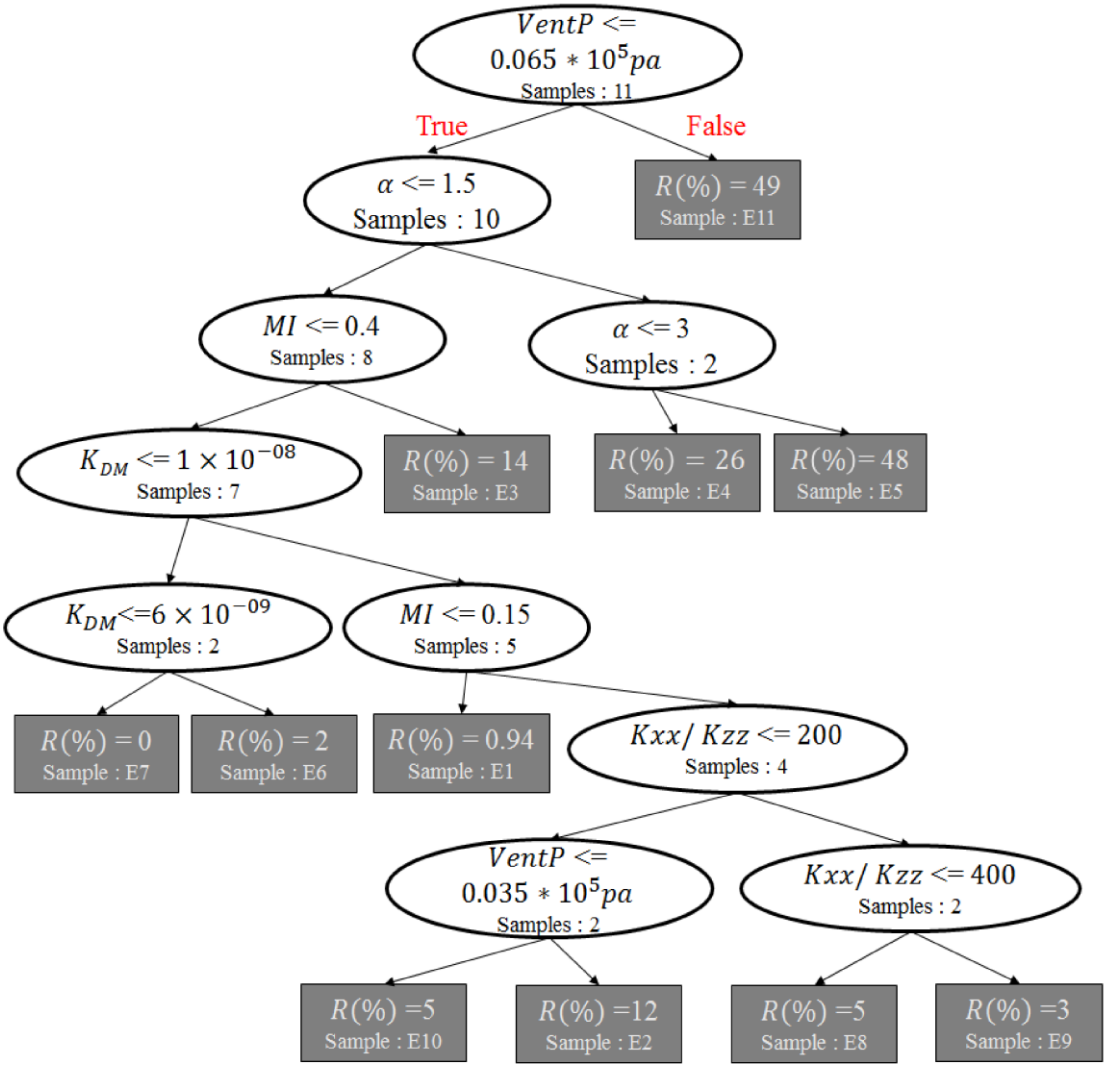

Figure 6.8 Decision tree to visually classify the results based on the target of rejection percentage from the 11 examples in Table 6.9. Circular block presents split nodes with a test function and rectangular block shows final node.

Once the decision tree is obtained in the training step as can be seen in Figure 6.7 and Figure 6.8, a prediction of void fraction (varying from 0.79~2.54) and rejection percentage (0~49) can be made with any combination of attributes in the range. Visual inspection of the tree also helps one to study the effect of each attribute. The visual inspection allows one to understand the effect of each parameter clearly and quickly.

For example, it can be seen in Figure 6.7 that the part will have highest void fraction range (2.33 to 2.54) if α is larger than 3. From Figure 6.8, it can be seen that the the highest rejection rate (48 to 49) is possible in the process if the α that characterizes the fabric is larger than 3 and if in the process the vent pressure is higher than 6.5 percent of the injection pressure (the vacuum pump not being able to maintain adequate vacuum). This quick and efficient analysis of the process and material parameters in terms of void formation with the trained decision tree will provide the manufacturing engineer a good guide for identifying parameters if high rejection rate is encountered in the process.

6.4 Summary

Key attributes which affect the void formation and the rejection rate (targets) in a VARTM process have been identified through a Monte Carlo simulation study with 150 simulations for each combination of the five attributes explored. The range of key attributes considered here are representative of material and process parameters used in such composite manufacturing processes. It was shown that the increase in the value of parameter such as Kxx/Kzz which enhances the flow in the in-plane direction result in lower void fraction and rejection percentage. On the other hand, increasing value in parameters such as K_{DM} ,MI and α lead to higher void fraction and rejection percentage as more resin flows in through the thickness direction. The process variable of vent pressure was also shown to affect the void formation adversely so higher the vent pressure, larger will be the void fraction and rejection percentage clearly showing the importance of ensuring that higher vacuum level is maintained at the vent. The parametric study shows that with the range of values studied, α (which is related to the

pinhole sizes in the fabric) and the vent pressure (maintenance of good vacuum) are most influential parameters.

Decision tree is created with the target data (void fraction and rejection percentage) obtained from numerical simulation study. Using the decision tree is proven to be not only efficient and easy to retrieve the target information but also necessary for visual study and clear understanding of the effect of each parameter on the target.

The parametric study and the application of the decision tree are an example of an efficient methodology to access the valuable information of void formation behavior with varying parameters in a VARTM process. This study allows one to design the process and ensure that the materials such as the fabrics used are well characterized and fall between the limits as forecasted by the decision tree in order to minimize the void and rejection percentage.

Chapter 7

CONCLUSIONS, CONTRIBUTIONS AND FUTURE WORK

7.1 Conclusions

Deterministic simulations of composite manufacturing processes provide guidelines for process design. However, almost all composite manufacturing processes are marred with variability due to material and process variability and nowhere this is more true than in certain class of LCM processes such as SCRIMP and Compression RTM. In such LCM processes, the presence of pinholes varying in size in a preform due to the variability in textile manufacturing introduces local variability in through the thickness permeability which is known to be cause of void formation. Hence the goal is to understand the role of such variability which will guide one towards a robust process design to prevent voids during the manufacturing process despite these unplanned perturbations in permeability. This work has shown that such variations can be addressed by developing methodologies to characterize and model the unplanned variability in the fabric and process using validated 3D numerical simulations as a surrogate for the actual manufacturing process to predict the void formation and expected rejection rate.

First of all, the study of effect of through the thickness skew terms (*Kxz,Kyz*) on the resin flow was carried out, which was followed by a development of methodology to measure these skew terms with other four permeability components (*Kxx,Kyy,Kzz, and Kxy*) from a single experiment. This novel methodology has been verified

experimentally and numerically. This work can characterize the skew terms of a fabric, especially 3D fabrics and studying the effect of its variability on flow.

Next, the local variations (pinholes) in the through the thickness permeability (*Kzz*) are studied and modeled. The permeability of pinholes are experimentally obtained to be used as input in 3D numerical simulations. The numerical simulations are validated with experimental work. The meso-scale pinholes are found to cause void formation by locally affecting the resin flow. The effects grow stronger as DM permeability increases because more resin is directed in through the thickness direction. This methodology of modeling and studying pinholes in numerical simulations will help detect material and process conditions to prevent void formation. Here it was shown that lower DM permeability will reduce the void formation in the presence of pinholes in the fabric.

The pinhole random field which was measured was studied statistically and a methodology was developed to create the random field with two parameters instead of obtaining it experimentally. Gamma distribution which fits the histogram of measured K_{pin} and MI of spatial correlation were found to define the pinhole random field. The random field was then created with gamma distribution parameters (scale factor of λ and shape factor of α) and MI. The created random field of K_{pin} was then used as an input to run Monte Carlo numerical simulations which were compared to experimental results. Numerical results showed a good agreement with experimental results, which validates the methodology to generate the random field. This study presents a novel methodology to create the pinhole random field with two parameters α and MI which helps avoiding the time-consuming task of experimentally acquiring K_{pin} values for a

fabric through hundreds of samples. The value of α and MI can be obtained just from one sample of the fabric

Next, a novel methodology to identify the statistical properties of α and MI which are necessary to create the pinhole random fields was developed. This method allows one to identify these two key parameters from a picture of a fabric sample. The dimensionality reduction methods called PCA and t_SNE were used to process the pictures of a fabric to achieve this goal. The high dimensions (pixels) of a picture were reduced to 3D space for the visual inspection and characterization. In the reduced 3D space, a total of 450 samples varying values of α and MI were plotted to show formation of distinct grouping or clusters for similar value of α and MI values. To validate this methodology, a test sample of a plain woven fabric was identified with α of 1 and MI of 0.3 by locating the cluster this sample belongs to. This study presents a novel methodology to allow one to identify the important parameters of a fabric, α and MI, on-line efficiently. The two parameters can then be used as an input to generate the random fields for Monte Carlo simulations to predict the void sizes and distributions accounting for the variability.

Finally, a parametric study was numerically carried out to study how the pinhole properties (α and MI) interact with other properties (DM permeability, vent pressure, and in-plane permeability of preform) to affect void formation in the process. It was numerically found that increasing in-plane permeability and MI decrease void formation. On the other hand, increasing , DM permeability, and vent pressure increased void formation and rejection rate. This indicates that the variables which enhance resin flow in in-plane direction mitigate the pinholes effect. This study provides a material choice and process window to reduce void formation and rejection

rate. Decision tree method is recommended to classify and sort the data from the numerical parametric study for easy and efficient access to the data.

7.2 Contributions

The unique contributions of this dissertation work are listed below.

1. A novel methodology to measure all six components of permeability tensor was developed and verified numerically and experimentally. Since the bulk permeability tensor is characterized from a single experiment, it saves time and effort to measure the permeability. This method is particularly useful for 3D fabric characterization with significant skewing of flow due to the 3D stitching or weaving which could influence the void formation and distribution.
2. A methodology to characterize stochastically varying permeability into the numerical simulation allows one to quantify the effect of local variability (pinhole) on the robustness of the manufacturing process in terms of void sizes and void distribution. This study also highlights the role of distribution media permeability in characterizing the robustness of the process. Higher distribution media permeability may reduce fill time but is more likely to cause higher percentage of voids.
3. A methodology to create the K_{pin} random fields by identifying two parameters from a fabric sample was developed. This will allow one to save time to obtain the K_{pin} random fields which are used in numerical simulations and access the variability on the void distribution formation by conducting many realizations of this variations. This methodology is particularly useful to model a large area of K_{pin} field for large composites such as wind blade.

4. A novel methodology to identify a woven fabric with the important statistical parameters (α, MI) was developed with a machine learning method called PCA and t_SNE. With this method, a woven fabric can be easily identified on-line with these two parameters from a digital image of a sample of the fabric. Once these parameters are identified, the K_{pin} random fields can be created to be used as an input for Monte Carlo numerical simulations and design the process in the presence of the variability in through the thickness permeability.

5. Lastly, the effect of pinholes along with other process or material properties is studied through comprehensive parametric study which can guide one to choose a reasonable range of values of material properties such as DM permeability or in-plane permeability of preform and process variables such as vacuum pressure to avoid voids in composite parts..

7.3 Future work

Stochastically varying property in through the thickness direction of a fabric can affect resin flow not only in RTM and VARTM (SCRIMP) but also compression RTM (CRTM). In the compression molding, resin is injected in the gap between the preform and the mold wall and then is pressurized into the preform by moving the top mold to close the gap as shown in Figure 7.1. The process consists of preform layup, partial mold closure, resin injection into the gap, closing the gap (impregnation of resin into the fibrous material), and curing and finally demolding. Although CRTM does not use DM as in SCRIMP which was studied in the dissertation, the major direction of resin flow in CRTM is in through the thickness direction where there are local variations in permeability induced by the pinholes. This means the flow process is likely to be affected by the random variation prevalent in that direction. The effect of pinholes can

be studied numerically and experimentally with combination of process parameters such as the initial mold gap, compression pressure and gap closure speed etc [126,127].

1.Preform preparation

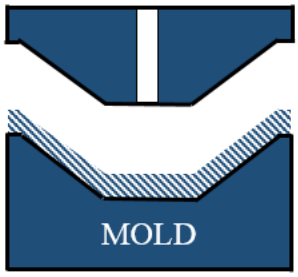

2. Preform lay-up

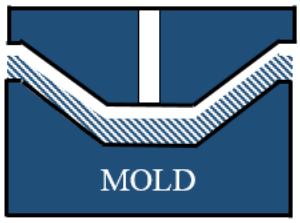

3. Partial mold closure

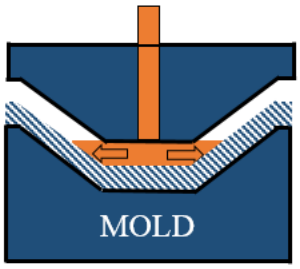

4. Resin injection into gap

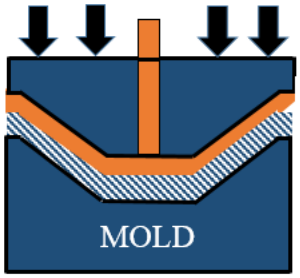

5. Gap closing : Resin impregnation

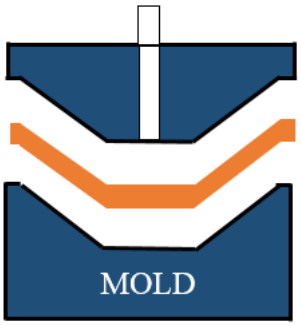

Figure 7.1 Schematic of CRTM process

Second future work can be about developing the optimized design of DM alignments so that the flow of resin in the presence of pinholes can be adequately guided and redirected to minimize the void formation using special alignment of DM in a SCRIMP (VARTM) process. The idea is to create a no DM zone between pieces of DM along the length of fabric in a SCRIMP process as illustrated in Figure 7.2. Dark blue represents 4 layers of fibrous preform and light blue indicates DM. Injection gate is placed at the top left. When resin is introduced through the injection gate, voids are most likely to be formed by irregular arrivals of resin from the top (DM) to the bottom layer of fabric, which forms more than two flow fronts merging resulting in entrapping the air and creating a void. This phenomena is exacerbated as the lead length between top and bottom flow front increases. The No DM zone should allow bottom flow to catch up with the top flow which results in a reduced lead length and reduced amount of voids due to such re-calibration as can be seen in Figure 7.3.

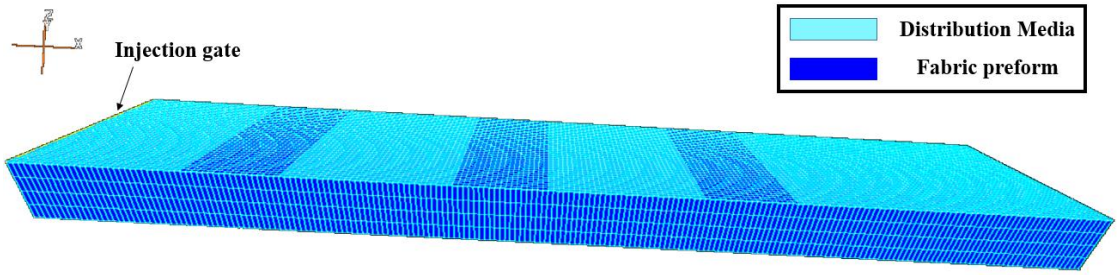

Figure 7.2 Schematic of a SCRIMP setting with the proposed DM alignment to minimize the void formation. Dark blue represents fibrous preform and light blue indicates DM.

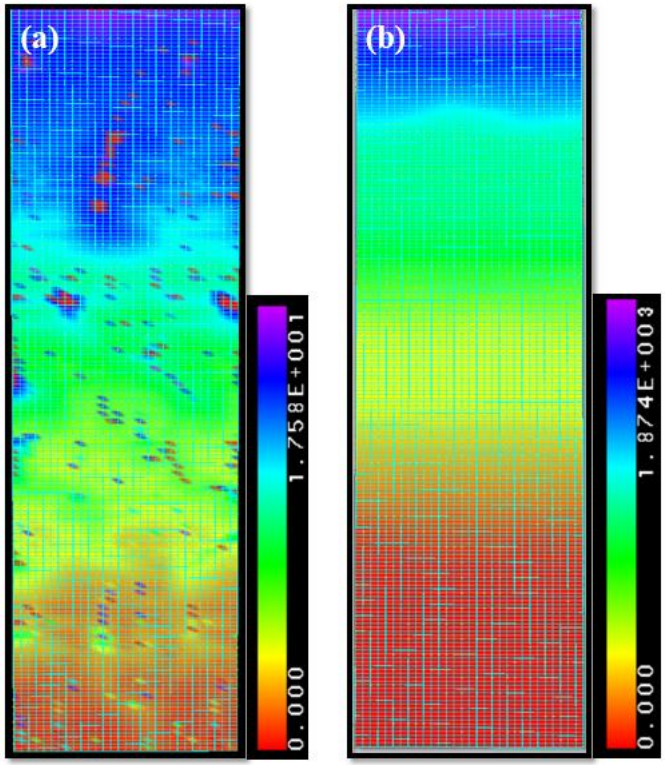

Figure 7.3 Development of flow front in the bottom layer of 4 layers in SCRIMP process with (a) DM design shown in Figure 6.1 and with (b) DM design in Figure 7.2. Color indicates the resin arrival time. The colorbar is given with filling time in seconds on the side. Resin flows from the bottom to the top.

The development of the flow front in the bottom layer when new DM design is used shows an uniform and gradual flow without any welded flow fronts where voids are likely to form. The filling time increases with less area of DM used, in this case about 2

order or magnitude bigger. An optimized DM design which prevent voids and ensures low filling time should be found as in the study by Sas et al[78].

Next suggested future work is to enhance the predictability of the void formation information by comparing the decision tree to other methods such as regression analysis or neural networks [101]. Each prediction methods can be assessed and the most appropriate one can be selected for the final usage recommendation.

Next suggested future work is to study how the parameters used in study shown in Chapter 6 are related. For example, among the parameters presented in Chapter 6, some are deeply inter-related between pinhole property (α , MI) and K_{zz}. Intuitively, it is obvious that the increase in α should result in increase in overall K_{zz}. However, it's not clear to what extent or to what degree K_{zz} is affected. The influence of MI on K_{zz} value is more complex. MI affects the K_{zz} locally than globally by increasing or decreasing local K_{zz} permeability. It's also not clear to what extent the MI influences K_{zz}. Better understanding of the parameters will allow more accurate modeling and proper non-dimensionalization which is an important step to compare the effect of each parameters. This study can be numerically and analytically carried out. And then the results from each method can be compared to verify the model.

Last suggested work is to investigate the effect of number of layers on the void formation in the SCRIMP or CRTM type of process. It can be hypothesized that as more layers of fabrics are used, the pinhole random field will become more homogenized and would result in lower void formation.The K_{eff} values with varying number of layers are calculated using Equation 3.4 and plotted in Figure 7.4. Thickness (h) is kept constant at the value of 0.28mm. The K_{eff} values which indicate the magnitude of influence of K_{pin} decreases to reach plateau between 6-7layers.

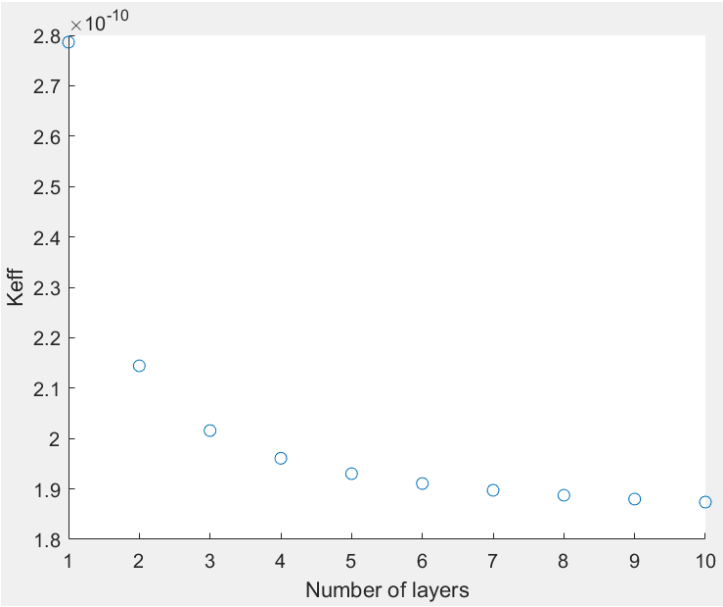

Figure 7.4 K_{eff} values calculated with varying number of layers

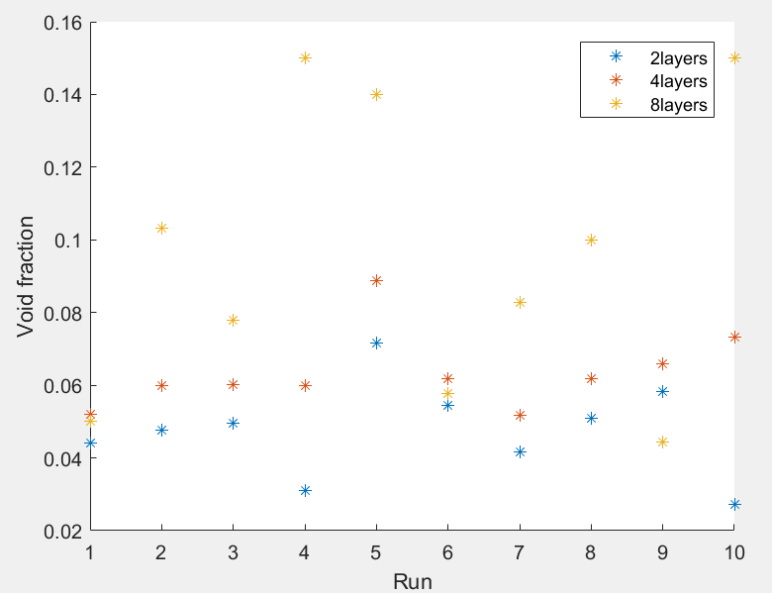

Figure 7.5 Void fraction calculated from 10 simulation runs for each case (2,4,and 8 layers)

Numerical simulations were also carried out with varying number of layers (2,4, and 8 layers) to quantify its effect on the void formation. The values of parameters for the numerical simulation are listed in chapter 4.2.7. The same K_{pin} random field is assigned to all layers of fabrics. Ten simulations were excecuted for each case (2,4, and 8 layers). The average value of void fraction for each case were found to be 4.74% for 2 layers, 6.3% for 4 layers, and 9.55% for 8 layer. First thing to notice is that the degree of void formation is affected by the number of layers of fabrics. Although analytical solution calculated using averaged and homogenized permeability value (K_{xx}) shows decrease in the Kpin,eff value, the numerical simulation results show the opposite trend of increasing the effect of pinhole random fields (increasing void fraction). The trend can be seen in Figure 7.5.This could be explained that the numerical simulation captures the effect of locally varying Kpin random field which seems to still play an important role although one would expect this effect will diminish with increasing number of layers. As the number of layers increase, the void fraction increases upto 8 layers because more random fields are added.This trend could change as more layers of fabrics are added resulting in more homogenized pinhole random field. A total of thirty additional numerical simulations were carried out with different K_{pin} random fields assigned to each layer ofThese simulations were equally distributed between three cases in which the total thickness was the same but for the first case, the composite consisted of two layers, for the second case the composite was made up of four layers and for the third case the number of layers was increased to eight. The average void fraction from ten simulation for each case was calculated to be 0.009 for 2 layers, 0.0237 for 4 layers, and 0.0244 for 8 layers. The effect of the random field on void formation is less with different random fields assigned to each layer than with the same random fields

assigned to all the layers. This needs to be explored further. Also the influence of number of layers needs to be studied experimentally to evaluate the validity of the hypothesis.

In summary, this work has initiated an approach in which preform variability can be characterized and its effect on void formation quantified. How such variability interacts with other material and process parameters have also been explored and the ground work for using flow simulations with stochastic material and process parameters to guide the material and process design to improve the yield from the manufacturing process has been laid.

REFERENCES

[1] S.G. Advani, E.M. Sozer, Process Modeling in Composites Manufactoring, 2002.

[2] BMW i3 - First Mass Produced Car Made With Composites | CompositesLab, (n.d.). http://compositeslab.com/bmw-i3-first-mass-produced-car-made-largely-with-composites/ (accessed July 18, 2018).

[3] A.T.W. Min, Y.S. Ong, A. Gupta, C.K. Goh, Multi-Problem Surrogates: Transfer Evolutionary Multiobjective Optimization of Computationally Expensive Problems, IEEE Trans. Evol. Comput. (2017). doi:10.1109/TEVC.2017.2783441.

[4] W.H. Seemann, G.C. Tunis, A.P. Perrella, K. Rikard, E.H. Del, A. Everett, P.W.R. I, W. Schurgin, H. Llp, United States Patent 5,721,034, 1998.

[5] J. Wang, P. Simacek, N. Gupta, S.G. Advani, Multidisciplinary tool for composite wind blade design & analysis, Compos. Part B Eng. 140 (2018) 91–98. doi:10.1016/j.compositesb.2017.09.075.

[6] D. a Griffin, Blade System Design Studies Volume I : Composite Technologies for Large Wind Turbine Blades, Energy. I (2002) 1–54. http://sandia.gov/wind/other/021879.pdf.

[7] J. Chen, Q. Wang, W.Z. Shen, X. Pang, S. Li, X. Guo, Structural optimization study of composite wind turbine blade, Mater. Des. 46 (2013) 247–255. doi:10.1016/j.matdes.2012.10.036.

[8] F. Takeda, S. Nishiyama, K. Hayashi, Y. Komori, Y. Suga, N. Asahara, Research in the Application of the Vartm Technique To the Fabrication of Primary Aircraft Composite Structure.Pdf, Mitsubishi Heavy Ind. Ltd. Tech. Rev. 42 (2005) 1–6.

[9] Rhinolinings Latino Industrial, (n.d.). http://rhinolatinoindustrial.com/products/cipp,_composites_and_vartm/vartm/51/65 (accessed July 24, 2018).

[10] J.P. Feser, A.K. Prasad, S.G. Advani, Experimental characterization of in-plane permeability of gas diffusion layers, J. Power Sources. 162 (2006) 1226–1231. doi:10.1016/j.jpowsour.2006.07.058.

[11] X. Zeng, L.P. Brown, A. Endruweit, M. Matveev, A.C. Long, Geometrical modelling of 3D woven reinforcements for polymer composites: Prediction of fabric permeability and composite mechanical properties, Compos. Part A Appl. Sci. Manuf. 56 (2014) 150–160. doi:10.1016/j.compositesa.2013.10.004.

[12] E. Berndt, I. Sevostianov, Multiscale modeling of fluid permeability of a non-homogeneous porous media, Int. J. Eng. Sci. 56 (2012) 99–110. doi:10.1016/j.ijengsci.2012.03.036.

[13] A.. Fallis, On the uncertainty of tow-level permeability in fibrous porous media, J. Chem. Inf. Model. 53 (2013) 1689–1699. doi:10.1017/CBO9781107415324.004.

[14] N. Vernet, E. Ruiz, S. Advani, J.B. Alms, M. Aubert, M. Barburski, B. Barari, J.M. Beraud, D.C. Berg, N. Correia, M. Danzi, T. Delavière, M. Dickert, C. Di Fratta, A. Endruweit, P. Ermanni, G. Francucci, J.A. Garcia, A. George, C. Hahn, F. Klunker, S. V. Lomov, A. Long, B. Louis, J. Maldonado, R. Meier, V. Michaud, H. Perrin, K. Pillai, E. Rodriguez, F. Trochu, S. Verheyden, M. Weitgrefe, W. Xiong, S. Zaremba, G. Ziegmann, Experimental determination of the permeability of engineering textiles: Benchmark II, Compos. Part A Appl. Sci. Manuf. 61 (2014) 172–184. doi:10.1016/j.compositesa.2014.02.010.

[15] F.T. C. Demaria, Edu Ruiz, In-Plane Anisotropic Permeability Characterization of Deformed Woven Fabrics by Unidirectional Injection. Part I: Experimental Results, Polym. Polym. Compos. 16 (2008) 101–113. doi:10.1002/pc.

[16] S. Sharma, D.A. Siginer, Permeability Measurement Methods in Porous Media of Fiber Reinforced Composites, Appl. Mech. Rev. 63 (2010) 020802. doi:10.1115/1.4001047.

[17] K. Okonkwo, P. Simacek, S.G. Advani, R.S. Parnas, Characterization of 3D fiber preform permeability tensor in radial flow using an inverse algorithm based on sensors and simulation, Compos. Part A Appl. Sci. Manuf. 42 (2011) 1283–1292. doi:10.1016/j.compositesa.2011.05.010.

[18] J.M. Lawrence, J. Barr, R. Karmakar, S.G. Advani, Characterization of preform permeability in the presence of race tracking, Compos. Part A Appl. Sci. Manuf. 35 (2004) 1393–1405. doi:10.1016/j.compositesa.2004.05.002.

[19] A. Gokce, M. Chohra, S.G. Advani, S.M. Walsh, Permeability estimation algorithm to simultaneously characterize the distribution media and the fabric preform in vacuum assisted resin transfer molding process, Compos. Sci. Technol. 65 (2005) 2129–2139. doi:10.1016/j.compscitech.2005.05.012.

[20] V.M. a Calado, S.G. Advani, Effective average permeability of multi-layer preforms in resin transfer molding, Compos. Sci. Technol. 56 (1996) 519–531. doi:10.1016/0266-3538(96)00037-1.

[21] S.G.A. Hatice Sas, Pavel Simacek, Minyoung Yun, Louis Agostino, A new approach for textile fiber preform permeability tensor characterization with non-zero skew components, Texcomp -12 Conf. (2015) 26–29.

[22] M. Yun, H. Sas, P. Simacek, S.G. Advani, Characterization of 3D fabric permeability with skew terms, Compos. Part A Appl. Sci. Manuf. 97 (2017). doi:10.1016/j.compositesa.2016.12.030.

[23] M.A. Yalcinkaya, A. Sarioglu, E.M. Sozer, A novel mold design for one-continuous permeability measurement of fiber preforms, J. Reinf. Plast. Compos. (2015). doi:10.1177/0731684415581630.

[24] Z. Cai, Estimation of the permeability of fibrous preforms for resin transfer moulding processes, Compos. Manuf. 3 (1992) 251–257. doi:10.1016/0956-7143(92)90112-8.

[25] K.K. Han, C.W. Lee, B.P. Rice, Measurements of the permeability of fiber preforms and applications, Compos. Sci. Technol. 60 (2000) 2435–2441. doi:10.1016/S0266-3538(00)00037-3.

[26] A.L. Berdichevsky, Z. Cai, Preform permeability predictions by self-consistent method and finite element simulation, Polym. Compos. 14 (1993) 132–143. doi:10.1002/pc.750140207.

[27] L. Ding, C. Shih, Z. Liang, C. Zhang, B. Wang, In situ measurement and monitoring of whole-field permeability profile of fiber preform for liquid composite molding processes, Compos. Part A Appl. Sci. Manuf. 34 (2003) 779–789. doi:10.1016/S1359-835X(03)00121-0.

[28] S. Comas-Cardona, B. Cosson, S. Bickerton, C. Binetruy, An optically-based inverse method to measure in-plane permeability fields of fibrous reinforcements, Compos. Part A Appl. Sci. Manuf. 57 (2014) 41–48. doi:10.1016/j.compositesa.2013.10.020.

[29] N.K. Naik, M. Sirisha, a. Inani, Permeability characterization of polymer matrix composites by RTM/VARTM, Prog. Aerosp. Sci. 65 (2014) 22–40. doi:10.1016/j.paerosci.2013.09.002.

[30] M. Yun, H. Sas, P. Simacek, S.G. Advani, Characterization of 3D fabric permeability with skew terms, Compos. Part A Appl. Sci. Manuf. (2017).

doi:10.1016/j.compositesa.2016.12.030.

[31] T.S. Lundström, R. Stenberg, R. Bergström, H. Partanen, P. a. Birkeland, In-plane permeability measurements: a nordic round-robin study, Compos. Part A Appl. Sci. Manuf. 31 (2000) 29–43. doi:10.1016/S1359-835X(99)00058-5.

[32] P. Nedanov, S.G. Advani, A Method to Determine 3D Permeability of Fibrous Reinforcements, J Compos. Mater. 36 (2002) 241–254. doi:10.1106/002199802021462.

[33] D.L. Woerdeman, F.R. Phelan, R.S. Parnas, Interpretation of 3-D Permeability Measurements for RTM Modeling, Polym. Compos. 16 (1995) 7–12.

[34] H.S. Sas, E.B. Wurtzel, P. Simacek, S.G. Advani, Effect of relative ply orientation on the through-thickness permeability of unidirectional fabrics, Compos. Sci. Technol. 96 (2014) 116–121. doi:10.1016/j.compscitech.2014.03.007.

[35] Bruschke, A predictive model for permeability and non-isothermal flow of viscous and shear-thinning fluids in anisotropic fibrous media, Arbor Cienc. Pensam. Y Cult. (1992). doi:10.16953/deusbed.74839.

[36] L. Bergamasco, S. Izquierdo, I. Pagonabarraga, N. Fueyo, Multi-scale permeability of deformable fibrous porous media, Chem. Eng. Sci. 126 (2015) 471–482. doi:10.1016/j.ces.2014.11.065.

[37] K. Potter, B. Khan, M. Wisnom, T. Bell, J. Stevens, Variability, fibre waviness and misalignment in the determination of the properties of composite materials and structures, Compos. Part A Appl. Sci. Manuf. 39 (2008) 1343–1354. doi:10.1016/j.compositesa.2008.04.016.

[38] A. Vanaerschot, B.N. Cox, S. V. Lomov, D. Vandepitte, Stochastic framework for quantifying the geometrical variability of laminated textile composites using micro-computed tomography, Compos. Part A Appl. Sci. Manuf. 44 (2013) 122–131. doi:10.1016/j.compositesa.2012.08.020.

[39] L. Fang, J. Jiang, J. Wang, C. Deng, Effect of Nesting on the Out-of-Plane Permeability of Unidirectional Fabrics in Resin Transfer Molding, Appl. Compos. Mater. 22 (2015) 231–249. doi:10.1007/s10443-014-9403-6.

[40] B. Chen, T.W. Chou, Compaction of woven-fabric preforms: Nesting and multi-layer deformation, Compos. Sci. Technol. 60 (2000) 2223–2231. doi:10.1016/S0266-3538(00)00017-8.

[41] K. Hoes, D. Dinescu, H. Sol, R.S. Parnas, S. Lomov, Study of nesting induced scatter of permeability values in layered reinforcement fabrics, Compos. Part A Appl. Sci. Manuf. 35 (2004) 1407–1418. doi:10.1016/j.compositesa.2004.05.004.

[42] S. Aranda, D.C. Berg, M. Dickert, M. Drechsel, G. Ziegmann, Influence of shear on the permeability tensor and compaction behaviour of a non-crimp fabric, Compos. Part B Eng. 65 (2014) 158–163. doi:10.1016/j.compositesb.2014.02.005.

[43] B. Markicevic, D. Heider, S.G. Advani, S. Walsh, Stochastic modeling of preform heterogeneity to address dry spots formation in the VARTM Process, Compos. Part A Appl. Sci. Manuf. 36 (2005) 851–858. doi:10.1016/j.compositesa.2004.09.002.

[44] A. Vanaerschot, B.N. Cox, S. V. Lomov, D. Vandepitte, Stochastic multi-scale modelling of textile composites based on internal geometry variability, Comput. Struct. 122 (2013) 55–64. doi:10.1016/j.compstruc.2012.10.026.

[45] M. Bodaghi, A. Vanaerschot, S. V Lomov, N.C. Correia, On the stochastic variations of intra-tow permeability induced by internal geometry variability in a 2 / 2 twill carbon fabric, Compos. Part A. 101 (2017) 444–458. doi:10.1016/j.compositesa.2017.07.008.

[46] P. Smith, C.D. Rudd, a. C. Long, The effect of shear deformation on the processing and mechanical properties of aligned reinforcements, Compos. Sci. Technol. 57 (1997) 327–344. doi:10.1016/S0266-3538(96)00132-7.

[47] A. Endruweit, P. McGregor, A.C. Long, M.S. Johnson, Influence of the fabric architecture on the variations in experimentally determined in-plane permeability values, Compos. Sci. Technol. 66 (2006) 1778–1792. doi:10.1016/j.compscitech.2005.10.031.

[48] A. Endruweit, P. Ermanni, The in-plane permeability of sheared textiles. Experimental observations and a predictive conversion model, Compos. Part A Appl. Sci. Manuf. 35 (2004) 439–451. doi:10.1016/j.compositesa.2003.11.002.

[49] F. Zhang, S. Comas-cardona, C. Binetruy, Statistical modeling of in-plane permeability of non-woven random fibrous reinforcement, Compos. Sci. Technol. 72 (2012) 1368–1379. doi:10.1016/j.compscitech.2012.05.008.

[50] F. Zhang, B. Cosson, S. Comas-Cardona, C. Binetruy, Efficient stochastic simulation approach for RTM process with random fibrous permeability, Compos. Sci. Technol. 71 (2011) 1478–1485. doi:10.1016/j.compscitech.2011.06.006.

[51] M. Bodaghi, S.Y. Sekeh, N. Correia, Probability density function of in-plane permeability of brous media : Constant Kozeny coe cient, (n.d.) 1–23.

[52] M. Bodaghi, G. Catalanotti, N. Correia, On the statistics of transverse permeability of randomly distributed fibers, Compos. Struct. 158 (2016) 323–332. doi:10.1016/j.compstruct.2016.09.045.

[53] J. Li, C. Zhang, R. Liang, B. Wang, Statistical characterization and robust design of RTM processes, Compos. Part A Appl. Sci. Manuf. 36 (2005) 564–580. doi:10.1016/j.compositesa.2004.10.001.

[54] J.M. Lawrence, P. Fried, S.G. Advani, Automated manufacturing environment to address bulk permeability variations and race tracking in resin transfer molding by redirecting flow with auxiliary gates, Compos. Part A Appl. Sci. Manuf. 36 (2005) 1128–1141. doi:10.1016/j.compositesa.2005.01.024.

[55] S. Bickerton, S.G. Advani, Characterization and modeling of race-tracking in liquidcomposite molding processes, Compos. Sci. Technol. 59 (1999) 2215–2229. doi:10.1016/S0266-3538(99)00077-9.

[56] F. Klunker, M. Danzi, P. Ermanni, Fiber deformation as a result of fluid injection: modeling and validation in the case of saturated permeability measurements in through thickness direction, J. Compos. Mater. 49 (2015) 1091–1105. doi:10.1177/0021998314530766.

[57] S. V. Lomov, I. Verpoest, T. Peeters, D. Roose, M. Zako, Nesting in textile laminates: Geometrical modelling of the laminate, Compos. Sci. Technol. 63 (2003) 993–1007. doi:10.1016/S0266-3538(02)00318-4.

[58] R. Helmus, R. Hinterhölzl, P. Hubert, A stochastic approach to model material variation determining tow impregnation in out-of-autoclave prepreg consolidation, Compos. Part A Appl. Sci. Manuf. 77 (2015) 293–300. doi:10.1016/j.compositesa.2015.03.021.

[59] B. Verleye, R. Croce, M. Griebel, M. Klitz, S. V. Lomov, G. Morren, H. Sol, I. Verpoest, D. Roose, Permeability of textile reinforcements: Simulation, influence of shear and validation, Compos. Sci. Technol. 68 (2008) 2804–2810. doi:10.1016/j.compscitech.2008.06.010.

[60] B. Ntinger, The effective permeability of a heterogeneous porous medium, Transp. Porous Media. 15 (1994) 99–127. doi:10.1007/BF00625512.

[61] S. Bickerton, E.M. Sozer, P. Šimácek, S.G. Advani, Fabric structure and mold curvature effects on preform permeability and mold filling in the RTM process.

Part II. Predictions and comparisons with experiments, Compos. Part A Appl. Sci. Manuf. 31 (2000) 439–458. doi:10.1016/S1359-835X(99)00088-3.

[62] M. Bodaghi, P. Simacek, S.G. Advani, N.C. Correia, A model for fibre washout during high injection pressure resin transfer moulding, J. Reinf. Plast. Compos. (2018). doi:10.1177/0731684418765968.

[63] A. Endruweit, A.C. Long, F. Robitaille, C.D. Rudd, Influence of stochastic fibre angle variations on the permeability of bi-directional textile fabrics, Compos. Part A Appl. Sci. Manuf. 37 (2006) 122–132. doi:10.1016/j.compositesa.2005.04.014.

[64] A. Endruweit, A.C. Long, Influence of stochastic variations in the fibre spacing on the permeability of bi-directional textile fabrics, Compos. Part A Appl. Sci. Manuf. 37 (2006) 679–694. doi:10.1016/j.compositesa.2005.08.003.

[65] A.A. Skordos, M.P.F. Sutcliffe, Stochastic simulation of woven composites forming, Compos. Sci. Technol. 68 (2008) 283–296. doi:10.1016/j.compscitech.2007.01.035.

[66] M.T. Senoguz, F.D. Dungan, A.M. Sastry, J.T. Klamo, Simulations and Experiments on Low-Pressure Permeation of Fabrics: Part II—The Variable Gap Model and Prediction of Permeability, J. Compos. Mater. 35 (2001) 1285–1322. doi:10.1106/HWL5-599F-8NA8-XAN0.

[67] K. Tackitt, S. Walsh, Experimental Study of Thickness Gradient Formation in the VARTM Process, Mater. Manuf. Process. 20 (2005) 607–627. doi:10.1081/AMP-200041896.

[68] X. Zeng, A. Endruweit, L.P. Brown, A.C. Long, Numerical prediction of in-plane permeability for multilayer woven fabrics with manufacture-induced deformation, Compos. Part A Appl. Sci. Manuf. 77 (2015) 266–274. doi:10.1016/j.compositesa.2015.03.027.

[69] R. Arbter, J.M. Beraud, C. Binetruy, L. Bizet, J. Breard, S. Comas-Cardona, C. Demaria, A. Endruweit, P. Ermanni, F. Gommer, S. Hasanovic, P. Henrat, F. Klunker, B. Laine, S. Lavanchy, S. V. Lomov, A. Long, V. Michaud, G. Morren, E. Ruiz, H. Sol, F. Trochu, B. Verleye, M. Wietgrefe, W. Wu, G. Ziegmann, Experimental determination of the permeability of textiles: A benchmark exercise, Compos. Part A Appl. Sci. Manuf. 42 (2011) 1157–1168. doi:10.1016/j.compositesa.2011.04.021.

[70] J.R. Weitzenbock, R.A. Shenoi, P.A. Wilson, Radial flow permeability measurement. Part A: theory, Compos. Part A Appl. Sci. Manuf. 30 (1999) 781–

796. doi:10.1016/S1359-835X(98)00183-3.

[71] R. Chelouah, P. Siarry, A hybrid method combining continuous tabu search and Nelder–Mead simplex algorithms for the global optimization of multiminima functions, Eur. J. Oper. Res. 161 (2005) 636–654. doi:10.1016/j.ejor.2003.08.053.

[72] R. Chelouah, P. Siarry, Genetic and Nelder-Mead algorithms hybridized for a more accurate global optimization of continuous multiminima functions, Eur. J. Oper. Res. 148 (2003) 335–348. doi:10.1016/S0377-2217(02)00401-0.

[73] S.K.S. Fan, Y.C. Liang, E. Zahara, A genetic algorithm and a particle swarm optimizer hybridized with Nelder-Mead simplex search, Comput. Ind. Eng. 50 (2006) 401–425. doi:10.1016/j.cie.2005.01.022.

[74] S.K.S. Fan, E. Zahara, A hybrid simplex search and particle swarm optimization for unconstrained optimization, Eur. J. Oper. Res. 181 (2007) 527–548. doi:10.1016/j.ejor.2006.06.034.

[75] A. Hertz, D. Werra, Using tabu search techniques for graph coloring, Computing. 39 (1987) 345–351. doi:10.1007/BF02239976.

[76] J. a. Nelder, R. Mead, A simplex method for function minimization, Comput. J. 7 (1964) 308–313. doi:10.1093/comjnl/7.4.308.

[77] P. Šimáček, S.G. Advani, Desirable features in mold filling simulations for liquid composite molding processes, Polym. Compos. 25 (2004) 355–367. doi:10.1002/pc.20029.

[78] H.S. Sas, P. Šimáček, S.G. Advani, A methodology to reduce variability during vacuum infusion with optimized design of distribution media, Compos. Part A Appl. Sci. Manuf. 78 (2015) 223–233. doi:10.1016/j.compositesa.2015.08.011.

[79] J. Wang, P. Simacek, S.G. Advani, Use of Centroidal Voronoi Diagram to find optimal gate locations to minimize mold filling time in resin transfer molding, Compos. Part A Appl. Sci. Manuf. 87 (2016) 243–255. doi:10.1016/j.compositesa.2016.04.026.

[80] M. Nordlund, T.S. Lundström, V. Frishfelds, A. Jakovics, Permeability network model for non-crimp fabrics, Compos. Part A Appl. Sci. Manuf. 37 (2006) 826–835. doi:10.1016/j.compositesa.2005.02.009.

[81] H. Huang, R. Talreja, Effects of void geometry on elastic properties of unidirectional fiber reinforced composites, Compos. Sci. Technol. 65 (2005)

1964–1981. doi:10.1016/j.compscitech.2005.02.019.

[82] T. Tran, S. Comas-Cardona, N.E. Abriak, C. Binetruy, Unified microporomechanical approach for mechanical behavior and permeability of misaligned unidirectional fiber reinforcement, Compos. Sci. Technol. 70 (2010) 1410–1418. doi:10.1016/j.compscitech.2010.04.023.

[83] L. Liu, B.M. Zhang, D.F. Wang, Z.J. Wu, Effects of cure cycles on void content and mechanical properties of composite laminates, Compos. Struct. 73 (2006) 303–309. doi:10.1016/j.compstruct.2005.02.001.

[84] P. Olivier, J.P. Cottu, B. Ferret, Effects of cure cycle pressure and voids on some mechanical properties of carbon/epoxy laminates, Composites. 26 (1995) 509–515. doi:10.1016/0010-4361(95)96808-J.

[85] F. White, Fluid Mechanics, (2009) 887.

[86] M. V. Bruschke, S.G. Advani, Flow of generalized Newtonian fluids across a periodic array of cylinders, J. Rheol. 37 (1993) 479–498. doi:10.1122/1.550455.

[87] E. Ruiz, V. Achim, S. Soukane, F. Trochu, J. Bréard, Optimization of injection flow rate to minimize micro/macro-voids formation in resin transfer molded composites, Compos. Sci. Technol. 66 (2006) 475–486. doi:10.1016/j.compscitech.2005.06.013.

[88] M. Yun, T. Carella, P. Simacek, S. Advani, Stochastic modeling of through the thickness permeability variation in a fabric and its effect on void formation during Vacuum Assisted Resin Transfer Molding, Compos. Sci. Technol. 149 (2017) 100–107. doi:10.1016/j.compscitech.2017.06.016.

[89] M. Bodaghi, A. Vanaerschot, S. V Lomov, N.C. Correia, On the variability of mesoscale permeability of a 2 / 2 twill carbon fabric induced by variability of the internal geometry l, Compos. Part A. 101 (2017) 394–407. doi:10.1016/j.compositesa.2017.05.030.

[90] R.V. Roy, S.T. Grilli, Probabilistic analysis of flow in random porous media by stochastic boundary elements, Eng. Anal. Bound. Elem. 19 (1997) 239–255. doi:10.1016/S0955-7997(97)00009-X.

[91] R.A. Kennedy, P. Sadeghi, T.D. Abhayapala, H.M. Jones, Intrinsic limits of dimensionality and richness in random multipath fields, IEEE Trans. Signal Process. 55 (2007) 2542–2556. doi:10.1109/TSP.2007.893738.

[92] J. Zhang, B. Ellingwood, Orthogonal Series Expansions of Random Fields in

Reliability Analysis, J. Eng. Mech. 120 (1994) 2660–2677. doi:10.1061/(ASCE)0733-9399(1994)120:12(2660).

[93] D. Zhang, Z. Lu, An efficient, high-order perturbation approach for flow in random porous media via Karhunen-Loève and polynomial expansions, J. Comput. Phys. 194 (2004) 773–794. doi:10.1016/j.jcp.2003.09.015.

[94] C. Zhang, L. Luo, W. Xu, V. Ledwith, Use of local Moran's I and GIS to identify pollution hotspots of Pb in urban soils of Galway , Ireland, 8 (2008). doi:10.1016/j.scitotenv.2008.03.011.

[95] J. Liou, Y. Su, J. Chiang, K. Cheng, A covariance conversion approach of Gamma random field simulation, (2008).

[96] M.R. Driels, Y.S. Shin, Determining the number of iterations for Monte Carlo simulations of weapon effectiveness, Reports Tech. Reports. (2004). http://hdl.handle.net/10945/798.

[97] M. Yun, P. Simacek, C. Binetruy, S. Advani, Random field generation of stochastically varying through the thickness permeability of a plain woven fabric, Compos. Sci. Technol. (2018). doi:10.1016/j.compscitech.2018.02.035.

[98] A.R. Jamieson, M.L. Giger, K. Drukker, H. Li, Y. Yuan, N. Bhooshan, Exploring nonlinear feature space dimension reduction and data representation in breast CADx with Laplacian eigenmaps and t -SNE, Med. Phys. 37 (2010) 339–351. doi:10.1118/1.3267037.

[99] M. a. M.A. Friedl, C.E.C.E. Brodley, Decision tree classification of land cover from remotely sensed data, Remote Sens. Environ. 61 (1997) 399–409. doi:10.1016/S0034-4257(97)00049-7.

[100] S. Geman, E. Bienenstock, R. Doursat, Neural networks and the bias/variance dilemma, Neural Comput. 4 (1992) 1–58. doi:10.1162/neco.1992.4.1.1.

[101] G.K.F. Tso, K.K.W. Yau, Predicting electricity energy consumption: A comparison of regression analysis, decision tree and neural networks, Energy. 32 (2007) 1761–1768. doi:10.1016/j.energy.2006.11.010.

[102] L.K.L. Saul, S.S.T. Roweis, Think globally, fit locally: unsupervised learning of low dimensional manifolds, J. Mach. Learn. Res. 4 (2003) 119–155. doi:10.1162/153244304322972667.

[103] A.N. Kandpal, B.B.M. Rao, Implementation of PCA & ICA for voice ecognition and separation of speech, ICAMS 2010 - Proc. 2010 IEEE Int. Conf. Adv.

Manag. Sci. 3 (2010) 536–538. doi:10.1109/ICAMS.2010.5553181.

[104] J.C. Isaacs, S.Y. Foo, A. Meyer-Baese, Novel kernels and kernel PCA for pattern recognition, Proc. 2007 IEEE Int. Symp. Comput. Intell. Robot. Autom. CIRA 2007. (2007) 438–443. doi:10.1109/CIRA.2007.382927.

[105] J.L. Xiaojin Zhu, Zoubin Ghaharamani, Semi-Supervised Learning Using Gaussian Fields and Harmonic Functions, in: Proc. Twent. Int. Conf. Mach. Learn., 2003.

[106] G. Tesauro, Temporal Difference Learning and TD-Gammon, Commun. ACM. 38 (1995) 58–67.

[107] C.J.C.H. Watkins, P. Dayan, Q-learning, Mach. Learn. 8 (1992) 279–292. doi:10.1007/BF00992698.

[108] Q. Wang, Kernel Principal Component Analysis and its Applications in Face Recognition and Active Shape Models, ArXiv Prepr. ArXiv1207.3538. (2012). http://arxiv.org/abs/1207.3538.

[109] A. Gisbrecht, A. Schulz, B. Hammer, Parametric nonlinear dimensionality reduction using kernel t-SNE, Neurocomputing. 147 (2015) 71–82. doi:10.1016/j.neucom.2013.11.045.

[110] E. Lopez, D. Gonzalez, J. V Aguado, E. Cueto, C. Binetruy, F. Chinesta, A Manifold Learning Approach for Integrated Computational Materials Engineering, 25 (2018) 59–68. doi:10.1007/s11831-016-9172-5.

[111] L.J.P. Van Der Maaten, G.E. Hinton, Visualizing high-dimensional data using t-sne, J. Mach. Learn. Res. 9 (2008) 2579–2605. doi:10.1007/s10479-011-0841-3.

[112] S.T. Roweis, Nonlinear Dimensionality Reduction by Locally Linear Embedding, 2323 (2009). doi:10.1126/science.290.5500.2323.

[113] S. Wold, K.I.M. Esbensen, P. Geladi, Principal Component Analysis, SpringerReference. 2 (1987) 37–52. doi:10.1007/SpringerReference_205537.

[114] G. Guo, Y. Fu, C.R. Dyer, T.S. Huang, Image-based human age estimation by manifold learning and locally adjusted robust regression, IEEE Trans. Image Process. 17 (2008) 1178–1188. doi:10.1109/TIP.2008.924280.

[115] E. Lopez, E. Abisset-Chavanne, F. Lebel, R. Upadhyay, S. Comas, C. Binetruy, F. Chinesta, Advanced thermal simulation of processes involving materials exhibiting fine-scale microstructures, Int. J. Mater. Form. 9 (2016) 179–202.

doi:10.1007/s12289-015-1222-2.

[116] H.J.. Kim, K.I.a , Jung, K.b, Kim, Face Recognition Using Kernel Principal Component Analysis, IEEE Signal Process. Lett. 9 (2002) 40–42. doi:10.1016/0169-7439(87)80084-9.

[117] X. Teng, B. Wu, W. Yu, C. Liu, A hand gesture recognition system based on local linear embedding, J. Vis. Lang. Comput. 16 (2005) 442–454. doi:10.1016/j.jvlc.2005.04.003.

[118] F.C. Elena Lopez, Adrien Scheuer, Emmanuelle Abisset-Chavanne, On the effect of phase transition on the manifold dimensionality: Application to the Ising model, Math. Mech. Complex Syst. Submitt. (n.d.).

[119] C.M. Bishop, Pattern Recognition and Machine Learning, 2013. doi:10.1117/1.2819119.

[120] G. Hinton, S. Roweis, Stochastic Neighbor Embedding, (2002). https://papers.nips.cc/paper/2276-stochastic-neighbor-embedding.pdf.

[121] V. Scienzia, S.E. Non, P. Per, L.D.A. Vinci, Mathematics and Mechanics of Complex Systems, 2018.

[122] M. Yun, P. Simacek, C. Binetruy, S. Advani, Random field generation of stochastically varying through the thickness permeability of a plain woven fabric, Compos. Sci. Technol. 159 (2018) 199–207. doi:10.1016/j.compscitech.2018.02.035.

[123] Y. Hou, P. Edara, C. Sun, Situation assessment and decision making for lane change assistance using ensemble learning methods, Expert Syst. Appl. 42 (2015) 3875–3882. doi:10.1016/j.eswa.2015.01.029.

[124] A. Criminisi, J. Shotton, E. Konukoglu, Decision Forests for Classification , Regression , Density Estimation , Manifold Learning and Semi-Supervised Learning, Learning. 7 (2011) 81–227. doi:10.1561/0600000035.

[125] T. Decision, T. Tutorial, DECISION TREES : How to Construct Them and How to Use Them for Classifying New Data Avinash Kak, (2017) 1–127.

[126] O. Geiger, D. Schmidt, Compression RTM - A new process for manufacturing high volume continuous fiber reinforced composites, 5th Int. CFK-Valley Stade Conv. (2011).

[127] P. Bhat, J. Merotte, P. Simacek, S.G. Advani, Process analysis of compression

resin transfer molding, Compos. Part A Appl. Sci. Manuf. 40 (2009) 431–441. doi:10.1016/j.compositesa.2009.01.006.

[128] M. V. Bruschke, S.G. Advani, A finite element/control volume approach to mold filling in anisotropic porous media, Polym. Compos. 11 (1990) 398–405. doi:10.1002/pc.750110613.

[129] Z. Chen, Networks and Heterogeneous Media on the Control Volume Finite Element Methods and Their Applications To Multiphase Flow, Am. Inst. Math. Sci. 1 (2006) 689–706. doi:10.3934/nhm.2006.1.689.

Appendix A

INTRODUCTION OF LIQUID INJECTION MOLDING SIMULATION (LIMS)

Liquid Injection Molding Simulation (LIMS) developed by University of Delaware is a 3D flow simulation software using control volume and finite element method[128,129]. LIMS simulates the mold filling process of RTM, the movement of Newtonian fluid (resin) through porous medium (reinforcing fabrics), using Darcy's law (Equation 1.1). Darcy's law and mass conservation method are used to solve for pressure field as can be seen in Equation A.1.

$$-\nabla \cdot (K \cdot \nabla P) = 0 \tag{A.1}$$

The boundary condition used to solve the equation is that pressure is always 0 at the flow front and that fluid cannot flow through the mold wall. Inlet and vent can be set with either pressure or flow rate condition. Once pressure fieild is known, the velocity filed can be found. Material property such as permeability or viscosity should be provided. The calculation is done on quasi-steady state term.

3D(fabric), 2D(DM) and 1D (pinhole) mesh can be used to simulate the fluid flow in the simulation. Any various shape of meshs are acceptable for numerical simulation.

For more information, these journals[77,128] or website (https://sites.udel.edu/lims/) are recommended to read.

Appendix B

REPRINT PERMISSION LETTERS